UNIVERSITY OF CALIFORNIA

Santa Barbara

The biomimetic, rational and quantitative design of cooperative receptors and responsive materials

A Dissertation submitted in partial satisfaction of the

requirements for the degree Doctor of Philosophy

in Biochemistry and Molecular Biology

by

Anna Julia Simon

Committee in charge:

Professor Kevin W. Plaxco, Chair

Professor Omar A. Saleh

Professor Kathleen R. Foltz

Professor Fredrick W. Dahlquist

September 2015

This dissertation of Anna Julia Simon is approved.

_____

Kevin Plaxco, Ph.D.

_____

Kathleen Foltz, Ph.D.

_____

Rick Dahlquist, Ph.D.

_____

Omar Saleh, Ph.D.

September 2015

ACKNOWLEDGEMENTS

My graduate work has centered on cooperativity, in which multiple components come together to form a cohesive whole and perform tasks that are impossible for one piece to do on its own. In a similar way, throughout my time in graduate school, there have been many, many mentors, colleagues, and friends who have helped and inspired me to do things that would have been impossible for me alone.

First and foremost, I am immensely thankful to my adviser, Professor Kevin Plaxco, for his incredible support, guidance, and humor through the years. For his encouragement for me to keep pushing myself, keep thinking and exploring, not settle for awkward writing or unsatisfying data.

To my committee members, Professors Kathy Foltz, Rick Dahlquist, and Omar Saleh, for their thoughtful questions and guidance.

To my first mentors in the Plaxco lab, Professors Andrew Bonham and Alexis Vallée-Bélisle, for their patience, wisdom, and boundless, infectious enthusiasm.

To Professor Chunhai Fan, for welcoming me into his lab in Shanghai, China, for three months, and Dr. Xuihai Mao, for his patience, kindness, and friendship during my time there.

To Luke Walls-Smith, for his hard work, careful eye, and persistence in working with me on our hydrogel projects.

To Dr. Mary Raven, for spending long hours with me in the NRI microscopy facility, for her constant cheerfulness and support.

To Stella Hahn, Lauren Baker, Nicole McCoy, Cabe Fletcher, Brett Beisecker, Luci Rojas, Mira Lazaro, Erika James, Naoko Gresback, and Marlene Carlyle for their constant competence, patience, and hard work.

To the "First Years," Dr. Matthew Lalli and soon-to-be doctors Julia Willett and Sarah Abdul-Wajid, for their humor, honesty, and incredible friendship from the beginning to end of these past five years.

To my siblings, Rebecca and Will Simon, for their love and friendship throughout our lives.

To my parents, Helene and David Simon, for their love and support, and for setting amazing examples of the kind of person I want to become. To my mother for encouraging my interest in the natural world, from traipsing around vernal pools and trying to set up a telescope with me on cold New England winter nights to suggesting that I engineer cats with opposable thumbs. My father for his quiet, direct, integrity and for inspiring my love of numbers and statistics.

VITA OF ANNA JULIA SIMON

September 2015

Education

University of California, Santa Barbara 9/10-9/15
Ph. D., Biochemistry and Molecular Biology (Biophysics/Bioengineering Emphasis)

Massachusetts Institute of Technology 9/06-6/10
B.S., Biological Engineering

Research

University of California, Santa Barbara Santa Barbara, CA
Graduate researcher; Advisor: Kevin Plaxco 6/11-present

Shanghai Institute of Applied Physics, Chinese Academy of Science Shanghai, China
PIRE-ECCI Fellow; Advisor: Chunhai Fan 10/12-2/13

Massachusetts Institute of Technology Cambridge, MA
Undergraduate researcher; Advisor: Angela Belcher 9/08-7/10

Awards & Fellowships

Invited participant, St. Jude Graduate Symposium (44 selected/1,815 applicants) 2015
Grad. Student rep, Biopolymers in vivo subgroup of Biophysical Society (elected) 2014-15
UCSB Inst. Collaborative Biotechnologies/Grad Division Matching Funds Fellowship 2014
Travel Fellowship, 3rd USA-Mexico Workshop in Biological Chemistry 2013
ACS Women Chemists Committee/Eli Lilly Travel Award (Declined) 2013
Partnership for Int'l Research & Education in Electron Chem. & Catalysis in Interfaces 2012-13
UC Regents' Special Fellowship 9/10-8/15
REU, Cent. for Polym. Assemblies & Mol. Interfaces, IBM Almaden Research Center 2009
Summer Undergraduate Research Fellowship, Caltech 2008

Publications

Watkins HM, Simon AJ, Sosnick TR, Lipman EA, Hjelm R, Plaxco KW (2015). A random coil negative control reproduces the discrepancy between scattering and FRET-based experiments of denatured protein dimensions. *Proc Natl Acad Sci USA* **112**:6631-6636

Simon AJ, Vallée-Bélisle A, Ricci F, Watkins HM, Plaxco KW (2014). Intrinsic disorder as a generalizable strategy for the rational design of highly responsive, allosterically cooperative receptors. *Proc Natl Acad Sci USA* **111**: 15048–15053.

Simon AJ, Vallée-Bélisle A, Ricci F, Watkins HM, Plaxco KW (2014). Using the population-shift mechanism to rationally introduce "Hill-type" cooperativity into a normally non-cooperative receptor.

Angewandte Chemie **53**:9471-9475

Watkins HM, Simon AJ, Ricci F, Plaxco KW (2014). Packing density effects on the folding thermodynamics of a surface-tethered biopolymer: an experimental study of folding in an ultra-crowded regime. *J Am Chem Soc* **136**:8923-7

Swasey SM, Karimova N, Aikens CM, Schultz DE, Simon AJ, Gwinn EG (2014). Chiral electronic transitions in fluorescent silver clusters stabilized by DNA. *ACS Nano* **8**:6883-6892

Mao X, Wei M, Zhu C, Lu J, Gao J, Simon AJ, Shi J, Huang Q, Fan C (2013). Real time in vitro regulation of DNA methylation using a 5-fluorouical conjugated DNA-based stimuli-responsive platform. *ACS Appl Mater Interfaces* **5**:2604–2609

Barbero R, Carnelli L, Simon A, Kao A, d'Arminio Monforte A, Ricco M, Bianchi D, Belcher AM (2013). Engineered yeast for enhanced CO_2 mineralization. *Energy and Environmental Science* **6**:660-674

Oral & Poster Presentations

St. June National Graduate Student Symposium; Memphis, TN	4/15
Biophysical Society National Meeting; Baltimore, MD	2/15
UCSB Chemical Sciences Student Seminars (invited); Santa Barbara, CA	2/15
Advanced Microscope Workshop (invited); Santa Barbara, CA	1/15
Biophysical Society National Meeting; San Francisco, CA	2/14
USA-Mexico Workshop in Biological Chemistry; Guanajuato, Mexico	11/13
UC Bioengineering Symposium; Berkeley, CA	6/12

Mentoring

UCSB Summer Applied Biotechnology Research Experience 2014
Student: Jose Marquez

UCSB Beckman Scholars 2013-14
Student: Luke Walls-Smith

Outreach & Volunteer work

Women in Science and Engineering Mentoring Committee founding member; FUSE Family Science Night; Graduate Union of Molecular Biology Investigators; UCSB Adventure Programs trip leader and kayak instructor; Santa Barbara Lindy Circle organizer

ABSTRACT

The rational, quantitative design of cooperative receptors and higher-order materials

By

Anna Julia Simon

Because the ability to effectively detect and respond to subtle chemical cues is so crucial to biological function, evolution has resulted in many diverse, intricate mechanisms for the robust, precise sensing of molecular stimuli. The ability to systematically recreate such mechanisms in artificial systems would likewise be useful in many biotechnologies, for example in biosensors, synthetic biology, and targeted drug delivery. In response, the work I present here focuses on the rational, quantitative recreation of biological mechanisms of sensing and actuation in artificial biomolecular systems.

The first aim of my thesis work, detailed in Chapters 2 and 3, centered on the rational engineering of allosteric cooperativity into normally non-cooperative artificial receptors. This mechanism, which occurs when multiple copies of identical target molecule bind to a receptor in an "all-or-nothing" fashion, increases the order of the binding curve, narrowing the transition window between bound and unbound, and enhancing the receptors' sensitivity to small changes in target concentration. To achieve this effect requires that the first copy of target molecule to bind shift the receptor from a low-affinity to a high-affinity conformation, thus increasing its affinity for the binding of subsequent copies of target molecule. Chapter 2 (published in 2014) centers on proof-of-concept efforts to engineering this mechanism into a

particularly simple and well-understood model receptor, a DNA-binding molecular beacon. I follow this in Chapter 3 (published in 2014) with the development of a disorder-based strategy suitable for the introduction of cooperativity into more complex receptors, including even those of unknown structure.

The second aim of my thesis work, detailed in Chapters 4 and 5 (in preparation for submission), focused on the engineering of multicomponent, stimulus-responsive biomolecular systems from a different perspective, specifically on the development of a quantitative understanding of the physics of stimulus-responsive materials. Materials that assemble and dissolve in response to chemical stimuli are ubiquitous in Biology – common examples are transport vesicles, viruses, and cell membranes. As with the imitation of allosteric cooperativity, the ability to rationally imitate the properties of these materials in an artificial, technological context would be useful in many applications. Although there exist many successful examples of such artificial, stimulus-responsive materials, design efforts thus far have been fairly qualitative, and systematic approaches to systematically control their properties do not exist. Part of the reason for this is that the relationship between properties such as network architecture and cooperativity, thermodynamic stability and molecular and micron scale behavior are not well understood, and there is a lack of simple, quantitative techniques for measuring the response of these materials. To address this challenge, I developed simple, straightforward techniques to measure the dissolution of a model hydrogel simultaneously at both the molecular and micron length scales, which I describe in Chapter 4. In Chapter 5, I employed these methods to explore the relationship between the thermodynamic stability and response kinetics of a model hydrogel, demonstrating the ability to quantitatively control the materials response kinetics using

simple strategies previously applied for the quantitative tuning of solution-phase biomolecular switches.

TABLE OF CONTENTS

1. INTRODUCTION

1.1 Motivation

Evolution has resulted in a myriad of strategies to recognize and respond to specific molecular stimuli in Biological systems, both simple and complex. The vertebrate immune system, for example, can generate antibodies against effectively any protein and many small molecules. The recognition of oligonucleotides via hybridization is likewise generalizable to the high-specificity, high-affinity detection of any nucleic acid sequence. These observations have motivated decades of research aimed at harnessing the power of biological recognition in artificial technologies, such as sensors (1-1), "smart," molecularly responsive surfaces (1-2) and materials (1-3), synthetic cellular circuits (1-4), and molecular computing (1-5).

Despite the many positive attributes and successful development of technologies based on biological recognition, the artificial biomolecular receptors commonly employed in current bioengineering efforts suffer from several potentially substantial limitations. For example, most technologies developed to date employ single-site binding, in which one receptor binds to one target molecule. The physics of such binding fixes the shape of the input-output (concentration-occupancy) curve of these receptors in such a way that prevents decisive, coordinated responses to subtle changes in the concentration of effector molecules. Natural biosystems, in contrast, often achieve more complex, coordinated behavior via mutually interacting, often hierarchically organized networks of receptors and target

molecules. The ability to quantitatively imitate these complex interactions would enable the construction of more responsive –and likely more effective– biotechnologies, such as biosensors that generate a robust output signal in response to a small change in target molecule concentration, or drug-delivering materials that efficiently deliver their cargo in response to a specific disease-related biomolecule. To date, however, rational methods for the design of artificial systems that quantitatively imitate remain largely unexplored. In response, my thesis focuses most broadly on the development of strategies for the rational design of biomolecular receptors and systems that mimic the more complex (than one receptor binding to one target molecule) receptors and hierarchical materials seen in naturally occurring systems.

Consistent with the above-described, overarching goal of my graduate research, the first aim of my thesis work, detailed in Chapters 2 and 3, focused on the rational introduction of allosteric cooperativity into normally non-cooperative artificial receptors. This mechanism, most famously known to underlie hemoglobin's efficient transport of oxygen, occurs when multiple target molecules bind to a receptor in a more-or-less "all or nothing" fashion. This increases the order of the binding response, thus enhancing the receptors sensitivity to small changes in target molecule concentration. Mechanistically, cooperativity arises when the first target molecule to bind to a receptor shifts the receptor from a low-affinity to a high-affinity conformation, thus increasing affinity for identical target molecules to subsequently bind. In Chapter 2 I describe my initial efforts at the rational introduction of cooperativity into these using a simple model receptor: DNA-detecting molecular beacons. Following this I developed an intrinsic disorder-based strategy by which the thermodynamic properties enabling cooperativity could be introduced into structurally more complex

receptors, which I describe in Chapter 3. Indeed, the approach I demonstrate is of sufficient generality that it can be applied to receptors for which little prior structural information is available.

My second broad aim, which took a different perspective on the engineering of biomimetic, multicomponent bioreceptors, focused on the development of a quantitative understanding of the physics of stimulus-responsive hydrogels. Materials in which multifunctional biomolecular building blocks controllably assemble and dissolve are ubiquitous in nature; for example in transport vesicles, viruses, and cell membranes. As with the imitation of allosteric cooperativity, the ability to rationally imitate the structural and response properties of these materials in an artificial context would be useful in many biotechnologies, for example biofuel cells, drug delivery materials, and biosensors. Although there successful examples of these artificial, stimulus-responsive materials, design efforts thus far have been largely qualitative, and systematics approaches to control the physical and response properties – and thus enable the straightforward design of such materials for technologies purposes - do not exist. Part of the reason for this is that the relationship between properties such as network architecture, affinities and molecular and micron scale behavior, and cooperativity between neighboring biomolecular building blocks are not well understood, and there is a lack of simple, quantitative techniques for measuring the response of these materials. In response, I developed and demonstrated simple, straightforward techniques to measure the dissolution of a model hydrogel at the molecular and micron size scales simultaneously, which I describe in Chapter 4.. I describe this method in Chapter 4. In Chapter 5, I employed these methods to quantitatively characterize the relationship between crosslinker affinity and geometry and response kinetics in a model hydrogel, demonstrating

the ability to quantitatively control the hydrogel's response properties using methods traditionally applied for the tuning of solution-phase DNA and aptamer switches.

1.2 Cooperativity

There are many successful examples of technologies that harness biomolecular recognition (cite a review here?), but these are typically limited by effective sensitivity. The ideal biosensor receptor is one that is highly specific *and* can robustly respond to very small changes in binding targets. A limitation often seen in current biotechnologies is that the physics of the single-site binding fixes the shape of the receptors' input-output curve. Specifically, single-site binding produces a hyperbolic binding curve (the "Langmuir isotherm") fixed in width, such that an 81-fold change in target concentration is required to shift occupancy from 10% to 90%. This fixed width prevents the receptor from robustly responding to small changes in target molecule concentration, which limits their applicability in many important applications. The clinically relevant ranges of many drugs, for example, are as narrow as 4-fold, rendering it difficult to achieve clinically relevant measurement precision using a detection scheme characterized by an 81-fold dynamic range (1-6).

As this fixed dynamic range is inherent in the physics of single site binding, Nature also faces the very real limitations inherent of single-site binding evolution. So challenged, evolution has invented a number of mechanisms, including sequestration, amplification cascades, receptor co-localization, and homotropic allosteric cooperativity, by which the otherwise fixed dynamic range of single-site receptors can be narrowed to optimally respond to molecular cues and thus better ensure the survival of an organism. The ubiquity with

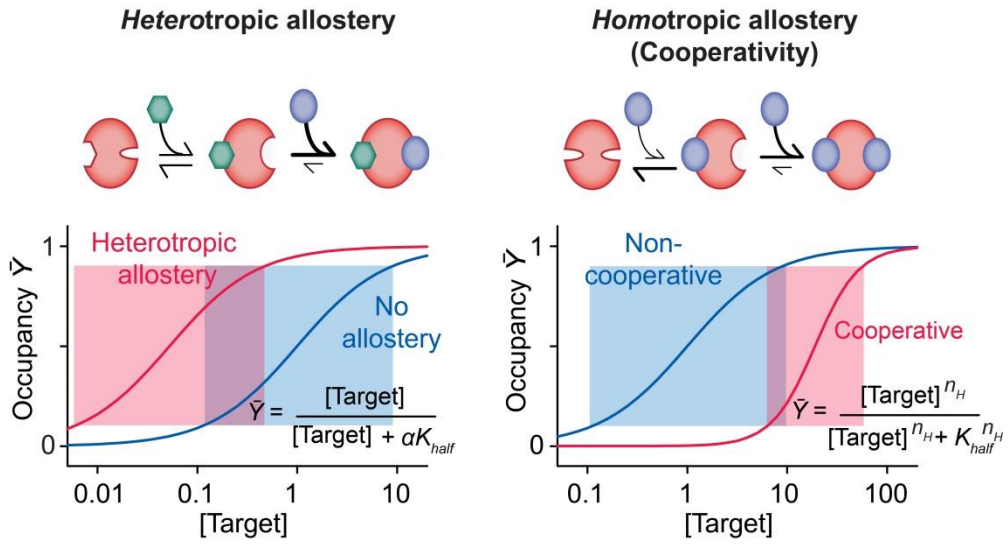

Figure 1-1. Nature often controls the shape and position of ligand–response curves via allostery. (**Left**) In heterotropic allostery, the binding of one ligand to a receptor increases or decreases the affinity with which a second, different ligand binds, shifting the placement of the binding curve without altering its shape and thus without altering the width of its useful dynamic range (shaded boxes) or, in turn, its sensitivity to small changes in target concentration. (**Right**) In homotropic allostery, in contrast, the binding of one copy of target ligand changes the affinity with which additional copies of the same ligand bind, altering both the placement and the shape of the binding curve. The latter effect allows the system to respond more (positive cooperativity) or less (negative cooperativity) sensitively to changes in target ligand concentration. For positive cooperativity, receptor occupancy is a higher (than unity) order function of target concentration, with the exponent, n_H, being known as the Hill coefficient.

which nature employs such mechanisms suggests that they may also be of value in the development of improved biotechnologies. Thus motivated, recent years have seen significant effort to rationally adapt these mechanisms to the protein and nucleic acid-based receptors employed in a number of artificial biotechnologies, with many of the mechanisms nature uses to sensitize receptors to small changes in target molecule concentration having been exploited to improve the responsiveness of biotechnologies, including molecular (1-7) and genetic (1-8) logic gates, ultra-responsive biosensors (1-9), and digital, "all-or-none" drug delivery systems (1-10). Allosteric cooperativity, however, which is arguably the

simplest solution to this problem, has seen adaptation to only a handful of small-molecule and biopolymer-based receptors whose architectures and mechanisms. Even in these successful examples of the introduction of cooperativity into artificial receptors, the thermodynamic principles underlying cooperativity have not been quantitatively explored, nor are these architectures readily applicable to the quantitative introduction of cooperativity into a broad variety of biopolymer receptors.

Although allosteric cooperativity is a simple, elegant mechanism, its underlying thermodynamics are rather subtle and perhaps non-intuitive. The effect occurs when two or more identical ligands bind in an "all or nothing" fashion to a receptor (*Figure 1-1*). This "all or nothing" binding produces a higher order dependence of the binding isotherm on target molecule concentration, such that the dependence on the concentration of the target molecule is raised to a factor known as the Hill coefficient. For non-cooperative receptors, the Hill coefficient is equal to one; for optimally cooperative receptors, the Hill coefficient equals the number of binding sites per receptor, corresponding to completely "all or none" behavior. The higher order of the binding curve in turn produces a steeper transition from unbound to bound receptors, requiring a smaller change in target molecule concentration to produce given changes in the fraction of the receptor's occupancy. Mechanistically, to generate this effect subsequent binding events are coupled such that the first target molecule to bind shifts the receptor from a low-affinity (or binding incompetent) to a high-affinity conformation, such that once an initial target molecule binds, the probability of the second binding is high. Although this mechanism is simple and elegant, engineering a receptor with two different conformations with different affinities and a target molecule-induced shift between them has historically complicated in practice. In fact, Hill-type cooperativity has, arguably, not been

introduced rationally and quantitatively into any previously non-cooperative receptor prior to my work.

1.3 Previous efforts to rationally introduce allosteric cooperativity

The above is not to say that the idea of introducing cooperativity into normally non-cooperative receptors is unprecedented. Indeed, motivated by the obvious value of being able to achieve this several groups had previously attempted the effort with some success. These prior studies, however, are all rather qualitative and empirical, and none provided a thermodynamic or mechanistic framework that could be used to generalize the approach to introduce cooperativity into other receptors.

The majority of the artificial cooperative receptors designed to date are small organic molecules, described in detail in several comprehensive reviews (1-11, 1-12, 1-13). The relative simplicity of these molecules enables the direct design of receptor-target interactions in which either multiple target molecules directly interact or in which the binding of one target molecule fixes the receptor in a conformation that favors a second target molecule binding. As an example of the former, Kikuchi *et al.* (1-14) report the cooperative binding complexation of four alkyl glucopyranoside target molecules to an artificial glycoside receptor composed of a resorcinol cyclic tetramer in hydrophilic solvent. The geometry of the four target complexation sites is such that target molecules complexed to the same tetramer shields their hydrophobic tails from solvent, providing a favorable interaction term aside from that of simple complexation. An early example of the latter, published in 1985 by Rebek Jr *et al.* (1-15), consisted of a synthetic receptor containing two $Hg(CN)_2$–binding crown ether groups connected by a biphenyl skeleton. The idea is that the first $Hg(CN)_2$

target molecule to bind would restrict the conformation of the other crown ether group to a either a binding competent or incompetent conformation, thus generating either positive or negative cooperativity (1-15). Researchers expanded on this work by developing similar receptors to cooperatively bind molecular targets including Hg(II) ions (1-16), Lewis oligosaccharides (1-17), fullerene (1-18), and oxocarbon (1-19). A third class of organic small molecule receptors cooperatively assemble into multi-molecular complexes in response to a target molecule, commonly a metal ion, which mediates interactions between the receptors at multiple sites. Here cooperativity arises because the first target molecule to coordinate the organic receptors forms intact binding sites for the other target molecules. As an example of this, Lehn *et al.* (1-20) describe tridentate oligobipyridine receptors that assemble in the presence of three Cu(I) ions to bridge interactions between the receptors, which as expected assemble cooperatively in the presence of Cu(I) with a Hill coefficient approaching three. Garret *et al.* (1-21) reported a similar cooperative assembly of tris-bipyridine strands in response to Ag(I) ions. Despite multiple successful examples of these small organic molecule cooperative receptors, however, none of these studies quantitatively explore the thermodynamic principles of underlying cooperativity, nor attempt to tune the receptors to achieve explicit control over the dynamic range of binding.

Substantially fewer examples of more complicated artificial cooperative receptors exist, and the majority of these are DNA receptors that employ a metal ion mediated assembly mechanism similar to that of the cooperatively assembling organic helix receptors. These receptors utilize the ability of Hg(II) and Ag(I) ions coordinate thymine-thymine and cytosine-cytosine mismatches, respectively, to form target molecule–inducible base pairs. DNA strands containing several of these mismatches will cooperatively assemble or switch

Cooperative G-quadruplex switches: Kwok *et al.*, 2012

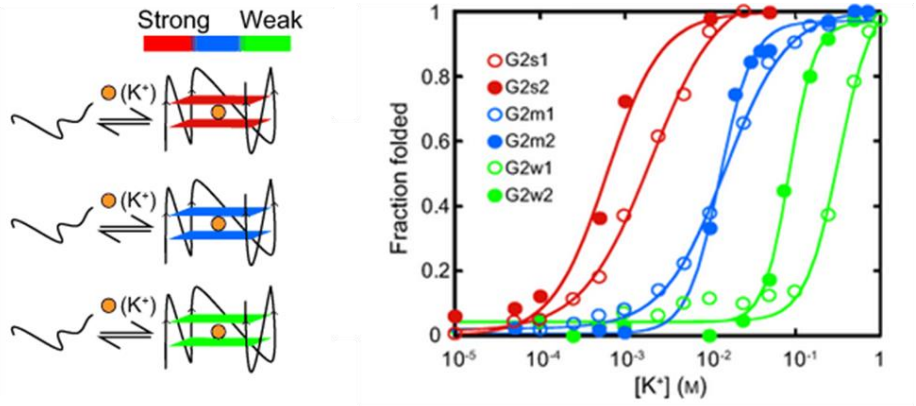

Cooperative SH3-inhibitor: Dueber *et al.*, 2007

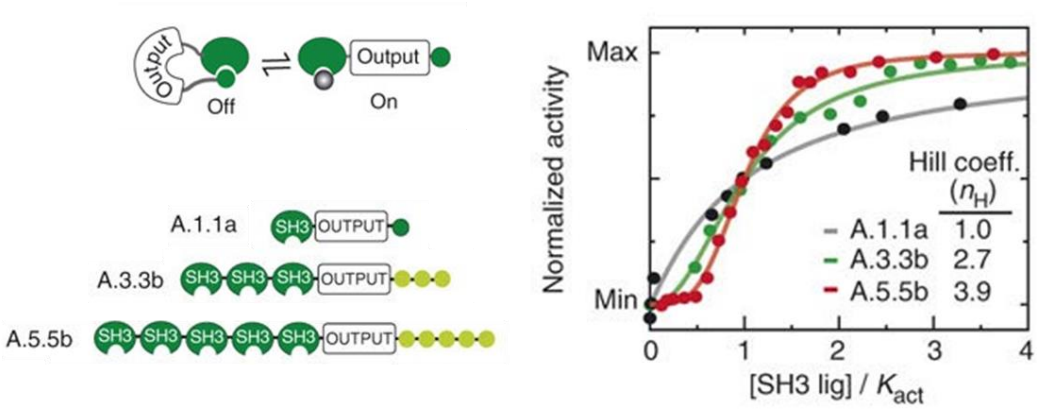

Figure 1-2. Previous designs achieved cooperativity, albeit qualitatively in non-generalizable systems. (**Top**) Kwok *et al.* introduced both positive and negative cooperativity into K^+-binding G-quadruplex receptors. Specifically, they engineered two-site receptors that fold upon binding target molecule, with varying extents of folding cooperativity of between the binding sites. The authors measured high cooperativity in some of their receptors thought to contain the strongest favorable interactions between binding sites; receptors G2m2 (blue solid circles), G2w1 (green empty circles), and G2w2 (green filled circles) achieved Hill coefficients of 2.5 ± 0.4, 2.2 ± 0.3, and 2.7 ± 0.1, respectively. However, these reported values are all substantially above the theoretical two-site maximal cooperativity, suggesting potential error in their experimental methods or analysis. Adapted from (1-24). (**Bottom**) Dueber *et al.* introduced cooperativity into protein switches by coupling repeated catalytically active N-WASP domains with SH3 inhibitor domains. In response to a SH3-binding effector molecule that outcompetes N-WASP's interactions with SH3, the N-WASP domain becomes active. Coupling multiple domains enables a cooperative response, with receptors A.3.3b and A.5.5b achieving Hill coefficients of 2.7 and 3.9. Adapted from (1-26).

into a conformation containing these coordinated mismatches in response to mercury or silver ions. Several successful examples of such artificial receptors that cooperatively switch or assemble in response to Hg(II) or Ag(I) exist. For example, in 2008 Wang *et al.* designed displacement-based Hg(II) sensors consisting one strand containing a fluorophore and several thymines and a weakly complementary adenosine strand containing a fluorophore (1-22). Hg(II) ions mediate "base pairs" between the thymine-thymine mismatches and thus displace the quencher-containing strand. This receptor achieved a Hill coefficient of 2.4 with five Hg(II) binding sites, a modest cooperativity for five binding sites, and no attempts to increase or modulate the cooperativity were discussed. Likewise, in 2013 Porchetta *et al.* developed similar, though more complex, multisite Hg(II)- and Ag(I)-binding receptors with affinity modulated by secondary DNA inhibitors and activators (1-23). While the authors quantitatively tuned the affinity of the switches using the activator and inhibitor, they did not address quantitative aspects or optimize the extent of target-binding cooperativity.

The engineering of artificial cooperative biomolecular receptors whose target molecules bind with mechanisms more complicated than simple coordination-mediated assembly is considerably more difficult than the above, and we are aware of only two such examples in the literature prior to my work (*Figure 1-2*). One of these, published by Kwok *et al.* in 2012, reports the engineering of DNA G-quadruplex receptors that fold to bind two or three potassium ions with either positive or negative cooperativity (1-24). The authors' strategy to achieve this was to tune the stability of the singly bound, partially folded intermediates by tuning the increasing the number of and length between successive guanine-rich G-quadruplex forming stretches. Although the concept of tuning the stability of partially bound conformations to tune cooperativity is perhaps generalizable, in practice controlling

the stability of such intermediates is not generalizable to many other classes of receptors. Moreover, the positively cooperative two-site receptors described by the authors achieve Hill coefficients above the theoretical maximal value of two, suggesting the interpretation of results may be significantly in error. Potentially, the high apparent binding cooperativity arose due to the increase in the ionic strength of the solution with increasing K^+ concentration. All of the cooperative G-quadruplex receptors binding curves have a K_{half} over 10 mM K^+, in the range of salt concentration change that may substantially increase favorable folding free energy (1-25).

The other example of the design of non-coordination-based cooperative receptors, published by Dueber *et al.* in 2007, consisted of tandem repeats of catalytic N-WASP domains connected to repeated inhibitory SH3 modules (1-26; *Figure 1-2, bottom*). In the absence of SH3-binding target molecule, the SH3 modules block the N-WASP domains. Competitively SH3 binding target molecule frees the N-WASP domains, allowing them to be catalytically active. An architecture in which five successive SH3 domains are connected to five N-WASP domains to five SH3 domains achieves a Hill coefficient of 3.9. Although the authors did computationally explore the effects of the strength of SH3/N-WASP interaction and the number of connected domains with the extent of cooperativity, it is not clear how the thermodynamics or mechanism of this architecture could be generalized to other classes of cooperative receptors that do not employ identical inhibitor-competitor geometry.

1.4 The rational engineering of allosteric cooperativity I: cooperative molecular beacons

The aim of the work presented in Chapter 2 (and published in 2014 (*1-27*))) was the quantitative introduction of homotropic allosteric cooperativity into a simple, well-understood, normally non-cooperative model receptor (*Figure 1-3*). The receptor we employed, the molecular beacon, traditionally consists of a short DNA stem-loop. Target DNA complementary to the loop must pay an energetic cost to break the stem. Specifically, to imitate cooperativity in artificial systems, we needed to engineer a two-site molecular beacon that would switch from predominantly a low-affinity or nonbinding state with no target molecule bound, to a high affinity state with one target molecule bound, which would then increase the affinity for a second target molecule to bind. In other terms, the first target molecule to bind must pay an energetic cost to switch the receptor's conformation from high to low affinity.

There are several challenges associated with the design of artificial cooperative receptors. One is that a high-affinity binding event must occur only (to a good approximation) if a lower affinity binding event has already occurred for an identical target molecule on the same receptor. Thus, this high-affinity site must only be available after the first target molecule is bound. Because the target molecules are identical (unlike in heterotropic allostery, in which the target molecules are different), the binding sites cannot be optimized separately. Another challenge is to tune the energetic difference between the first and second target binding events so that the difference in affinities is great enough to generate substantial cooperativity, but that the first binding event is not so unfavorable that the target cannot effectively bind at reasonable concentrations. To determine the optimal

energetic gap, we calculated that for substantial cooperativity (e.g., reducing the dynamic range of binding from 81-fold down to 20-fold) requires that the first binding event be only

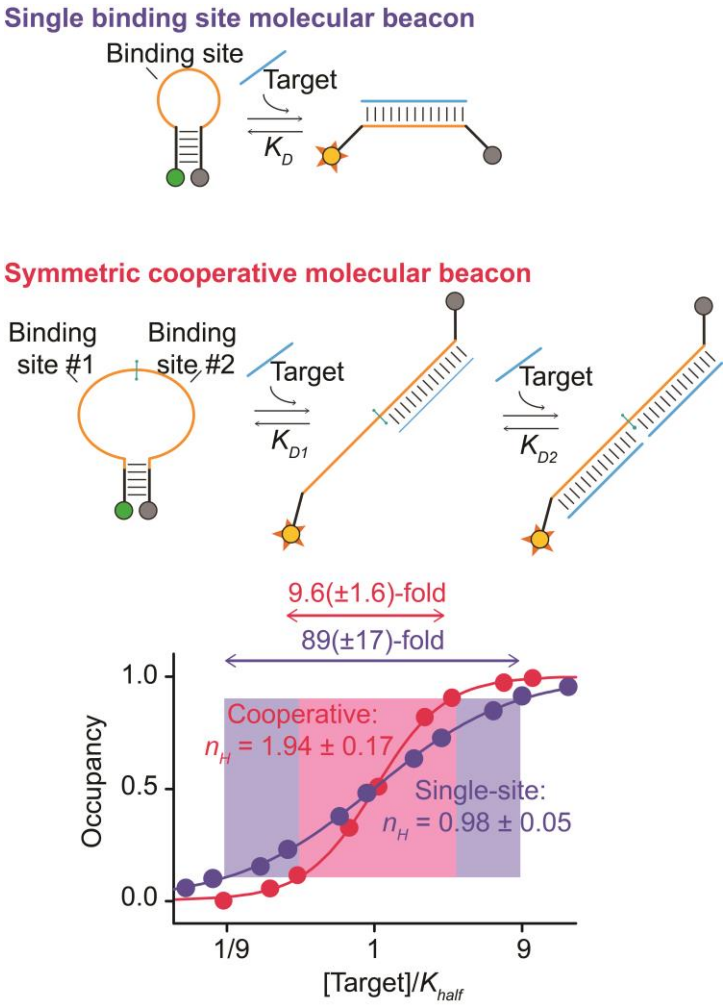

Figure 1-3. (**Top**) As a test bed for our design efforts we use molecular beacons, a commonly employed sensor for the detection of specific nucleic acids. Molecular beacons consist of a short DNA stem-loop. Complementary target molecule can bind to the loop, paying an energetic cost to break the base pairs in the stem. (**Middle**) In our simplest, symmetrical design, we introduced cooperativity into the molecular beacon by introducing a second binding site in the loop. The first target molecule to bind breaks the stem, increasing the affinity for the second to bind. (**Bottom**) The traditional molecular beacon is not cooperative, binding target molecule with a Hill coefficient within error of one (blue). In contrast, our symmetrical cooperative design achieves a Hill coefficient of 1.94 ± 0.17, within error of ideal two-site cooperativity. Adapted from (1-27).

~6 kJ/mol less favorable than the second, corresponding to a 10-fold difference in binding affinities, demonstrating that the engineering of considerable cooperativity is technically feasible. For near perfect cooperativity for a two-site receptor (dynamic range below 10-fold), the difference would have to be ~12-18 kJ/mol, corresponding to a 100-500x difference in binding affinities.

Taking these design rules into consideration, in Chapter 2 of my thesis I describe the successful introduction of Hill-type cooperativity into molecular beacons. My first design, inspired by the heterotropic allosteric cooperative receptor of Porchetta *et al.* (1-28), consisted of a molecular beacon modified with a second binding site in a long stem. The first target molecule to bind to this receptor would partially open the stem, increasing the affinity for the second target molecule to bind the site in the loop. The best of these asymmetrical architectures achieved a Hill factor of 1.5, decreasing the dynamic range of binding from 81-fold to 20-fold. To achieve higher cooperativity I designed a symmetrical molecular beacon with two binding sites in the loop. The first target molecule to bind completely opens the stem, allowing the second target molecule to bind the receptor as easily as it would to single stranded DNA. The cooperativity of this architecture is readily tuned by changing the stability of the stem, and reaches at best cooperativity within error of perfect two-site cooperativity. To confirm the quantitative relationship between binding affinities and cooperativity I employed a heterotropic design based on this symmetrical beacon. I directly measured the relationship between the energetic difference between the high affinity and low affinity states, the first and second binding affinity, and the extent of cooperativity, validating the long-held quantitative understanding of the thermodynamics underlying cooperativity.

1.5 The rational engineering of allosteric cooperativity II: cooperative high complexity receptors

My first work in this area successfully achieved the introduction of cooperativity into a simple model receptor by explicitly designing a high affinity and low affinity conformation and the target molecule induced equilibrium between them. The structural complexity of most receptors, however, renders this very precise engineering well beyond even state of the art biomolecular design efforts. One proposed strategy for evolution to address this challenge, theoretically suggested in 2005 (1-29) and demonstrated experimentally in 2013 (1-30) is to employ multisite, intrinsically disordered receptors that only fold upon binding a target molecule. I employed this strategy to introduce cooperativity into receptors more complex and less structurally understood than molecular beacon receptors. Specifically, I engineered cooperativity into aptamers, DNA sequences that specifically bind small molecule and protein receptors (1-31). To do this, I developed a disorder-based architecture consisting of a tandem repeat of one half of an aptamer receptor, a variable length linker section, and a tandem repeat of the second half of the aptamer receptor (*Figure 1-4, top*). Because the linker is entropically expensive to close, in the absence of target this receptor remains unfolded. The first copy of target molecule to bind pays an energetic cost to close the loop, increasing the favorability of the second target molecule binding. I applied this concept to design three different target molecules with cooperativity in the best of these approaching ideal cooperativity (*Figure 1-4, bottom*). I also developed and verified a predictive theory for how cooperativity scales with favorable closing free energy and loop closure entropy, enabling the rational tuning of the dynamic range of binding.

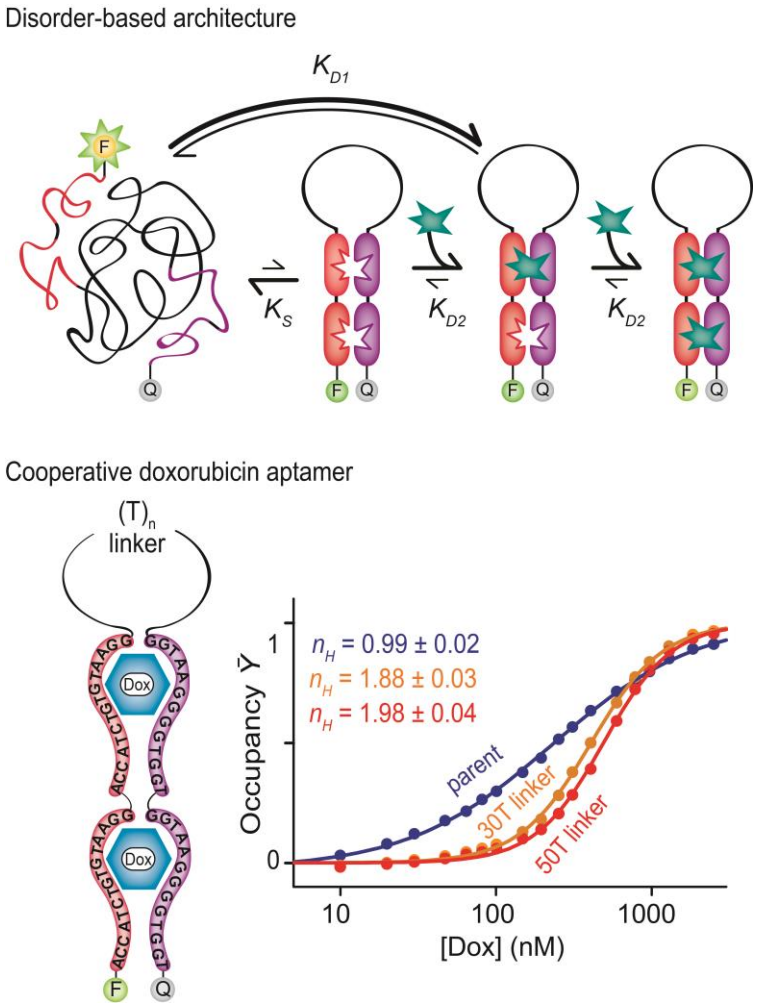

Figure 1-4. (**Top**) Our disordered receptor architectures consist of two copies of one half of a receptor (red), a variable length, unstructured linker (black), and two copies of the second half of the receptor (purple). In the absence of target ligand, the construct exists primarily in a disordered state lacking preformed binding sites. This disordered state, however, is in equilibrium (equilibrium constant, K_S) with the fully folded receptor. The first target molecule to bind must overcome the unfavorable free energy associated with forming this structure, reducing its affinity compared with that of the preformed aptamer by the factor $(1 + K_S)/K_S$. The second target molecule binds to a preformed binding site, thus improving its affinity relative to that of the first binding event. (**Bottom**) We have applied our approach to engineer cooperativity into three different aptamers, including a doxorubicin-binding aptamer, which, although predicted to form a stem loop, is ultimately of unknown structure. (Bottom) Constructs using either 30- or 50-base linkers achieve Hill coefficients of 1.88 ± 0.03 and 1.98 ± 0.04, respectively, corresponding to useful dynamic ranges of 10.4-fold and 9.2-fold. The Hill coefficient of the parent aptamer, in contrast, is within experimental uncertainty of unity. Adapted from (1-31).

1.6 Stimulus-responsive hydrogels

In addition to their importance in ligand binding, cooperativity and multivalency also play an important role in the controlled assembly of many biological materials. Indeed, virtually all biomaterials form not from a single, monolithic piece, but rather an assembly of component biomolecules that interact to form a coherent material with finely tuned mechanical, physical, and chemical properties. In many cases, these materials dynamically and controllably assemble and dissolve where and when they are needed, for example as cell membranes, viral capsids, and transport vesicles. These materials commonly assemble and dissolve in a cooperative, all-or-nothing manner, avoiding wasteful or even harmful partially formed intermediates. Like artificial receptors, the ability to quantitatively design artificial bioinspired, target molecule-responsive biomaterials would be useful in many technologies. For example, these materials would be useful in drug delivery systems that dissolve to release their cargo in response to molecules such as tumor or infection markers, biosensors that form a solid material in response to target molecule.

Given its modular, controllable structure and ability to respond to molecular stimuli, DNA is a natural material for the construction of these responsive hydrogels, and indeed many successful examples of responsive DNA hydrogels exist (1-32, 1-33, 1-34, 1-35). The majority of this prior work, however, has been rather qualitative, focusing on engineering gels with new geometries or responsive to new target molecules, rather than on exploring or controlling the relationship between the gel structure, mechanics, or response thermodynamics or kinetics. Part of the reason for this is that simple methods for quantitatively measuring DNA hydrogel response to target molecules do not exist.

In response, the second broad aim of my thesis work focuses on the development and application of simple, quantitative tools for measuring the response kinetics of DNA hydrogels. Specifically, by labeling a small fraction of the aptamer crosslinkers with a fluorophore-quencher pair, we can quantitatively measure dissolution at the molecular scale. By embedding fluorescent beads with a range of micron-scale diameters in the hydrogel, we can quantitatively measure dissolution at a range of size scales (based on the size of the beads) over time. The use of multichannel imaging to simultaneously visualize the fluorescence of the aptamers and the beads enables the simultaneous measurement of the response kinetics of the hydrogel at both molecular- and micron-length scales, which allows us to probe their relationship. Using these new approaches, I have performed the first reported quantitative measurements of the response kinetics of a model target molecule-responsive DNA hydrogel, significantly improving, as described in Chapter 4, our understanding of these potentially important new materials. Finally, in Chapter 5, I employ this technique to explore the effect of changing the base-pairing length and geometry of the crosslinker on the molecular- and micron- scale kinetics of gel dissolution, a step towards the development of design principles for the construction of gels with specifically tuned dissolution kinetics and thermodynamics.

1.7 Approaches to the high-precision measurement of hydrogel response kinetics

To measure dissolution kinetics at the molecular-scale we measure the fluorescent output of a small amount of fluorophore-quencher labeled aptamer (*Figure 1-5*). In our model hydrogel, an adenosine-binding aptamer binds to two trivalent Y-DNA "monomers,"

which can in turn bind to two other aptamer crosslinkers, forming a coherent network. Thus, in the intact gel, the aptamer takes an extended conformation with the fluorophore and quencher separated, and thus fluorescent output is high. Upon addition of adenosine, the aptamer folds, dissociating from the monomers, bringing the fluorophore and quencher into proximity, and reducing fluorescence. By visualizing the intensity of aptamer fluorescence with confocal microscopy, we can directly measure the extent of molecular-scale dissolution of the gel as a function of time, target molecule concentration, or distance from the surface to which the effector is added. Additionally, further analysis of the images of the intensity pattern of the confocal images over time gives more qualitative information about the mechanism and geometry of dissolution.

To measure the micron-scale dissolution we employ passive rheology, a simple, nondestructive method commonly employed for the measurement of soft materials that relies on measuring the thermally-driven mobility of micron-scale particles embedded in the material (*Figure 1-5*). The intact gel network traps embedded particles such that they remain more-or-less in place. Upon dissolution the bead mobility increases, first remaining in place but moving with slightly more mobility as the network remains intact but becomes softer, than transitioning to Brownian diffusion through a viscous liquid. Measuring the mobility of the beads, quantified by the mean squared displacement over a given time interval, gives a quantitative measurement of the extent of dissolution of the gel at the scale of the bead's size. Employing differently-colored beads and aptamer crosslinker and two-colored confocal microscopy enables the simultaneous measurement of the molecular and micron scale dissolution kinetics.

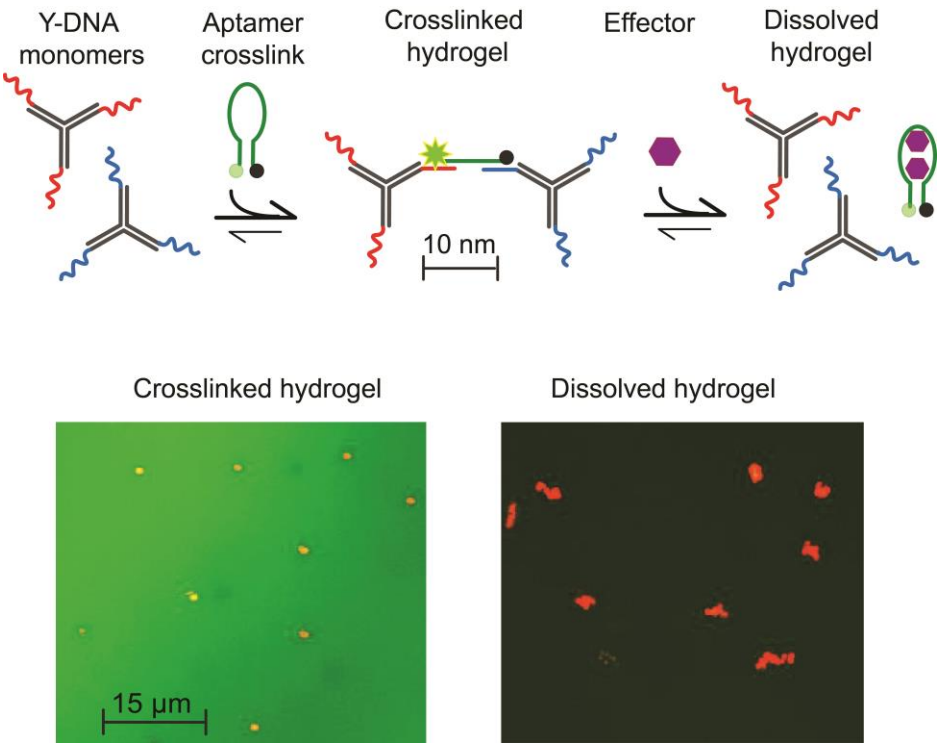

Figure 1-5. As our model system we employed an adenosine-responsive DNA hydrogel modeled on a Y-DNA hydrogel architecture first described by Cheng *et al*. (1-32). (Top) This consists of Y-shaped "monomers" (each consisting of three annealed strands of DNA) with pendant, single-stranded arms. These arms are partially complementary to an adenosine-binding aptamer, which crosslinks the monomers to form a 3-dimensional network. In response to binding its specific molecular effector, adenosine, the aptamer dissociates and folds, disrupting the hydrogel. (Bottom left) This composite image shows the average signal from the aptamer (green channel) and the maximum signal of the beads (red channel) over 20 frames (~33 s), in an intact hydrogel. The fluorophore-quencher pair appended to ~1% of the aptamers is separated, producing high fluorescent output and thus a bright green image. The intact network traps the embedded beads so that they remain in place over the time window of this composite image. (Bottom right) This composite image shows a gel 25 minutes after the addition of 14 mM adenosine over the same time window as left. Upon the addition of adenosine, the aptamer dissociates, decreasing the emission of the fluorphore labeled aptamers, and thus the aptamer-channel signal substantially decreases. The dissociation of the aptamer dissolves the gel network, dramatically increasing bead mobility.

Using this technique, we have measured the effector-induced dissolution of a model hydrogel on the molecular and micron scale under a variety of conditions, giving us a quantitative understanding of the multiscale dissolution physics of our model gel.

Specifically, we demonstrated that both molecular and micron scale dissolution kinetics exhibit an initial lag phase followed by an exponential dissolution phase, and that dissolution rate depends monotonically on both adenosine concentration and the depth below the surface to which we add adenosine (*Figure 1-6*). Notably, our results also showed substantially faster dissolution kinetics at the molecular scale compared to the micron scale, an observation supported by previous experiments (1-37) and theory (1-38). Additionally, we compared the mobility versus time response kinetics for 0.21 μm, 1.0 μm, and 3.2 μm beads and found that the scaled response curves are near identical, suggesting that the gel dissolution response is rather uniform above the ~0.21 μm size scale.

1.8 The control of responsive DNA hydrogel dissolution kinetics

In the final chapter of my thesis work, I employ the multiscale, time-resolved DNA hydrogel measurement technique developed in Chapter 4 to demonstrate the tuning and optimization of the kinetics of our model system. A central advantage to the use of DNA and aptamers in biotechnologies is that their simple, modular base-pairing rules enable the ready tuning and optimization of their thermodynamics and kinetics. That is, the thermodynamics and kinetics of DNA switches may be readily optimized by the addition and subtraction of base pairs, a strategy that is far simpler than what is involved in tuning the thermodynamics and kinetics of other biomolecular (i.e., protein-based) bioengineered systems. While this approach is rather straightforward in one-dimensional (i.e., switch or receptor) systems, it has not been explored in DNA-based materials.

In response, my final thesis chapter explores the effect of changing base pairing length, geometry, and affinity between crosslinker and monomer on the kinetics of responsive DNA hydrogels. Specifically, I have measured the effect of changing the length and position with which the Y-DNA monomers bind adenosine aptamer crosslinker on dissolution kinetics in the model hydrogel that we explored in Chapter 4. The results demonstrate that addition or a subtraction of a single base pair is sufficient to substantially change response kinetics, demonstrating that this method is an effective means of controlling the response of DNA-based materials.

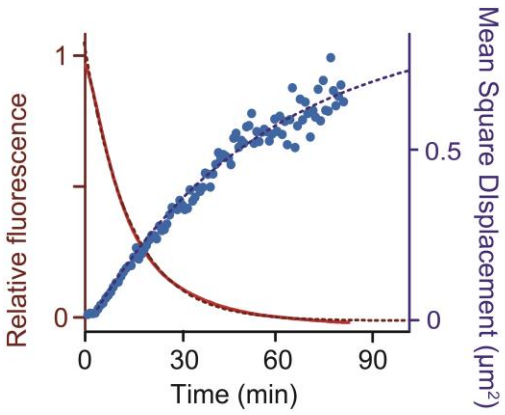

Figure 1-6. We have successfully applied our technique to measure the molecular and micron scale dissolution of DNA hydrogels over time. Above shows the average response kinetics in response to 6 mM adenosine at the molecular scale (red lines) and the 1.0 μm diameter bead scale. Both the molecular-scale and micron scale dissolution response curves are biphasic, with initial lag phases (for the molecular-scale dissolution, see *Figures 4-2* and *4-5* for plot of the response at earlier time scales that better shows this lag phase) and then longer exponential phases. Notably, the micron scale dissolution considerably lags behind the molecular scale dissolution, which is consistent with theoretical predictions.

1.9 Conclusions

Biology has evolved diverse, intricate mechanisms for the effective, robust, and decisive response to molecular stimuli, many of which would be of high value in artificial biotechnologies. Many of these response mechanisms, for example cooperative ligand binding and stimulus-responsive self-assembly, require the finely tuned interplay between multiple biomolecular components. The work presented in this thesis centers on the systematic, quantitative of some of these multivalent, stimulus-responsive biosystems. The design principles developed here will hopefully be useful in the further design and technological application of useful responsive switches and materials.

1.10 References

1-1. Vallée-Bélisle A, Plaxco KW (2010). Structure-switching biosensors: inspired by Nature. *Curr Opin Struct Bio*, **20**:218-526

1-2. Xia F, Jiang L (2008). Bio-inspired, smart, multiscale interfacial materials. *Adv Mater* **20**:2842-2858

1-3. Pasparakis G, Vamvakaki M (2011). Multiresponsive polymers: nano-sized assemblies, stimuli-sensitive gels, and smart surfaces. *Polym Chem* **2**:1234-1248

1-4. Lu TK, Khalil AS, Collins JJ (2009). Next-generation synthetic gene networks. *Nat Biotech* **27**:1139-1150

1-5. Benenson Y (2012). Biomolecular compuing systems: principles, progress, and potential. *Nat Rev Gen*, **13**:455-468

1-6. Setia U, Gross PA (1976). Administration of tobramycin and gentamicin by the intravenous route every 6 hr in patients with normal renal function. *J Infect Dis*, **134**:S125-S129

1-7. Chuang M-C, Windmiller JR, Santhosh P, Valdés-Ramírez G, Katz E, Wang J (2011). High-fidelity determination of security threats via a Boolean biocatalytic cascade. *Chem Commun* **47**:3087-3089

1-8. Bonnet J, Yin P, Ortiz ME, Subsoontorn P, Endy D (2013). Amplfying genetic logic gates. *Science* **340**:599-603

1-9. Ricci F, Vallée-Bélisle A, Plaxco KW (2011). High-precision, in vitro validation of the sequestration mechanism for generating ultrasensitive dose-response curves in regulatory networks. *PLoS Comp Biol* **7**:e1002171

1-10 von Maltzahn G, Park JH, Lin KY, Singh N, Schwöpe C, Mesters R, Berdel WE, Ruoslahti E, Sailor MJ, Bhatia SN (2011). Nanoparticles that communicate in vivo to amplify tumour targeting. *Nat Mater* **10**:545-552

1-11. Shinkai S, Ikeda M, Sugasaki A, Takeguchi M (2001). Positive allosteric systems designed on dynamic supramolecular scaffolds: toward switching and amplification of guest affinity and selectivity. *Acc Chem Res* **34**:494-503

1-12. Zhao Y (2013). Cooperatively enhanced receptors for biomimetic molecular recognition. *Chem Phys Chem* **14**:3878-3885

1-13. Kremer C, Lützen A (2013). Artificial allosteric receptors. *Chem Eur J* **19**:616-6196

1-14. Kikuchi Y, Tanaka Y, Sutarto S, Kobayashi K, Toi H, Aoyama Y(1992). Highly cooperative binding of alkyl glucopyranosides to the resorcinol cyclic tetramer due to intracomplex guest-guest hydrogen-bonding: solvophobicity/solvophilicity control by an

alkyl group of the geometry, stoichiometry, stereoselectivity, and cooperativity. *J Am Chem Soc* **114** 10302 – 10306

1-15. Rebek Jr. J, Costello T, Marshall L, Wattley R, Gadwood RC, Onan K (1985). Allosteric effects in organic chemistry: Binding cooperativity in a model for subunit interactions. *J Am Chem Soc* **107**:7481-7487

1-16. Wang J, Qian X (2006). A series of polyamide receptor based PET fluorescent sensor molecules: positively cooperative Hg2+ ion binding with high sensitivity. *Org Lett* **8**:3721-3724

1-17. Sugasaki A, Sugiyasu K, Ikeda M, Takeuchi M, Shinkai S (2001). First successful molecular design of an artificial Lewis oligosaccharide binding system utilizing positive homotropic allosterism. *J Am Chem Soc* **123**:10239-10244

1-18. Ayabe M, Ikeda A, Kubo Y, Takeuchi M, Shinkai S (2002). A dendritic porphyrin receptor for C60 which features a profound positive allosteric effect. *Angew Chemie* **41**:2790-2792

1-19. Gan Q, Ronson TK, Vosburg DA, Thoburn JD, Nitschke JR (2015). Cooperative loading and release behavior of a metal-organic receptors. *J Am Chem Soc* **137**:1770-1773

1-20. Lehn JM, Rigault A, Siegel J, Harrowfield J, Chevrier B, Moras D (1987). Spontaneous assembly of double-stranded helicates from oligobipyridine ligands and copper(I) cations: structure of an inorganic double helix. *Proc Nat Acad Sci USA*, **84**:2565-2565

1-21. Garret TM, Koert U, Lehn J-M (2004). Binding cooperativity in the self-assembly of double-stranded silver(I) trihelicates. *J Phys Org Chem* **8**:529-532

1-22. Wang Z, Lee JH, Lu Y (2008). Highly sensitive "turn-on" fluorescent sensor for Hg2+ in aqueous solution based on structure-switching DNA. *Chem Commun* 6005-6007

1-23. Porchetta A, Vallée-Bélisle A, Plaxco KW (2013). Allosterically-tunable, DNA-based switches triggered by heavy metals. *J Am Chem Soc* **135**:13238-13241

1-24. Kwok CK, Sherlock ME, Bevilacqua PC (2012). Decrease in RNA folding cooperativity by deliberate population of intermediates in RNA G-quadruplexes. *Angew Chemie* **52**:683-686

1-25. Watkins HM, Vallée-Bélisle A, Ricci F, Makarov DE, Plaxco KW (2012). Entropic and electrostatic effects on the folding free energy of a surface-attached biomolecule: An experimental and theoretical study. *J Am Chem Soc* **134**:3346-3348

1-26. Dueber JE, Mirsky EA, Lim WA (2007). Engineering synthetic signaling proteins with ultrasensitive input/output control. *Nat Biotech* **25**:660-662

1-27. Simon AJ, Vallée-Bélisle A, Ricci F, Watkins HM, Plaxco KW (2014). Using the population-shift mechanism to rationally introduce "Hill-type" cooperativity into a normally non-cooperative receptor. *Angew Chem* **53**:9471-9475

1-28. Porchetta A, Vallée-Bélisle A, Plaxco KW, Ricci F (2012). Using distal site mutations and allosteric inhibition to tune, extend, and narrow the useful dynamic range of aptamer-based sensors. *J Am Chem Soc* **134**:20601-20604

1-29. Hilser VJ, Thompson EB (2007). Intrinsic disorder as a mechanism to optimize allosteric coupling in proteins. *Proc Natl Acad Sci* **104**:8311-8315

1-30. Ferreon AC, Ferreon JC, Wright PE, Deniz AA (2013). Modulation of allostery by protein intrinsic disorder. *Nature* **498**:390-394

1-31. Simon AJ, Vallée-Bélisle A, Ricci F, Watkins HM, Plaxco KW (2014). Intrinsic disorder as a generalizable strategy for the rational design of highly responsive, allosterically cooperative receptors. *Proc Natl Acad Sci USA* **111**:15048–15053

1-32. Cheng E, Xing Y, Chen P, Yang Y, Sun Y, Zhou D, Xu L, Fan Q, Liu D (2009). A pH-triggered, fast-responding DNA hydrogel. *Angew Chem* **121**:7776-7799

1-33. Helwa Y, Dave N, Froidevaux R, Samadi A, Liu J (2012). Aptamer-functionalized hydrogel microparticles for fast visual detection of mercury(II) and adenosine. *ACS App Mater Interfaces* **4**:2228-2233

1-34. Wei X, Tian T, Jia S, Zhu Z, Ma Y, Sun J, Lin Z, Y CJ (2015). Target-responsive DNA-hydrogel mediated "stop-flow" microfluidic paper-based analytic device for rapid, portable, and visual detection of multiple targets. *Anal Chem* **87**:4275-4282.

1-35. Zhang L, Lei J, Liu L, Li C, Ju H (2013). Self-assembled DNA hydrogel as switchable material for aptamer-based fluorescent detection of protein. *Anal Chem* **85**:11077-11082

1-36. Guo W, Qi X-J, Orbach R, Lu C-H, Freage L, Mironi-Harpaz I, Seliktar D, Yang H-H, Willner I (2014). Reversible Ag^{+}-crosslinked DNA hydrogels. *Chem Commun* **50**:4065-4068

1-37. Larsen TL, Furst EM (2008). Microrheology of the liquid-solid transition during gelation. *Phys Rev Lett E* 146001

1-38. Broedersz CP, Mao X, Lubensky TC, MacKintosh FC (2011). Criticality and isostaticity in fibre networks. *Nat Phys* **7**:983-989

2. USING THE POPULATION-SHIFT MECHANISM TO RATIONALLY INTRODUCE "HILL-TYPE" COOPERATIVITY INTO A NORMALLY NON-COOPERATIVE RECEPTOR

Allosteric cooperativity, which nature uses to improve the sensitivity with which biomolecular receptors respond to small changes in ligand concentration, could likewise be of use in improving the responsiveness of artificial biosystems. Thus motivated, we demonstrate here the rational design of cooperative molecular beacons, a widely employed DNA sensor, using a generalizable population-shift approach in which we engineer receptors that equilibrate between a low-affinity state and a high-affinity state exposing two binding sites. Doing so we achieve cooperativity within error of ideal behavior, greatly steepening the beacon's binding curve relative to that of the parent receptor. The ability to rationally engineer cooperativity should prove useful in applications such as biosensors, synthetic biology and "smart" biomaterials, in which improved responsiveness is of value. This work was published in 2014 in *Angew Chem* (2-1).

2.1 Motivation

The ability to respond sensitively to small changes in a molecular input is critical to many biological processes. Such ability allows cells and organisms to react to subtle molecular cues and to convert complex input signals into decisive, effectively binary outputs (2-2). An enhanced ability to detect small changes in molecular concentration would likely

also prove of value in many biotechnologies. The ratio between an effective dose and a toxic dose of some drugs, for example, can be as little as 4-fold (2-3) and thus to measure these with clinically-relevant precision requires sensors that respond robustly to small changes in drug concentration.

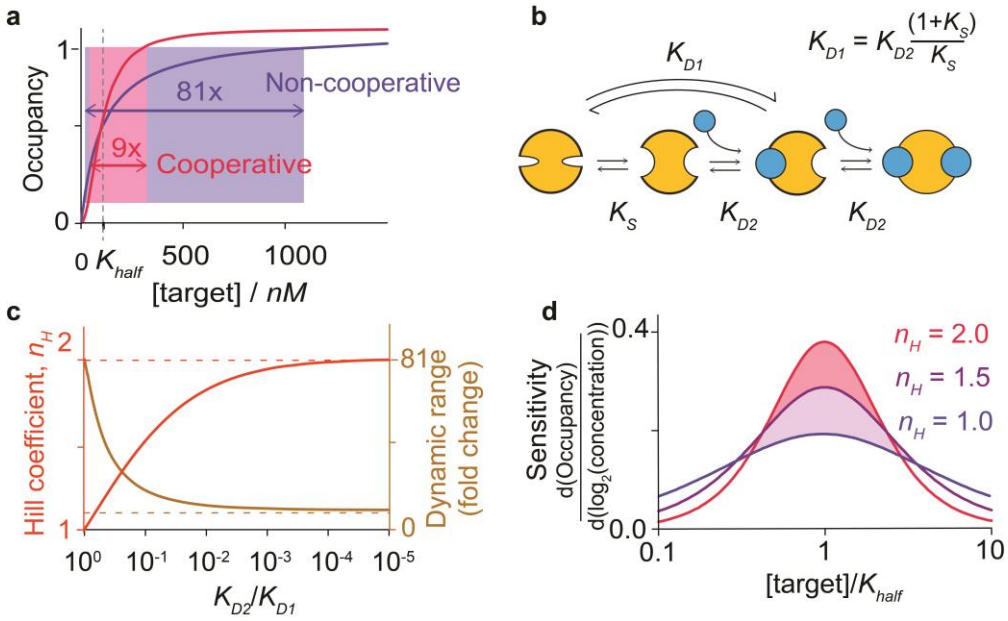

Figure 2-1. (***a***) Allosteric ("Hill-type") cooperativity provides a means of overcoming the 81-fold dynamic range of single site receptors (red) to produce steeper, more responsive behavior (blue). Cooperativity arises when multiple binding sites interact such that the first binding event improves the affinity of subsequent binding events. (***b***) To design this we employ the population-shift mechanism, in which the first binding event is coupled to an unfavorable conformational change, reducing its affinity (K_{D1}) relative to that of the second binding event (K_{D2}). (***c***) While maximal cooperativity (dashed lines) is only achieved if the second binding event is infinitely more favorable than the first, near-ideal behavior is rapidly approached as the relative affinity of the subsequent binding event rises. (***d***) Even modest cooperativity significantly improves sensitivity to small changes in concentration (shown here as the relative change in occupancy per two-fold change in target concentration).

Driven by the advantages associated with enhanced molecular responsiveness evolution has invented a number of mechanisms, including sequestration, amplification

cascades, and receptor co-localization, by which the relative insensitivity of single-site receptors (e.g., they require an 81-fold concentration change to transition from 10% to 90% occupancy) can be overcome (2-2). To date many of these mechanisms have been exploited to improve the responsiveness of biotechnologies ranging from molecular (2-4) and genetic (2-5) logic gates to ultra-responsive biosensors (2-6, 2-7) and digital, "all-or-none" drug-delivery systems (2-8, 2-9). Allosteric cooperativity, however, which is arguably the simplest solution to this problem (2-10, 2-11) has seen adaptation to only a handful of small-molecule (2-12, 2-13) and biopolymer-based receptors (2-14, 2-15, 2-16, 2-17). Here we explore and articulate design principles underlying this mechanism by engineering it into a normally non-cooperative receptor, thus improving its ability to respond to subtle concentration changes.

2.2 Thermodynamic underpinnings of cooperativity

The occupancy of an allosterically cooperative receptor goes as

$$\frac{[complex]}{[complex]+[free\ receptor]} = \frac{[target]^{n_H}}{[target]^{n_H} + K_{Half}^{n_H}} \qquad \textbf{(2-1)}$$

where K_{Half} is the concentration at which half of all binding sites are occupied and n_H, the "Hill coefficient," provides a convenient metric of cooperativity: a system is non-cooperative at n_H = 1, and approaches maximum cooperativity as n_H approaches the number of binding sites on the receptor (2-18). (Note: here we discuss positive cooperativity, which steepens the binding curve. Negative cooperativity, in contrast, broadens the curve; e.g., ref (2-14)). The resultant higher order dependence on concentration narrows the range over which a receptor transitions from largely unbound to largely bound, increasing the robustness of its response to small changes in input (*Figure 2-1a).* Specifically, the width of a receptor's dynamic range

(defined conventionally as the ratio of the target concentrations at which occupancy is 90% and 10%, C_{90} and C_{10}, respectively) is related to the Hill coefficient by (2-19, 2-20, 2-21)

$$Dynamic\ Range = \frac{C_{90}}{C_{10}} = 81^{1/n_H} \quad \textbf{(2-2)}$$

The dynamic range thus collapses from 81-fold for a non-cooperative receptor to just 9-fold for a maximally cooperative, two-site analogue, significantly enhancing the extent to which receptor occupancy changes with small changes in target concentration.

Allosteric cooperativity is achieved when the binding of one copy of a target molecule improves the affinity with which subsequent copies of the same molecule bind to other, distal, sites on the same receptor (*Figure 2-1b*), changing in turn the *shape* of the binding curve (*Figure 2-1a*) (2-22, 2-23, 2-24). Cooperativity, also called *homo*tropic allostery (all sites bind identical molecules), thus differs from *hetero*tropic allostery (sites bind different molecules), which instead alters the *placement* (i.e., midpoint) of the binding curve without changing its underlying shape. While extensive literature exists regarding the design of heterotropically allosteric receptors (2-25, 2-26, 2-27), the rational design of cooperativity has seen relatively little success (2-12, 2-13, 2-14, 2-15, 2-16, 2-17), perhaps because details of the mechanism render its design rather non-intuitive. First, the all-or-nothing effect of cooperativity requires the creation of systems in which a *higher* affinity site is occupied only *after* a lower affinity site that binds the *same ligand* is already filled. Second, in contrast to heterotropic allostery, homotropic allostery occurs at binding sites that are identical or near identical, and thus it requires perhaps more finesse to alter the affinity of one independently of the others.

2.3 Design approaches and results

Given the above arguments our goal is to design multi-site receptors for which the affinity of the first binding event is poorer than that of subsequent binding events. To achieve this we have employed the population-shift mechanism (see, by analogy, refs (2-16, 2-28)). That is, we have designed receptors that interconvert between two conformations, the more stable of which is "closed," exhibiting low affinity for the target, and the less stable of which is "open," exposing multiple high affinity binding sites (*Figure 2-1b*). The first binding event shifts the conformational equilibrium "up-hill" toward the latter, higher affinity state. As subsequent binding events need not "pay the cost" associated with this unfavorable conformational change, their affinity is enhanced relative to that of the first, producing a cooperative response. For the simplest case of a receptor opening to expose two identical binding sites, the dissociation constant of the first binding event, K_{D1}, will be higher (i.e., poorer affinity) than that of the second, K_{D2}, by the relationship

$$K_{D1} = K_{D2}\frac{1+K_S}{K_S} \qquad \textbf{(2-3)}$$

where K_S is the equilibrium constant for the shift between the closed and open conformations. The extent of cooperativity, in turn, depends on the ratio of the affinities of the binding events by (2-29)

$$n_H = \frac{2}{1+\sqrt{K_{D2}/K_{D1}}} \qquad \textbf{(2-4)}$$

From this relationship it is apparent that maximum cooperativity (n_H equals the total number of binding sites) is only achieved when subsequent binding events are infinitely more favorable than the first (i.e., $K_{D2} << K_{D1}$). Fortunately for our design efforts, however, the

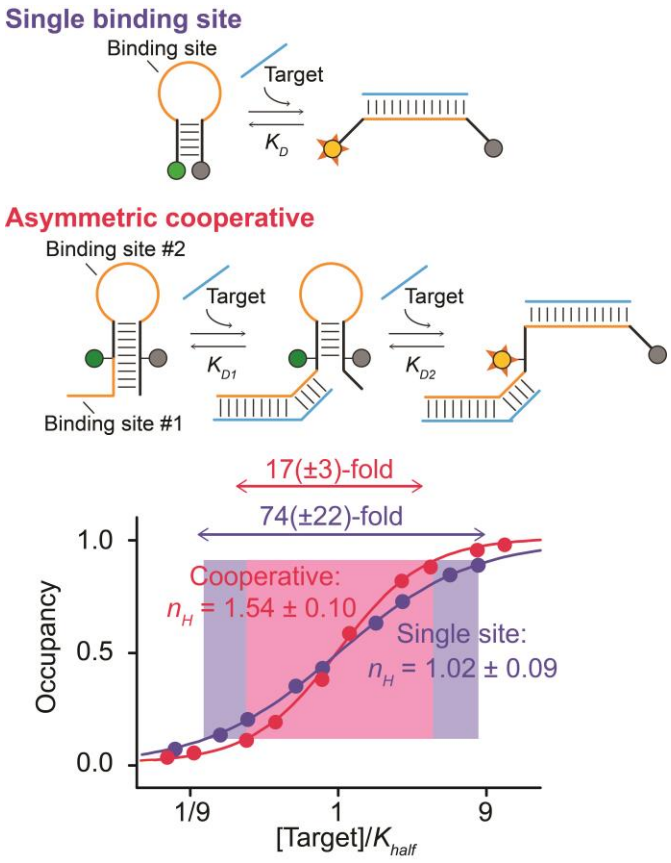

Figure 2-2. (***Top***) As a test bed for our design efforts we use molecular beacons, a commonly employed sensor for the detection of specific nucleic acids (2-30, 2-31, 2-32, 2-33). (***Middle***) To introduce cooperativity we added a second binding site contained partially within the 5' strand of the stem and partially within an appended single-stranded tail. Binding to either site disrupts the stem, pushing the conformational equilibrium towards the higher affinity state. (***Bottom***) The binding of an unmodified molecular beacon is not cooperative, producing a Hill coefficient (n_H) and dynamic range within error of the 1 and 81-fold values expected. The tailed beacon, in contrast, achieves a Hill coefficient of 1.54±0.10, shrinking the dynamic range to 17(±3)-fold. Error estimates here and elsewhere reflect estimated 95% confidence intervals.

asymptotic approach towards maximal cooperativity (*Figure 1c)* and, thus, maximum responsiveness (*Figure 2-1d*) is rapid. Specifically, a two-site receptor achieves a Hill coefficient of 1.5 when the ratio K_{D2}/K_{D1} reaches just 0.1 (i.e., when, at 37˚C, the gap between the binding events is only 6 kJ/mol). This reduces the receptor's dynamic range

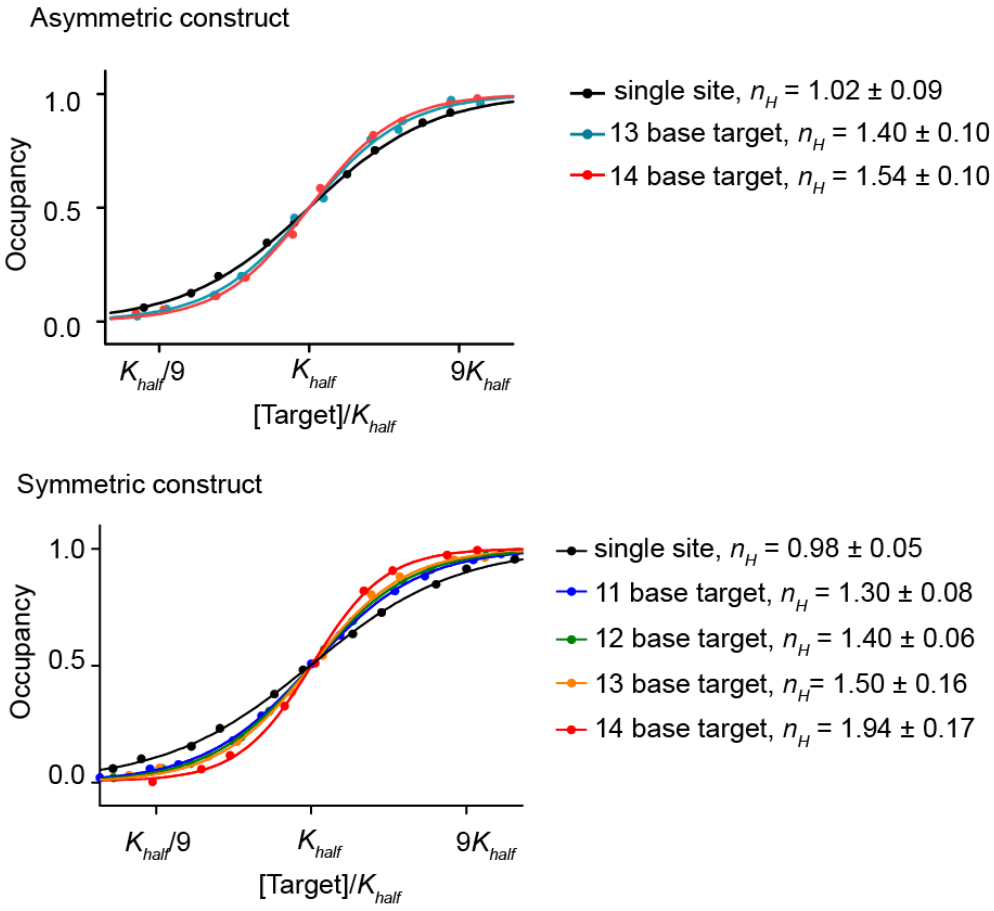

Figure 2-3. Increasing target hybridization lengths monotonically increase cooperativity. This most likely occurs because a longer target molecule is able to more completely pay the energetic cost to shift the receptor from low-affinity to high-affinity conformations, thus achieving an optimally wide gap between the first and second binding affinity. (***Top***) For the asymmetrical beacon the 13-base target achieves a Hill coefficient of 1.40 ± 0.10, while the 14-base target achieves a Hill coefficient of 1.55 ± 0.10. (***Bottom***) For the symmetric beacon, the Hill coefficient monotonically increases from 1.30 ± 0.08 with an 11-base target to 1.94 ± 0.17 with a 14-base target.

from 81-fold to just 19-fold, significantly increasing sensitivity to small changes in target concentration.

As our design test bed we have employed molecular beacons (2-30), a widely used optical (2-31, 2-32) and electrochemical (2-33) sensor for the detection of DNA and RNA. Molecular beacons are DNA molecules containing self-complementary ends and modified on their termini with an optically reporting fluorophore-quencher pair (*Figure 2, top*). In the absence of target the beacon's ends hybridize to form a stem-loop that brings its reporters into proximity, reducing fluorescence. Hybridization of the loop to a complementary target sequence breaks the stem, separating the repofrters and increasing their output. As expected, the binding of a "traditional," molecular beacon is non-cooperative, exhibiting a Hill coefficient of 1.02±0.09 and a dynamic range of 74(±22)-fold, values within error of those predicted for single-site binding (*Figure 2-2, bottom*).

Our first design efforts were inspired by a previous, *hetero*tropically allosteric beacon in which the binding of one molecule controls the affinity of a second, different target molecule, shifting the midpoint of the binding curve without changing its shape (2-25). This consists of a stem-loop containing one binding site in its loop and a second partially within a single-stranded tail and partially within the beacon's double-stranded stem. The binding of a target molecule to either the tail or the loop weakens the stem, shifting the beacon's population toward the open, binding-competent conformation and improving the affinity with which the second ligand binds. Here we have made the two binding sites identical (*Figure 2-2, middle*), rendering the beacon cooperative and producing a steeper, more responsive curve than seen for either the parent or the heterotropically allosteric beacon. Against a 14-base target, for example, that overlaps with five (of nine) bases in the stem the tailed beacon

achieves a Hill coefficient of 1.54±0.10 and, correspondingly, a dynamic range of 17(±3)-fold (*Figure 2-2*, *bottom*). In contrast a 13-base target overlapping with just 4 bases in the stem (thus producing a smaller energy gap), produces a Hill coefficient of only 1.40±0.10 and a dynamic range of 23(±6)-fold (*Figure 2-3*, *top*).

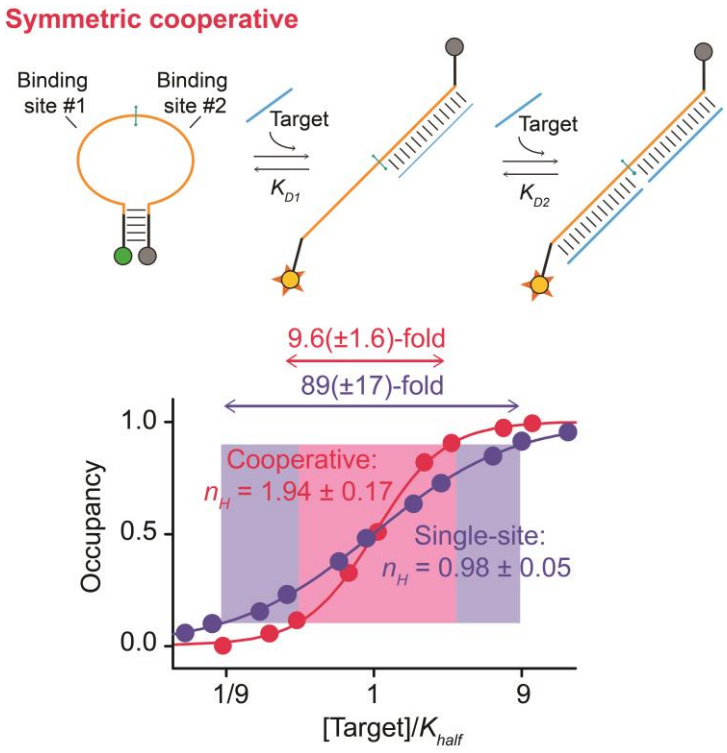

Figure 2-4. (***Top***) Our second design places two target-binding sites within the beacon's single-stranded loop, rendering it possible to stabilize the stem (i.e., increase the energy gap between the two binding events) without altering specificity. (***Bottom***) Using a rather stable stem and a 14-base target this achieves a Hill coefficient of 1.94±0.17 and a dynamic range of 9.6(±1.6)-fold, within error of ideal behavior. Shorter targets and/or less stable stems reduce cooperativity by reducing the energy gap between the first and second binding events (*Figures 2-4*, *2-6*).

To achieve performance closer to the theoretical maximum it is necessary to increase the energy gap between the first and second binding events (i.e., to decrease K_S), which can be done by altering the stability (sequence), of the stem (2-28). The stem of the tailed beacon,

however, also serves as part of a target-binding site and thus altering it would also change the beacon's specificity. To circumvent this we designed a second, "symmetric" cooperative beacon that places two identical binding sites within the single-stranded loop with only minor stem overlap with the stem (*Figure 2-4*, *top*). Because the persistence length of double-stranded DNA is long (2-33) the strain associated with the binding of even a single target

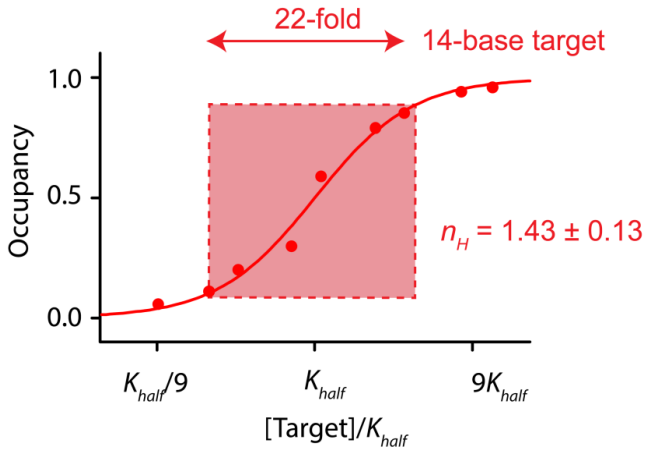

Figure 2-5. Decreasing the stability of the symmetrical beacon by removing a single GC base pair substantially decreases cooperativity, reducing the Hill coefficient achieved by the beacon from within error of two to 1.43 ± 0.13.

molecule to this loop destabilizes the stem and shifts the population towards the high-affinity conformation, improving the affinity of the second binding event. Furthermore, we can "tune" the energy gap between the two dissociation constants by altering the sequence or length (and thus stability) of the stem without altering the specificity of the two target binding sites. Using a stable six base-pair, GC-rich stem for which K_S = 0.0025 at 39°C) this construct achieves a Hill coefficient of 1.94±0.17 and a dynamic range of 9.6(±1.6)-fold (for a 14-base target), values within error of those expected for a perfectly cooperative two-site receptor (*Figure 2-4*, *bottom*). Weakening the stem by removing a single GC base pair raises

K_S to ~0.14, reducing the Hill coefficient to 1.43±0.13, and broadening the dynamic range to 22(±6)-fold (*Figure 2-5*).

2.4 Validation of the theoretical underpinnings of cooperativity

The symmetry of the latter beacon renders it a convenient platform with which to dissect the thermodynamics underlying our design. To do so we have explicitly measured K_{D1} and K_{D2}, the affinities of the first and second binding events using a control construct identical to the symmetric beacon save that the binding sites differ in sequence (Figure 2-6a). This provides a means of verifying equation 4, the theoretical relationship between the Hill coefficient and the ratio of binding affinities. For example, plugging the K_{D1} and K_{D2} observed for this control construct (at 39˚C; *Figure 2-6b*) into equation 3 predicts n_H = 1.88, which is within the error of the 1.94±0.17 observed for the equivalent symmetric beacon under the same conditions (*Figure 2-4*, *bottom*). Conducting this experiment over a range of temperatures, which alters the conformational equilibrium constant and in turn, K_{D1}, we find that, as expected, this relationship holds even as the ratio of affinities varies over orders of magnitude. Specifically, as K_S decreases monotonically from 0.78 (at 58˚C) to 0.0025 (at 39˚C) the receptors shift monotonically from effectively single-site behavior to near-perfect two-site cooperativity (*Figures 2-6c*, *2-7*).

2.5 Conclusions

A number of bioinspired mechanisms have been used to enhance the precision of biosensors (2-5, 2-6) and to improve the responsiveness of drug delivery systems (2-8, 2-9),

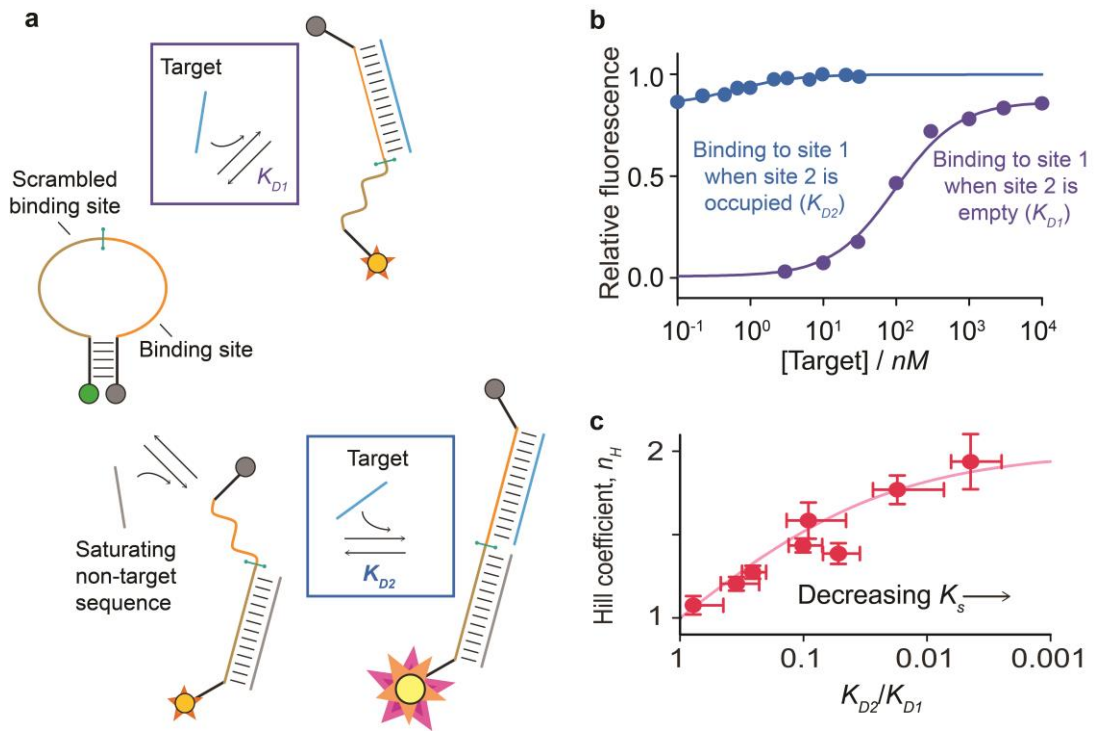

Figure 2-6. (***a***) The modular structure of our symmetric cooperative beacon allows exploration of the thermodynamics underlying its design. To do so we employed a construct in which the two ligand binding sites are distinct, allowing independent measurement of K_{D1} and K_{D2}. (***b***) Shown are the affinities (at 39˚C) measured when the other binding site is empty (purple), and when it is occupied (blue); note that, the latter occurs on a beacon that is already largely open, and thus produces only a fifth of the total signal change. The affinities obtained from this control predict n_H = 1.88 for our sensor (eq. 2-3), within experimental error of the observed value (*Figure2- 4*). (***c***) Measuring K_{D2}, K_{D1} (using the control construct), and n_H (using the cooperative beacon) over a range of temperatures we find that the expected relationship between these values (eq. 2-3) holds even as the ratio of the binding affinities varies over orders of magnitude.

synthetic biology "circuits,"(2-5) and molecular logic gates (2-4). To date, however, Hill-type cooperativity, a simple mechanism by which biology enhances the cell's ability to sense small changes in the concentration of molecular cues (2-2), has seen little use in artificial biosystems. In response we have demonstrated here the utility of employing the population-shift mechanism to rationally introduce cooperativity into molecular beacons, greatly increasing the sensitivity with which they respond to subtle changes in molecular concentration. We note in closing that the modular structure of molecular beacons may

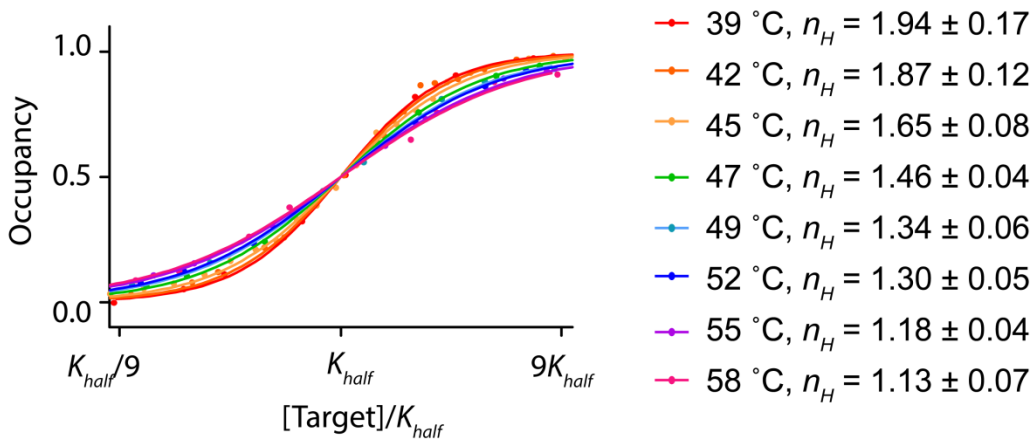

Figure 2-7. Increasing temperature decreases the stability of the symmetrical beacon's stem and in turn the cooperativity. Cooperativity decreases monotonically from 1.94 ± 0.17 at 39 °C to 1.13 ± 0.07 at 58 °C.

render their re-engineering particularly straightforward. We nevertheless believe the design strategies described here will prove general. That is, the principles that the population shift mechanism provides a ready route to cooperativity, and that the switching equilibrium constant need only be of order 0.1 to generate significantly improved responsiveness, will be generalizable to other receptors. For example, a large body of literature already demonstrates the rational introduction of binding-induced conformational changes into normally static biomolecules (2-25, 2-26, 2-27), suggesting that, although design details may differ, cooperativity could similarly be introduced into a range of receptors via mechanisms such as, for example, binding-induced folding.

2.6 Experimental Materials and Methods

Symmetric cooperative molecular beacon targets:

14-base target: 5’ GTAAGACAGTGAACC

13-base target: 5’ TAAGACAGTGAAC

12-base target: 5’AAGACAGTGAAC

11-base target: 5’AGACAGTGAAC

Control (non-cooperative) two-site molecular beacon:

5’ (FAM) GGTGGGCTTGAGTCTCTTAGTTCACTGTCTTACCCACC

Control target sequence:

5’ TAAGAGACTCAAG

We collected all fluorescence measurements using a Cary Eclipse Fluorimeter (Varian) with excitation at 485 (± 5) nm and acquisition at 515 (± 5) nm. We performed all measurements in 150 mM sodium chloride, 50 mM sodium phosphate buffer pH 7. All measurements were conducted at 39˚C unless otherwise noted. We incubated all samples for at least 15 minutes with each target concentration at the appropriate temperature prior to taking measurements; kinetic traces collected at all target concentrations indicate that this is more than sufficient to achieve equilibration. To determine the Hill coefficient, we measured fluorescence at five replicate points per titration. We used GraphPad Prism plotting software to fit the traces to

the Hill equation. Error bars represent 95% confidence intervals based on standard errors derived from the fits.

2.7 References

2-1. Simon AJ, Vallée-Bélisle A, Ricci F, Watkins HM, Plaxco KW (2014). Using the population-shift mechanism to rationally introduce "Hill-type" cooperativity into a normally non-cooperative receptor. *Angew Chem* **53**:9471-9475

2-2. Zhang Q, Bhattacharya S, Andersen ME (2013). Ultrasensitive response motifs: basic amplifiers in molecular signalling networks. *Open Biol* **3**:130031

2-3. Setia U, Gross PA (1976). Administration of tobramycin and gentamicin by the intravenous route every 6 hr in patients with normal renal function. *J Infect Dis* **134**:S125–S129

2-4. Chuang M-C, Windmiller JR, Santhosh P, Valdés-Ramírez G, Katz E, Wang J (2011). High-fidelity determination of security threats via a Boolean biocatalytic cascade. *Chem Commun* **47**:3087-3089

2-5. Bonnet J, Yin P, Ortiz ME, Subsoontorn P, Endy D (2013). Amplfying genetic logic gates. *Science* **340**:599-603

2-6. Katz E, Wang J, Privman M, Halámek J (2012). Multianalyte digital enzyme biosensors with built-in Boolean logic *Anal Chem* **84**:5463-5469

2-7. Ricci F, Vallée-Bélisle A, Plaxco KW (2011). High-precision, in vitro validation of the sequestration mechanism for generating ultrasensitive dose-response curves in regulatory networks. *PLoS Comp Biol* **7**:e1002171

2-8. MacEwan SR, Chilkoti A (2012). Digital switching of local arginine density in a genetically encoded self-assembled polypeptide nanoparticle controls cellular uptake. *Nano Lett* **12**:3322-3328

2-9. von Maltzahn G, Park JH, Lin KY, Singh N, Schwöpe C, Mesters R, Berdel WE, Ruoslahti E, Sailor MJ, Bhatia SN (2011). Nanoparticles that communicate in vivo to amplify tumour targeting. *Nat Mater* **10**:545-552

2-10. Whitty A (2008). Cooperativity and Biological complexity. *Nat Chem Biol* **4**:435-439

2-11. Perutz MF, in I Wish I'd Made You Angry Earlier, Cold Spring Harbor Press 1988

2-12. Kikuchi Y, Tanaka Y, Sutarto S, Kobayashi K, Toi H, Aoyama Y(1992). Highly cooperative binding of alkyl glucopyranosides to the resorcinol cyclic tetramer due to

intracomplex guest-guest hydrogen-bonding: solvophobicity/solvophilicity control by an alkyl group of the geometry, stoichiometry, stereoselectivity, and cooperativity. *J Am Chem Soc* **114**:10302 – 10306

2-13. Wang J, Qian X (2006). A series of polyamide receptor based PET fluorescent sensor molecules: positively cooperative Hg2+ ion binding with high sensitivity. *Org Lett* **8**:3721-3724

2-14. Kwok CK, Sherlock ME, Bevilacqua PC (2013). Decrease in RNA folding cooperativity by deliberate population of intermediates in RNA G-quadruplexes. *Angew Chem* **52**:683-686

2-15. Dueber JE, Mirsky EA, Lim WA (2007). Engineering synthetic signaling proteins with ultrasensitive input/output control. *Nat Biotech* **25**:660-662

2-16. Porchetta A, Vallée-Bélisle A, Plaxco KW, Ricci F (2012). Using distal site mutations and allosteric inhibition to tune, extend, and narrow the useful dynamic range of aptamer-based sensors. *J Am Chem Soc* **134**:20601-20604

2-17. Wang Z, Lee JH, Lu Y (2008). Highly sensitive "turn-on" fluorescent sensor for Hg2+ in aqueous solution based on structure-switching DNA. *Chem Commun* 6005-6007

2-18. Hill AV (1910). The possible effects of the aggregation of the molecules of hæmoglobin on its dissociation curves. *J Physiol* **40**: *IV–VII*

2-19. Goldbeter A, Koshland Jr DE (1981). An amplified sensitivity arising from covalent modification in biological systems. *Proc Natl Acad Sci USA* **78**: 6840-6844

2-20. Goldbeter A, Koshland Jr DE (1982). Sensitivity amplification in biochemical systems. *Q Rev Biophys* **15**:555-591

2-21. Ferrell Jr JE (1996). Tripping the switch fantastic: how a protein kinase cascade can convert graded inputs into switch-like outputs. *Trends Biochem Sci* **21**:460-466

2-22. Monod J, Wyman J, Changeux J-P (1965). On the nature of allosteric transitions: A plausible model. *J Mol Biol* **12**:88–118

2-23. Koshland DE, Nemethy G, Filmer D (1996). Comparison of experimental binding data and theoretical models in proteins containing subunits. *Biochemistry* **5**:365-385

2-24. Pauling L (1935). The oxygen equilibrium of hemoglobin and its structural interpretation. *Proc Natl Acad Sci USA* **21**:186-191

2-25. Ricci F, Vallée-Bélisle A, Porchetta A, Plaxco KW (2012). Rational design of allosteric inhibitors and activators using the population-shift model: in vitro validation and application to an artificial biosensor. *J Am Chem Soc***134**: 15177-15180

2-26. Strickland D, Moffat K, Sosnick T (2008). Light-activated DNA binding in a designed allosteric protein. *Proc Natl Acad Sci USA* **105**:1070-10714

2-27. Radley TL, Markowska AI, Bettinger BT, Ha J-H, Loh SN (2003). Allosteric switching by mutually exclusive folding of protein domains. *J Mol Biol* **332**:529-536

2-28. Vallée-Bélisle A, Ricci F, Plaxco KW (2009). Thermodynamic basis for the optimization of binding-induced biomolecular switches and structure-switching biosensors. *Proc Natl Acad Sci USA* **106**:13802-13807

2-29. Dahlquist FW (1978). The meaning of Scatchard and Hill plots. *Meth Enzymol* **48**:270-299

2-30. Tyagi S, Kramer FR (1996). Molecular beacons: probes that fluoresce upon hybridization. *Nat Biotechnol* **14**:303-308

2-31. Kim Y, Sohn D, Tang W. Molecular beacons in biomedical detection and clinical diagnosis. *Int J Clin Exp Pathol* **1**:105-116

2-32. Tyagi S, Kramer FR (2012). Molecular beacons in diagnostics. *F1000 Medicine Reports* **4**

2-33. Ricci F, Plaxco KW (2008). E-DNA: a convenient, label-free method for the electrochemical detection of hybridization. *Microchim Acta* **163**:149-155

2-34. Smith SB, Cui Y, Bustamante C (1996). Overstretching B-DNA: The elastic response of individual double-stranded and single-stranded DNA molecules. *Science* **271**: 795-799

2.8 Funding and acknowledgements

We thank F. W. Dahlquist for helpful discussions. This work was supported by the NIH AI107.936, NSF DMR-1121053, by NSERC RGPIN-2014-06403 (A.V.-B.), ERC (project no. 336493; F.R.), by the Marie Curie IOF Pr 298491 under FP7-PEOPLE-2011-IOF (F.R.), PIRE-ECCI (A.J.S.), and by the Institute for Collaborative Biotechnologies through grant W911NF-09-0001 from the U.S. Army Research Office. The content of the information does not necessarily reflect the position or the policy of the Government, and no official endorsement should be inferred.

3. INTRINSIC DISORDER AS A GENERALIZABLE STRATEGY FOR THE RATIONAL DESIGN OF HIGHLY RESPONSIVE, ALLOSTERICALLY COOPERATIVE RECEPTORS

Control over the sensitivity with which biomolecular receptors respond to small changes in the concentration of their target ligand is critical for the proper function of many cellular processes. Such control could likewise be of utility in artificial biotechnologies, such as biosensors, genetic logic gates, and "smart" materials, in which highly responsive behavior is of value. In nature, the control of molecular responsiveness is often achieved using "Hill-type" cooperativity, a mechanism in which sequential binding events on a multivalent receptor are coupled such that the first enhances the affinity of the next, producing a steep, higher-order dependence on target concentration. Here we use an intrinsic-disorder-based mechanism that can be implemented without requiring detailed structural knowledge to rationally introduce this potentially useful property into several normally non-cooperative biomolecules. To do so we fabricate a tandem repeat of the receptor that is destabilized (unfolded) via the introduction of a long, unstructured loop. The first binding event requires the energetically unfavorable closing of this loop, reducing its affinity relative to that of the second binding event, which, in contrast occurs at a preformed site. Using this approach we have rationally introduced cooperativity into three unrelated aptamers, achieving in the best of these a Hill coefficient experimentally indistinguishable from the theoretically expected maximum. The extent of cooperativity, and thus the steepness of the binding transition, are,

moreover, well modeled as simple functions of the energetic cost of binding-induced folding, illustrating the quantitative nature of this design strategy. This work was published in 2014 in *Proceedings of the National Academy of Sciences USA* (3-1).

3.1 Motivation

Optimized shape and mid-point of binding curves is critical to the function of many cellular processes (3-2). One of the most commonly-evolved strategies for the control of the behavior of receptors is allostery, in which the binding of one ligand alters the affinity with which subsequent ligands bind. Allostery comes in two "flavors." *Hetero*tropic allostery, in which the two ligands *differ*, provides a means of shifting the mid-point of a binding curve to higher or lower target concentrations without changing the curve's intrinsically hyperbolic shape and thus without altering its sensitivity to small changes in the relative concentration of its molecular target (*Figure 3-1, left*). An example is the binding of bisphosphoglycerate to mammalian hemoglobin, which decreases the protein's affinity for oxygen, thus pushing its binding curve to higher concentrations and enhancing oxygen transport efficiency, whilst leaving the intrinsic shape of its binding curve unaltered. *Homo*tropic allostery, in contrast, occurs when the ligands are the *same*; that is, when the binding of one copy of a ligand changes the affinity with which subsequent copies of the same molecule bind. This mechanism, commonly referred to as "cooperativity," changes not only the placement but also the *shape* of the binding curve, producing either a more responsive, higher-order dependence on ligand concentration (positive cooperativity) or a less responsive, lower-order dependence (negative cooperativity) (*Figure 3-1, right*). Like heterotropic allostery,

cooperativity is also seen in the function of hemoglobin; the protein uses this mechanism to bind four oxygen molecules in a positively cooperative, approximately "all-or-nothing" fashion, steepening its binding curve and enhancing its ability to deliver oxygen over the rather modest concentration gradient present between the lungs and the peripheral tissues.

The ubiquity with which nature exploits homotropic and heterotropic allostery has motivated efforts to rationally engineer these mechanisms into biomolecular receptors normally lacking them, both to test our understanding of the principles underlying these effects and to harness them to improve the utility of artificial biotechnologies. The rational introduction of heterotropic allostery into otherwise non-allosteric receptors, for example, has seen significant prior exploration [e.g., (3-3, 3-4, 3-5, 3-6, 3-7, 3-8, 3-9)], using both mechanical coupling [e.g., (3-3, 3-6, 3-7, 3-8, 3-9)] and mutually-exclusive folding [e.g., (3-4, 3-5)] approaches to successfully introduce this mechanism into a range of protein- and nucleic acid-based receptors. The design of allosterically cooperative receptors, in contrast, has seen far less success. That is, while a handful of specific examples of rationally designed cooperativity have been reported to date (3-10, 3-11, 3-12, 3-13), no general approach has previously been reported by which such behavior can be rationally introduced into any arbitrarily complex biomolecule. This failure has limited the extent to which cooperativity, which could provide a powerful means of improving the ability of artificial biotechnologies to respond to small changes in molecular concentration (3-10, 3-14), can be applied in applications such as biosensing (3-15, 3-16), "smart" drug delivery materials (3-17, 3-18), and molecular (3-19) and genetic (3-20) logic gates, in which such enhanced responsiveness would be of value.

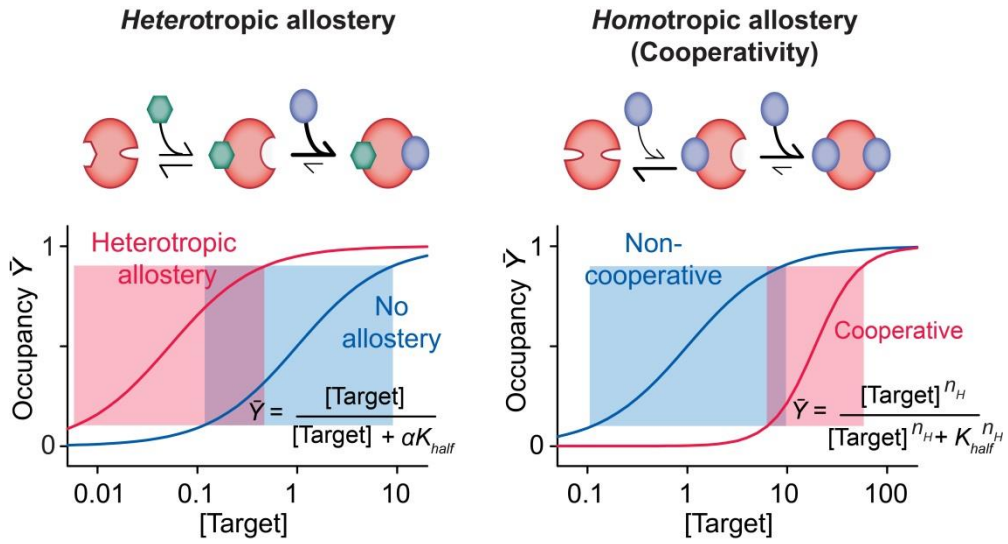

Figure 3-1. Allostery is a common strategy for the tuning of the shape and position of ligand-response curves. (***Left***) In heterotropic allostery, the binding of one ligand to a receptor increases or decreases the affinity with which a second, different ligand binds, shifting the placement of the binding curve without altering its shape and thus without altering the width of its useful dynamic range (shaded boxes) or, in turn, its sensitivity to small changes in target concentration. (***Right***) In homotropic allostery, in contrast, the binding of one copy of target ligand changes the affinity with which additional copies of the same ligand bind, altering both the placement and the shape of the binding curve. The latter effect allows the system to respond more (positive cooperativity) or less (negative cooperativity) sensitively to changes in target ligand concentration. For positive cooperativity receptor occupancy is a higher (than unity) order function of target concentration, with the exponent, n_H, being known as the Hill coefficient.

Two reasons account for why, despite its underlying simplicity and elegance, achieving the rational design of positive cooperativity has proven far from straightforward. First, to achieve the effect requires the creation of systems in which a higher affinity site is occupied only after a lower affinity homotypic site is already filled (which would normally be filled only at higher ligand concentrations). This contrasts sharply with heterotropic allostery, in which the two binding sites typically exhibit little if any cross-reactivity. Second, all of the binding sites of a cooperative receptor recognize copies of the same ligand, rendering it more difficult to alter the affinity of one independently of that of the others. This

is again in contrast to heterotropic allostery, in which each binding site is chemically distinct, allowing each to be independently optimized. Given these difficulties, and given the relative infancy of biomolecular design efforts (3-21, 3-22, 3-23), the ability to perform the structure-based design of cooperativity appears to be beyond current capabilities except for the simplest, most well understood receptors (3-10, 3-11, 3-12, 3-13). Here, however, we employ an approach to the rational engineering of allosterically cooperative receptors that does not require detailed, structure-based design. Indeed, our approach is so simple that it can be performed, as demonstrated here, even in the absence of detailed knowledge of the parent receptor's structure.

3.2 Intrinsic disorder and allostery in Biology

Our design approach is inspired by intrinsically disordered proteins, proteins that are normally unfolded and only fold upon binding their target ligand. Specifically, both theoretical (3-24) and experimental (3-25, 3-26) studies have demonstrated that the global conformation change these proteins undergo upon an initial ligand binding event provides a convenient means of pre-organizing a second, distal ligand binding site. This improves the affinity of the second binding event (since binding need no longer pay the unfavorable cost associated with folding), leading to positive allosteric behavior. Ferreon et al., for example, have shown that the intrinsically disordered oncoprotein adenovirus early region 1A (E1A) folds upon binding either of its two (different) target ligands (CREB binding protein or retinoblastoma protein), thus increasing the affinity with which the second ligand binds and rendering the system heterotropically allosteric (3-25). And Standly and co-workers have

shown that the partially intrinsically disordered protein STIM 1 exhibits strongly homotropic allosteric binding to calcium (3-26). Here we use this same mechanism to rationally introduce cooperativity into a number of normally non-cooperative aptamers (DNA-based receptors often adopting complex tertiary folds), thus producing steeper, more responsive binding curves than those seen for the unmodified parent molecule.

Positive cooperativity arises when the first binding event on a multisite receptor improves the binding affinity of additional copies of the same ligand. Thus, once one copy of the ligand is bound the probability of the second binding event becomes high, generating effectively "all or none" behavior. The resulting binding curve (3-27) is given by the Hill equation:

$$Receptor\ site\ occupancy\ \bar{Y} = \frac{(target)^{n_H}}{(target)^{n_H} + \left(K_{1/2}\right)^{n_H}} \qquad \textbf{(3-1)}$$

in which $K_{1/2}$ is the ligand concentration at which half of the receptor sites are bound, and n_H, the Hill coefficient, describes the order of the dependence on ligand concentration (Fig. 3-1, *lower right*). For a non-cooperative receptor, in which each copy of the ligand binds independently of all others, $n_H = 1$. For an ideally cooperative receptor, in which all of the binding sites on any one receptor molecule are simultaneously either fully occupied or fully unoccupied, the Hill equation equals the number of binding sites. The Hill coefficient is, in turn, related to the useful dynamic range of a receptor (a convenient measure of responsiveness that is typically defined as the ratio between the target concentration at which occupancy is 90% to that at which it is 10%; $C_{90\%}$ and $C_{10\%}$, respectively) by (3-28):

$$Dynamic\ range = \frac{C_{90\%}}{C_{10\%}} = 81^{1/n_H} \qquad \textbf{(3-2)}$$

From this we see that the useful dynamic range of a non-cooperative receptor (n_H = 1) is quite broad; such a receptor requires an 81-fold change in target concentration to transition from 10% occupancy to 90% occupancy, rendering it relatively insensitive to small changes in this input. The dynamic range falls to just 9-fold, however, for an ideally cooperative, two-site receptor (n_H = 2), rendering such a receptor many times more sensitive to small changes in target concentration.

In naturally-occurring receptors the energetic difference between the first and subsequent binding events required to generate allosteric cooperativity usually arises due to mechanical coupling between the relevant binding sites. That is, structural changes that occur upon the first binding event are transduced throughout the receptor in a manner that improves affinity at other, distal, sites. In hemoglobin, for example, this occurs when the protein undergoes a global conformational switch from a low affinity state that dominates when no ligand is bound, to a higher affinity conformation upon the binding of the first oxygen molecule (3-29). Here we hypothesize that the requisite global conformational switch can also be driven by a mechanism analogous to the binding-induced folding seen for intrinsically disordered proteins. That is, via a binding-induced switch from a largely or entirely disordered state lacking pre-configured binding sites to a well-defined folded conformation exposing multiple, well-structured binding sites (*Figure 3-2*, *Top*). In this scenario the affinity of a binding site is reduced when its neighboring site is empty because the receptor is unfolded and thus binding must pay the cost associated with folding it. Equivalently, the affinity of a binding site is enhanced when its neighboring site is already occupied. The relative [microscopic –see (3-28, 3-29)] dissociation constants of the two binding scenarios (neighboring site open, K_{D1}, and neighboring site occupied, K_{D2}) are then

related to K_S, the equilibrium constant for forming the folded conformation in the absence of the target ligand, by (3-13):

$$\frac{K_{D2}}{K_{D1}} = \frac{K_S}{1+K_S} \quad \textbf{(3-3)}$$

The Hill coefficient, in turn, is related to this ratio by (3-12, 3-27):

$$n_H = \frac{2}{1+\sqrt{\frac{K_{D2}}{K_{D1}}}} = \frac{2}{1+\sqrt{\frac{K_S}{1+K_S}}} \quad \textbf{(3-4)}$$

From this we see that a folding equilibrium constant of just 0.1, which corresponds to a folded state that is unstable in the absence of the target ligand by just 6 kJ/mol (at room temperature), is sufficient to achieve n_H = 1.5. This, in turn, narrows the receptor's dynamic range by more than a factor of four (Eq. 3-2), significantly enhancing its sensitivity to small changes in the concentration of its target ligand (*Figure 3-2*, *bottom*).

3.3 Design approaches

To physically realize such folding-based cooperativity, we have re-engineered several normally non-cooperative receptors into constructs comprised of a tandem repeat of one half of the receptor connected to a tandem repeat of the second half of the same receptor via an unstructured linker (*Figure 3-2*, *top*). In the absence of target, the unfavorable entropic cost of closing this linker (i.e., of ordering this disordered region) *de*stabilizes the folded, binding-competent conformation, producing a largely unfolded state lacking structured binding sites. The binding of the first copy of the target ligand brings the two halves of the construct into apposition, forming *both* binding sites. The second binding event thus need not pay the

unfavorable free energy cost associated with folding, improving its affinity and, in turn, producing a cooperative response.

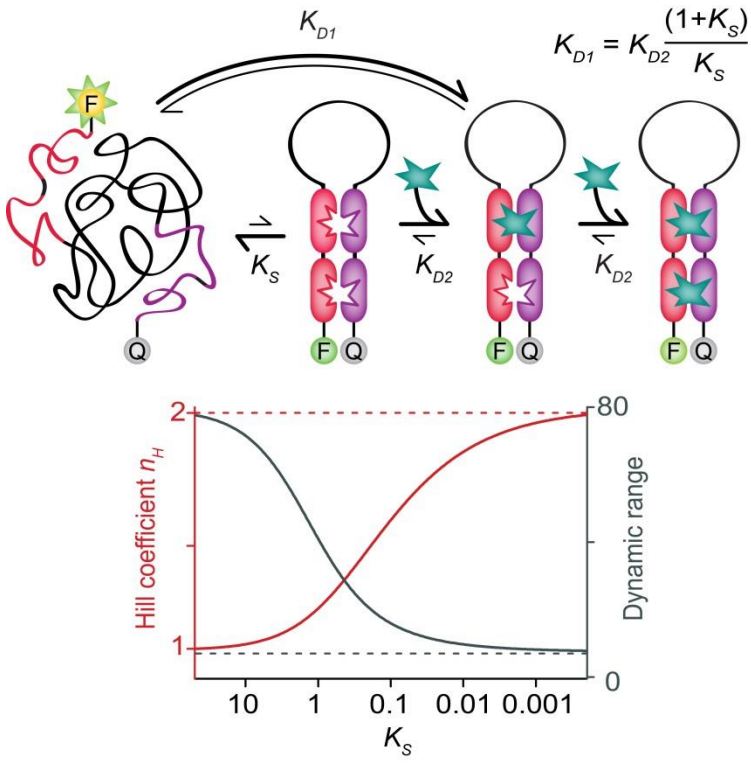

Figure 3-2. Our approach to the rational design of cooperativity employs receptor architectures that fold upon binding the first target molecule. (***Top***) Specifically, our receptor architectures consists of two copies of one half of a receptor (red), a variable length, unstructured linker (black), and two copies of the second half of the receptor (purple). In the absence of target ligand, the construct exists primarily in a disordered state lacking pre-formed binding sites. This disordered state, however, is in equilibrium (equilibrium constant, K_S) with the fully-folded receptor The first target molecule to bind must overcome the unfavorable free energy associated with forming this structure, reducing its affinity compared to that of the pre-formed aptamer by the factor $(1+K_S)/K_S$. The second target molecule binds to pre-formed binding site, thus improving its affinity relative to that of the first binding event. (***Bottom***) The degree of cooperativity, i.e., the Hill coefficient (n_H) and the useful dynamic range (typically defined as the ratio between the target concentration at which occupancy is 90% to that at which it is 10), depend strongly on K_S. So much so that an equilibrium constant as great as ~0.1 (i.e., receptors that populate their high affinity state to the level of ~10% even in the absence of ligand) still produces near-maximum sensitivity to small changes in the concentration of the target ligand.

3.4 Results

We employed as our recognition sites a simple, mercury(II)-binding thymine-thymine mismatch (3-30) for the preliminary exploration of our design approach. Specifically, we inserted two thymine-thymine mismatches into an otherwise complementary DNA stem, the two strands of which are linked via an unstructured poly-AC loop, and the two termini of which are modified with a fluorophore-quencher pair that reports on folding (*Figure 3-3*, *left*). Employing a loop length of 50 bases, this construct is reasonably cooperative, achieving a Hill coefficient of 1.51±0.03 and a useful dynamic range of just 18(±1)-fold (*Figure 3-3*, *middle*). This represents a substantial increase in responsiveness relative to that of the

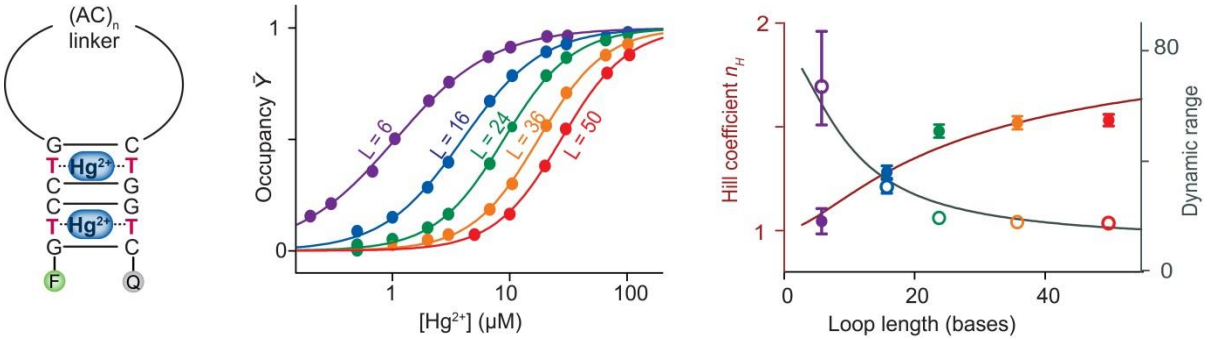

Figure 3-3. Our first test-bed system is a cooperative mercury(II)-binding receptor. (***Left***) Our first test-bed system consists of a short, double-stranded stem containing two mercury(II)-binding thymine-thymine mismatches linked via a variable length, unstructured, poly-AC sequence. (***Middle***) The cooperativity and binding affinity of these constructs scales monotonically with the loop length, ranging from a Hill coefficient of 1.51±0.03 (dynamic range = 18-fold) for the construct with a 50-base loop to a Hill coefficient of 1.05±0.05 (dynamic range = 67-fold) for the construct with a 6-base loop, with the latter being quite close to the behavior observed for single-site binding (*Figure 3-4*). **(*Right*)** Speaking to the quantitative nature of this design, the observed Hill coefficients and dynamic ranges fit equations 7 and 2 with R^2 of 0.920 and 0.956, respectively, using only a single fitted parameter (K_{close}), the best fit-value of which is within experimental uncertainty of independent estimates (see text). Of note, all of these constructs equilibrate within the 30 to 60 s mixing dead time of our experiments (*Figure 3-5*).

equivalent, 50-base-linker receptor in which one of the two thymine-thymine mismatch sites has been replaced with a non-binding cytosine-cytosine mismatch; as expected, this single-site construct exhibits a Hill coefficient within experimental uncertainty of unity and a dynamic range within uncertainty of 81-fold (*Figure 3-4*).

The degree of cooperativity depends on the equilibrium constant for switching the receptor from its low affinity state to its high affinity state (Eq. 3-4). In our design this equilibrium constant is the product of the equilibrium constant for forming the intact binding sites in the absence of the linker, K_{close}, and the unfavorable equilibrium constant associated with closing the linker, K_{link}:

$$K_S = K_{link}K_{close} \quad \textbf{(3-5)}$$

Consistent with this, the cooperativity of our two-site mercury receptor falls monotonically as we shorten its loop (thus decreasing K_{link}) from 50 bases (n_H = 1.51±0.03) to 6 bases (n_H = 1.05±0.05) (*Figure 3-3*, *middle*). To put these observations on a still more quantitative footing we note that, for linkers longer than the ~3-base persistence length of single-stranded DNA (30), K_{link} is dominated by the entropic cost of loop closure and thus should go as

$$K_{link} = L^{-1.75} \quad \textbf{(3-6)}$$

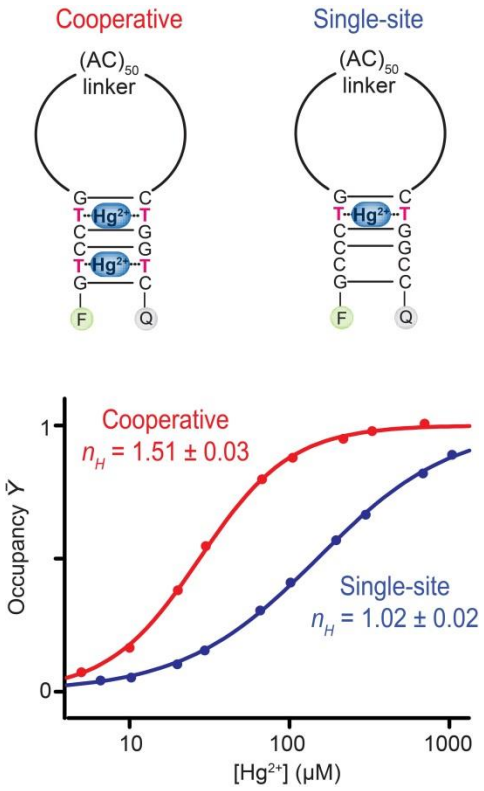

Figure 3-4. A single-site Hg(II)-binding control beacon binds Hg(II) non-cooperatively, with a Hill coefficient within error of unity.

where L is linker length (3-32). Combining equations 4, 5 and 6 we can thus relate the degree of cooperativity of our constructs to the length of their unstructured loops:

$$n_H = \frac{2}{1+\sqrt{\frac{K_{close}L^{-1.75}}{1+K_{close}L^{-1.75}}}} \quad \textbf{(7)}$$

Despite employing only a single floating parameter, K_{close}, this equation fits the observed Hill coefficients of our family of cooperative mercury receptors quite well (R^2 = 0.92), speaking to the validity of our design model (*Figure 3-3*, *right*). Moreover, the fitted value of K_{close}, 59±30, corresponds to a free energy of -10.6(±1.4) kJ/mol for the formation of the two-mismatch-containing stem. This, in turn, agrees to within experimental uncertainty with the

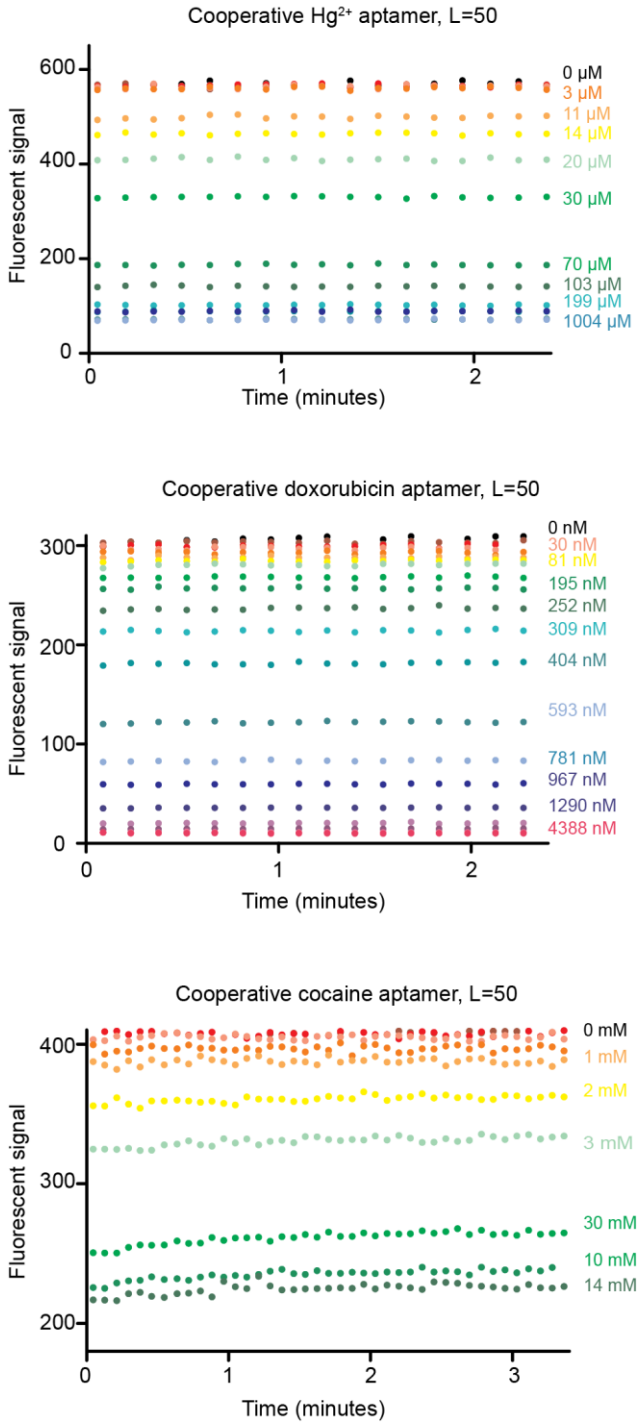

Figure 3-5. To ensure that all titration points are collected after the sample has reached equilibrium, the signal over time is measured for all collection points. All samples equilibrate within the 30-60 second dead time of mixing for the instrument.

~12.2(±1.6) kJ/mol predicted by adding the -4.6 kJ/mol stability of the stem as predicted by the "DINAMelt Mfold" secondary structure prediction algorithm (3-33, 33-34) to the -7.6(±1.6) kJ/mol prior literature estimates of the stabilization produced by the fluorophore-quencher pair we have employed (3-35, 3-36).

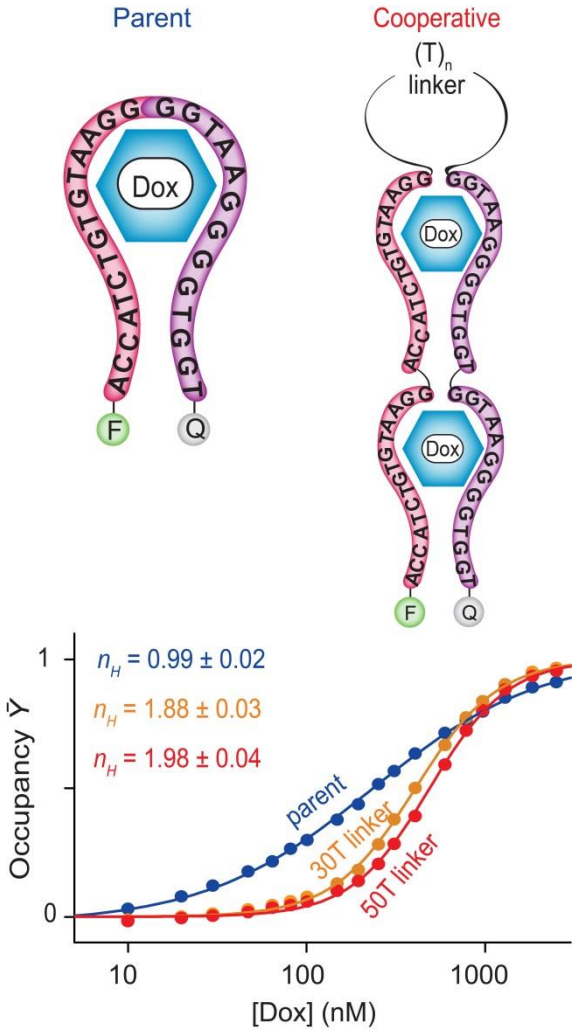

Figure 3-6. (***Top***) We have also applied our approach to engineer cooperativity into a doxorubicin-binding aptamer, which, while predicted to form a stem loop, is ultimately of unknown structure. (***Bottom***) Constructs employing either 30- or 50-base linkers achieve Hill coefficients of 1.88±0.03 and 1.98±0.04, respectively, corresponding to useful dynamic ranges of 10.4-fold and 9.2-fold. The Hill coefficient of the parent aptamer, in contrast, is within experimental uncertainty of unity.

Encouraged by these successful test-case design efforts, we next adapted our simple strategy to engineer cooperativity into two structurally more complex receptors. For the first, we employed the doxorubicin-binding aptamer of Wochner et al., which binds this important cancer chemotherapeutic with a dissociation constant of ~200 nM (3-37). Of note, the three-dimensional structure of this aptamer is not known, rendering this a significantly more challenging test of our design approach. To introduce cooperativity into the doxorubicin-binding aptamer we first employed DINAMelt Mfold as a guide to predict its likely secondary structure (*Figure 3-6*, *top*). We then "cut" the parent aptamer sequence at the position within the single putative loop identified by Mfold and linked tandem repeats of the two resulting half-aptamers via unstructured poly-thymine sequences of either 30 or 50 bases. The construct employing a 50-base linker is quite cooperative, exhibiting a Hill coefficient of 1.98±0.04 and a dynamic range of just 9.2(±0.4)-fold (*Figure 3-6*, *bottom*), values within experimental uncertainty of ideal behavior for a fully cooperative, two-site receptor. The construct employing the shorter, 30-base linker is slightly less cooperative, achieving a Hill coefficient of 1.88±0.03 and a useful dynamic range of 10.4(±0.8)-fold. The parent, single-site doxorubicin aptamer, in contrast, achieves a Hill coefficient of 0.99±0.02 and a useful dynamic range of 81(±3)-fold. These values are well within the predictions of our model.

The quantitative model for folding-based cooperativity outlined above (Eq. 3-7) for our mercury receptors likewise describes the behavior of our doxorubicin-binding constructs. Specifically, Mfold (3-33, 3- 34) predicts that the parent aptamer forms a stem loop structure with folding free energy that is unstable by 0.75 kJ/mol (per monomeric aptamer) in the absence of doxorubicin. When added to the favorable association energy of the fluophore-

quencher pair (3-35, 3-36) this yields a closing free energy of -6.1 kJ/mol and a K_{close} of 11.2 for the tandem repeat. Inserting the latter value into Eq. 3-7 predicts Hill coefficients of 1.71 and 1.80 for our 30-thymine and 50-thymine constructs, respectively, estimates that are reasonably close to the experimental values.

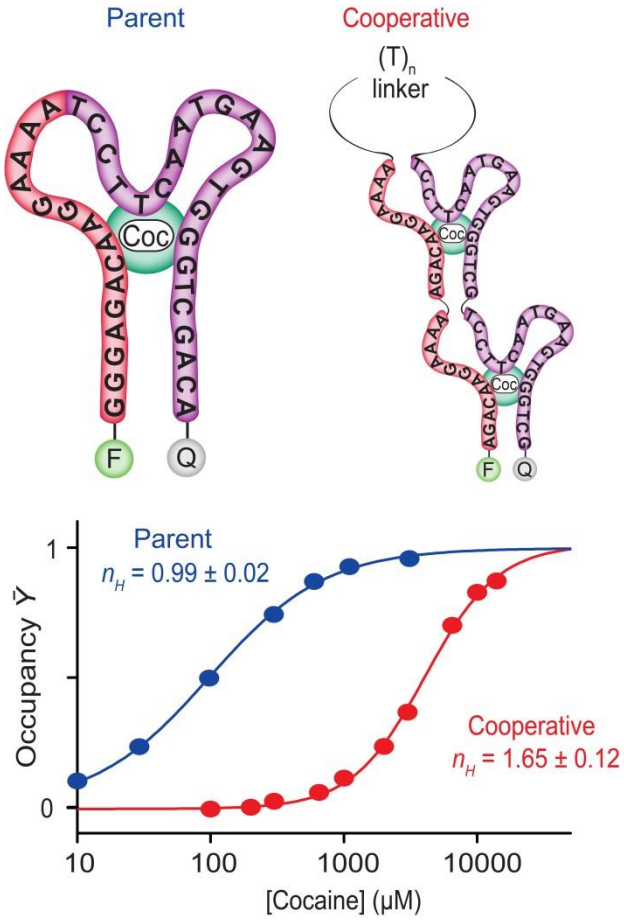

Figure 3-7. As a final test of the generality of our approach we have applied it to the cocaine-binding aptamer of Stojanovic *et al.* (3-38). (***Top***) This aptamer is thought to form a three-way junction. ***(Bottom)*** The modified aptamer achieves substantial cooperativity, exhibiting a Hill coefficient of 1.65±0.12. The parent aptamer, in contrast, exhibits a Hill coefficient within experimental uncertainty of unity.

As a final test of the generality of our approach we applied our method to the cocaine-binding aptamer described by Stojanovic *et al.* (3-38). This is another receptor for which detailed conformational infromation is lacking. Using a previously identified cut site (3-39), we engineered a cooperative receptor in which tandem repeats of the two halves of the aptamer are linked via an unstructured, 50-base poly-thymine sequence (*Figure 5*, *top*). The resultant construct exhibits a Hill coefficient of 1.65±0.12 and dynamic range of binding of 13(±4)-fold (*Figure 5*, *bottom*). As with the cooperative mercury(II)- and doxorubicin-binding aptamers, the behavior of the cooperative cocaine-binding aptamer likewise appears consistent with Eq. 7. Complicating this analysis, however, is the fact that the aptamer is thought to contain a large number of non-Watson-Crick base pairs (3-39), and thus DINAMelt Mfold likely fails to accurately model its folding free energy. To overcome this, we instead used the experimentally determined folding free energy of the parent aptamer (3-40) to determine K_{close}. Specifically, the folding free energy of the fluorophore-and-quencher-modified parent aptamer is -7.5 kJ/mol. Given the known stabilizing effects of the fluorophore-quencher pair (3-35, 3-36), we thus estimate that the folding free energy of the dye-free parent aptamer is +0.1 kJ/mol. The folding free energy of a dimer aptamers, one of which is dye-labeled, should thus be -7.4 kJ/mol, which in turn corresponds to a K_{close} of 19. Inserting this value into equation 3-7 predicts a Hill coefficient of 1.75, which is again within experimental uncertainty of the observed value.

3.5 Conclusions

Here we have demonstrated the utility of employing binding-induced folding as an effective, quantitative and potentially versatile means of engineering allosteric cooperativity

into normally non-cooperative biomolecular receptors. Specifically, we have used this approach to generate cooperative receptors starting from three distinct, unrelated aptamers that bind three distinct and unrelated molecular targets. The most cooperative of these re-

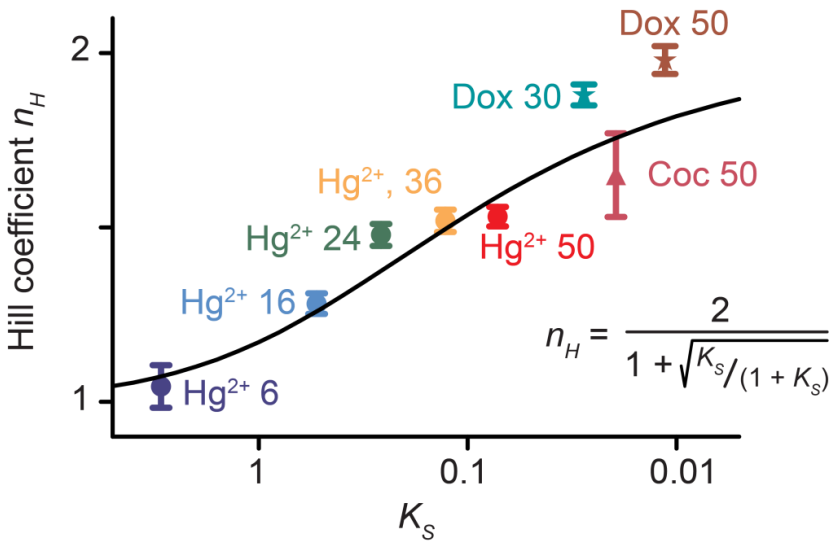

Figure 3-8. We have achieved the rational, quantitative introduction of cooperativity into a range of aptamer-based receptors. As shown here, for example, equation 4 (solid line), which defines the expected relationship between K_s, the equilibrium constant for receptor "folding," and n_H, the Hill coefficient, describes the behavior of all eight of the receptors reported in this paper with reasonable accuracy despite its lacking *any* fitted parameters. The biomolecules shown include receptors designed to cooperatively bind mercury ions (Hg^{2+}), doxorubicin (Dox), and cocaine (Coc), and featuring, as denoted in the figure, unstructured loops of between 6 and 50 bases.

designed receptors exhibits a Hill coefficient within experimental uncertainty of the theoretically expected maximum, thus converting the 81-fold dynamic range associated with single-site binding to a 9-fold dynamic range and rendering the resultant receptor far more sensitive than its parent to small changes in the concentration of its target ligand. Finally, the approach is quantitative, with the degree of cooperativity attained for each of eight different

receptors (again, binding three quite different molecular targets) closely matching the values expected given the switching equilibrium constant, K_S, of each of the modified aptamers (*Figure 3-8*).

The ability to rationally engineer biomolecular receptors such that they overcome the "tyranny of the Langmuir isotherm (3-41)" and respond robustly to relatively small changes in the concentration of their target ligand has proven an important goal in molecular engineering and synthetic biology (3-15, 3-16, 3-17, 3-18, 3-19, 3-20). While nature frequently exhibits the simple, elegant mechanism of allosteric cooperativity to overcome this limitation, the generalizable ability to recapitulate this behavior in normally non-cooperative biomolecular receptors has hitherto remained elusive, with successful examples of artificially engineered, allosteric cooperativity having been restricted to a small number of more-or-less non-generalizable examples (3-10, 3-11, 3-12, 3-13). In part this is because our ability to rationally design biomolecules that switch reversibly between two well-defined conformations likewise remains limited (3-23). In response we have demonstrated here a means of engineering cooperativity that circumvents this challenge by utilizing the (easily achievable) unfolded state as one of the two required conformations. Given the ease with which single domain proteins can similarly be re-engineered to undergo binding-induced folding (see, e.g., (3-42, 3-43)), and the recent report of a naturally occurring protein that employs intrinsic disorder to generate cooperative binding (3-26), we suspect that intrinsic disorder may also prove a useful means of rationally optimizing the responsiveness of protein-based receptors.

3.6 Materials and Methods

All reagent-grade chemicals, including cocaine, mercury chloride, doxorubicin, sodium phosphate monobasic and, sodium phosphate dibasic (doxorubicin from LC Laboratories, Woburn, Massachusetts; all others from Sigma-Aldrich, St. Louis, Missouri) were used as received. DNA molecules modified with a carboxyfluorescein (FAM) and a black-hole-quencher-1 (BHQ) were used as purchased (BioSearch Tech, Novato, CA). The sequences are as follows:

Cooperative Hg(II)-binding aptamer:

5' (FAM)-GTCCTG-$(AC)_n$-CTGGTC-(BHQ), n = 3, 8, 12, 18, 25

Single-site Hg(II)-binding aptamer:

5' (FAM)-GCCCTG-$(AC)_{25}$-CTGGCC-(BHQ)

Cooperative doxorubicin-binding aptamer:

5' (FAM)-$(ACCATCTGTGTAAGG)_2$-T_n-$(GGTAAGGGGTGGT)_2$-(BHQ), n = 30, 50

Single-site doxorubicin-binding aptamer:

5' (FAM)-ACCATCTGTGTAAGGGGTAAGGGGTGGT-(BHQ)

Cooperative cocaine-binding aptamer:

5’ (FAM)-AGACAAGGAAAATTTAGACAAGGAAAA-T_{50}-

TCCTTCAATGAAGTGGGTCGTTTCCTTCAATGAAGTGGGTCG-(BHQ)

Single-site cocaine-binding aptamer:

5' (FAM)-GGGAGACAAGGAAAATCCTTCAATGAAGTGGGTCGACA-(BHQ)

We obtained all fluorescence measurements using a Cary Eclipse Fluorimeter (Varian) with excitation at 485 (± 5) nm and acquisition at 515 (± 10) nm. We measured the mercury-binding and doxorubicin-binding receptors at 30˚C and the cocaine-binding receptors at 37˚C in 50 mM sodium phosphate buffer pH 7. We obtained binding curves by adding sequentially increasing target concentrations to a stock solution of the receptors at 20 nM. For the Hg^{2+}- and doxorubicin-binding receptors we titrated in solutions containing the target molecule but lacking the aptamer; we then adjusted the observed signal to account for the resultant dilution of the aptamer. For the cocaine-binding aptamer we titrated in a solution of cocaine also containing the aptamer at 20 nM, thus keeping the aptamer concentration constant throughout the experiments. We thermally equilibrated all samples for at least 15 minutes prior to taking the first measurement. To ensure that the binding equilibrium had been reached prior to measurement we obtained kinetic traces after the addition of each new target concentration (e.g., *Figure 3-5*). The data employed in the equilibrium plots (*Figures 3-3, 3-4* and 3-*7*) represent the average of 10 fluorescence measurements collected at least 2 minutes after these additions. Hill coefficients were determined by fitting these data using GraphPad Prism plotting software. Error bars represent 95% confidence intervals based on standard errors derived from these fits.

3.7 References

3-1. Simon AJ, Vallée-Bélisle A, Ricci F, Watkins HM, Plaxco KW (2014). Intrinsic disorder as a generalizable strategy for the rational design of highly responsive, allosterically cooperative receptors. *Proc Natl Acad Sci USA* **111**:15048–15053

3-2 Zhang Q, Bhattacharya S, Andersen ME (2013) Ultrasensitive response motifs: basic amplifiers in molecular signaling networks. *Open Biol* **3**:130031

3-3. Strickland D, Moffat K, Sosnick TR (2008) Light-activated DNA binding in a designed allosteric protein. *Proc Natl Acad Sci USA* **105**:10709-10714

3-4. Radley TL, Markowska AI, Bettinger BT, Ha JH, Loh SN (2003) Allosteric switching by mutually exclusive folding of protein domains. *J Mol Biol* **332**:529-536

3-5. Guntas G, Ostermeier M (2004). Creation of an allosteric enzyme by domain insertion. *J Mol Bio* **336**:263-273

3-6. Choi B, Zocchi G, Canale S, Wu Y, Chan S, Perry L (2005). Artificial allosteric control of Maltose Binding Protein. *Phys Rev Lett* **94**:038103

3-7. Tang J, Breaker RR (1997). Rational design of allosteric ribozymes. *Chem Biochem* **4**:453-459

3-8. Ricci F, Vallée-Bélisle A, Porchetta A, Plaxco KW (2012). Rational design of allosteric inhibitors and activators using the population-shift model: in vitro validation and application to an artificial biosensor. *J Am Chem Soc* **134**:15177-15180

3-9. Porchetta A, Vallée-Bélisle A, Plaxco KW, Ricci F (2012). Using distal-site mutations and allosteric inhibition to tune, extend, and narrow the useful dynamic range of aptamer-based sensors. *J Am Chem Soc* **134**:20601-20604

3-10. Dueber JE, Mirsky EA, Lim WA (2007). Engineering synthetic signaling proteins with ultrasensitive input/output control. *Nat Biotech* **25**:660-662

3-11. Kwok CK, Sherlock ME, Bevilacqua PC (2013). Decrease in RNA folding cooperativity by deliberate population of intermediates in RNA G-quadruplexes. *Angew Chem* **52**:683-686

3-12. Wang Z, Lee JH, Lu Y (2008). Highly sensitive "turn-on" fluorescent sensor for Hg2+ in aqueous solution based on structure-switching DNA. *Chem Commun* **45**:6005-6007

3-13. Simon AJ, Vallée-Bélisle A, Ricci F, Watkins H, Plaxco KW (2014). Using the population-shift mechanism to rationally introduce Hill-type cooperativity into a biomolecular receptor. *Angew Chem* **53**:9471-9475

3-14. Whitty A (2008). Cooperativity and biological complexity. *Nat Chem Biol* **4**:435-439

3-15. Katz E, Wang J, Privman M, Halámek J (2012). Multianalyte digital enzyme biosensors with built-in boolean logic. *Anal Chem* **84**:5463-5469

3-16. Ricci F, Vallée-Bélisle A, Plaxco KW (2011). High-precision, in vitro validation of the sequestration mechanism for generating ultrasensitive dose-response curves in regulatory networks. *PLoS Comput Biol* **7**:e1002171

3-17. MacEwan SR, Chilkoti A (2012). Digital switching of local arginine density in a genetically encoded self-assembled polypeptide nanoparticle controls cellular uptake. *Nano Lett* **12**:3322-3328

3-18. von Maltzahn G, Park J-H, Lin K, Singh N, Schwöppe C, Mesters R, Berdel WE, Ruoslahti E, Sailor MJ, Bhatia SN (2011). Nanoparticles that communicate in vivo to amplify tumour targeting. *Nat Mater* **10**:545-552

3-19. Chuang M-C, Windmiller JR, Santhosh P, Valdés-Ramírez G, Katz E, Wang J (2011). High-fidelity determination of security threats via a Boolean biocatalytic cascade. *Chem Commun* **47**: 3087-3089

3-20. Bonnet K, Yin P, Ortiz ME, Subsoontorn P, Endy D (2013). Amplifying genetic logic gates. *Science* **340**:599-603

3-21. Nanda V, Koder RL (2010). Designing artificial enzymes by intuition and computation. *Nat Chem* **2**:15-24

3-22. Samish I, MacDermaid CM, Perez-Aguilar JM, Savern JG (2011). Theoretical and computational protein design. *Annu Rev Phys Chem* **62**:129-149

3-23. Fleishman SJ, Baker D (2012). Role of the biomolecular energy gap in protein design, structure, and evolution. *Cell* **149**:262-273

3-24. Hilser VJ, Thompson EB (2007). Intrinsic disorder as a mechanism to optimize allosteric coupling in proteins. *Proc Natl Acad Sci* **104**:8311-8315

3-25. Ferreon AC, Ferreon JC, Wright PE, Deniz AA (2013). Modulation of allostery by protein intrinsic disorder. *Nature* **498**:390-394

3-26. Furukawa Y, Teraguchi S, Ikegami T, Dagliyan O, Jin L, Hall D, Dokholyan NV, Namba K, Akira S, Kurosaki T, Baba Y, Standley DM (2014). Intrinsic disorder mediates cooperative signal transduction in STIM1. *J Mol Biol* **426**:2082-2097

3-27. Hill AV (1910). The possible effects of the aggregation of the molecules of hæmoglobin on its dissociation curves. *J Physiol* **40**:IV–VII

3-28. Dahlquist FW (1978). The meaning of Scatchard and Hill plots. *Meth Enzymol* **48**:270-299

3-29. Ercolani G, Schiaffino L (2011). Allosteric, chelate, and interannular cooperativity: a mise au point. *Angew Chem* **50**:1762-1768

3-30. Miyake Y, Togashi H, Tashiro M, Yamaguchi H, Oda S, Kudo M, Tanaka Y, Kondo Y, Sawa R, Fujimoto T, Machinami T, Ono A (2006). MercuryII-mediated formation of thymine−HgII−thymine base pairs in DNA duplexes. *J Am Chem Soc* **128**:2172-2173

3-31. Paner TM, Amartunga M, Benight AS (1992). Studies of DNA dumbbells III. Theoretical analysis of optical melting curves of dumbbells with a 16 base-pair duplex stem and T_n end loops (n = 2, 3,4, 6, 8, 10, 14). *Biopolymers* **32**:881-892

3-32. Chan HS, Dill KA (1989). Intrachain loops in polymers. *J Chem Phys* **90**:492–509

3-33. SantaLucia JR (1998). A unified view of polymer, dumbbell, and oligonucleotide DNA nearest-neighbor thermodynamics. *Proc Natl Acad Sci USA* **95**:1460-1465

3-34. Zuker M (2003). Mfold web server for nucleic acid folding and hybridization prediction. *Nucl Acids Res* **31**:3406-3415

3-35. Vallée-Bélisle A, Ricci F, Plaxco KW (2009). Thermodynamic basis for the optimization of binding-induced biomolecular switches and structure-switching biosensors. *Proc Natl Acad Sci USA* **106**:13802-13807

3-36. Marras SAE, Kramer FR, Tyagi S (2007). Efficiencies of fluorescence resonance energy transfer and contact-mediated quenching in oligonucleotide probes. *Nucl Acids Res* **30**:e122

3-37. Wochner A, Menger M, Orgel D, Cech B, Rimmele M, Erdmann VA, Glökler J (2008). A DNA aptamer with high affinity and specificity for therapeutic anthracyclines. *Anal Biochem* **373**:34-42

3-38. Stojanovic MN, de Prada P, Landry DW (2001). Aptamer-based folding fluorescent sensor for cocaine. *J Am Chem Soc* **123**:4928–4931

3-39. Zuo X, Xiao Y, Plaxco KW (2009). High specificity, electrochemical sandwich assays based on single aptamer sequences and suitable for the direct detection of small-molecule targets in blood and other complex matrices. *J Am Chem Soc* **131**:6944-6945

3-40. Lawrence C, Vallée-Bélisle A, Pfeil SH, de Mornay D, Lipman EA, Plaxco KW (2014). A comparison of the folding kinetics of a small, artificially selected DNA aptamer with those of equivalently simple naturally occurring proteins. *Protein Sci* **23**:56-66

3-41. Corn RM (2005). Enzymatically amplified SPR imaging for biosensor microarrays: Fighting the tyranny of the Langmuir isotherm. *Abstracts of Papers of the American Chemical Society* **230**:U330-U331

3-42. Ha J-H, Loh SN (2012). Protein conformational switches: From Nature to design. *Chemistry* **18**:7984-7999

3-43. Kohn JE, Plaxco KW (2005). Engineering of a signal-transduction mechanism for protein-based biosensors. *Proc Natl Acad Sci USA* **102**:10841-10845

3.8 Funding and acknowledgements

We thank F. W. Dahlquist for helpful discussions. We acknowledge support from the NIH (EB007689) and from the Institute for Collaborative Biotechnologies through grant W911NF-09-0001 from the U.S. Army Research Office. The content of the information does not necessarily reflect the position or the policy of the Government, and no official endorsement should be inferred.

4. QUANTITATIVE MEASUREMENT OF THE MOLECULAR- AND MICRON-SCALE DISSOLUTION KINETICS OF RESPONSIVE DNA HYDROGELS

Recent years have seen increasing reports of stimulus-responsive hydrogels constructed using DNA building blocks connected by responsive aptamer crosslinkers. To date, however, the majority of the literature describing these "smart" materials has been rather qualitative, presumably due to lack of simple, direct tools for measuring the thermodynamics and kinetics with which they respond. To meet this challenge, we demonstrate here simple, time-resolved methods by which the physical properties of these hydrogels can be measured over molecular and micron length scales. Specifically, we employ fluorophore-quencher labeled crosslinkers and the rheology of entrapped, micron-sized particles to simultaneously visualize dissolution at molecular and micron length-scales, respectively. Using these approaches we have measured the response kinetics of an adenosine-responsive DNA hydrogel as a function of effector concentration and the depth within the gel at which dissolution is being monitored. As expected, we find that the response timescale depends strongly and monotonically on both. We likewise find that dissolution is largely uniform at length scales longer than a few times the monomer-monomer distance, suggesting that the process may be significantly less cooperative than suggested. Finally, we find that bead mobility, which monitors micron-scale dissolution, exhibits a power-law-like relationship with the number of disrupted crosslinks before a distinct crossover from solid-like to liquid-like behavior, an observation that is in agreement with previous theoretical predictions. This chapter comprises a manuscript in preparation, to be submitted September 2015.

4.1 Motivation

Stimulus-responsive biological materials commonly use precisely organized biomolecular networks that assemble, dissolve, and rearrange in response to specific molecular or physical cues (4-1, 4-2, 4-3, 4-4, 4-5). To fabricate similarly responsive artificial materials, many researchers have turned to DNA as its simple, well-understood base-pairing rules easily support the design and construction of precisely organized three-dimensional networks (4-6, 4-7, 4-8, 4-9, 4-10, 4-11). Moreover, by incorporating aptamers, artificial DNA sequences selected for *in vitro* for their ability to bind specific molecular effectors, these hydrogels can be made responsive to the presence of specific atomic or molecular cues, such as pH (4-7), mercury (4-8), adenosine (4-8,4- 9), cocaine (4-9), lead (4-9), thrombin (4-10), and silver (4-11).

The simplicity with which responsive DNA hydrogels are designed and fabricated, and the potentially broad range of effectors to which they may respond, have led to significant exploration (e.g., 4-7, 4-8, 4-9, 4-10, 4-11). The majority of this literature, however, is rather qualitative, with little work having addressed, for example, the kinetics with which these hydrogels respond as functions of parameters such as the effector concentration, position within the hydrogel, or length scale over which dissolution is monitored. This lack of understanding regarding the quantitative aspects limits the development of rational strategies for the optimization of these hydrogels, including the rational "tuning" of such properties as their dissolution kinetics and the relationship between molecular and micron scale responses. For example, although there are numerous theoretical and simulation-based predictions regarding the interplay between molecular scale dissociation and micron-scale mechanics (4-12, 4-13, 4-14, 4-15, 4-16, 4-17, 4-18, 4-19, 4-

20, 4-21), experimental tests of these relationships are few (4-17, 4-18). In response, we demonstrate here methods for the quantitative characterization of the molecular- and micron-scale response kinetics of DNA hydrogels. Using these methods, we also test several previously predicted properties of such hydrogels, demonstrating the utility of our experimental approaches improving our understanding and, we believe, optimization of this important class of responsive materials.

4-2. Hydrogel measurement strategies

As our model system we employ an adenosine responsive version of the commonly employed Y-DNA hydrogel architecture. First described in 2009 by Cheng *et al.* (4-7), this architecture consists of a network of Y-shaped DNA "monomers" (each containing three annealed strands forming a double-stranded core with three pendant, single-stranded arms) crosslinked via hybridization with a complementary sequence to form a dense 3-dimensional network (*Figure 4-1*). For our studies we use the 27-base adenosine-binding aptamer of Huizenga and Szostak (4-22) as the crosslinker, rendering the resulting hydrogel responsive to this specific small molecule. Mixing the aptamer with the appropriate Y-monomers produces a thick, relatively rigid hydrogel (*Figure 4-1, right inset*). The introduction of adenosine stabilizes the aptamer's hairpin-shaped adenosine-binding conformation, dissociating it from the monomers and thus disrupting the hydrogel (*Figure 4-1, top*). Qualitatively, this dissolution can be observed by eye (Figure 4-1, inset; see also (4-7, 4-8, 4-9, 4-10, 4-11)). Our goal, however, is to instead develop quantitative methods of monitoring dissolution over multiple length scales.

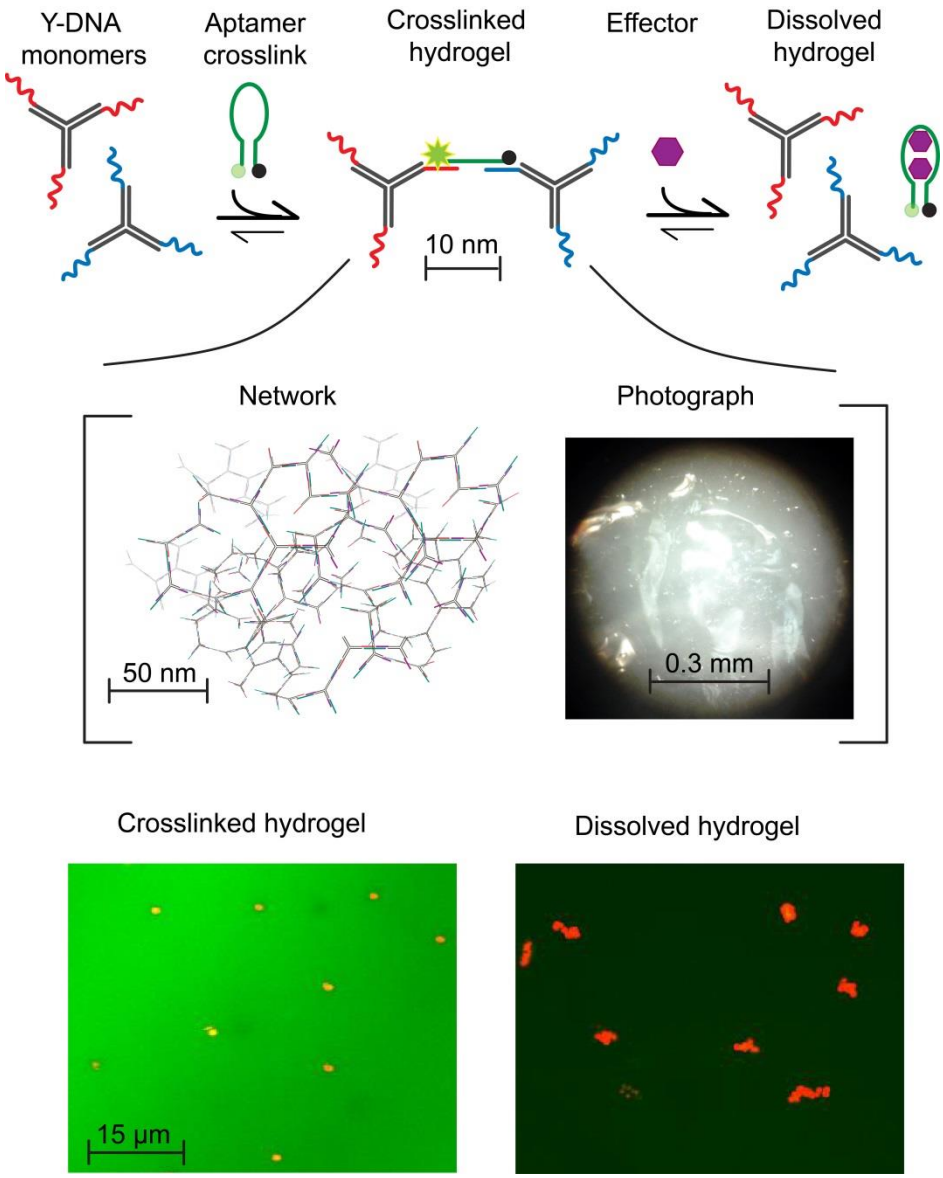

Figure 4-1. As our model system we employed an adenosine-responsive DNA hydrogel modeled on a Y-DNA hydrogel architecture first described by Cheng *et al.* (4-21). (***Top***) This consists of Y-shaped "monomers" (each consisting of three annealed strands of DNA) with pendant, single-stranded arms. These arms are partially complementary to an adenosine-binding aptamer, which crosslinks the monomers to form a 3-dimensional network (***inset, left***) that forms a visibly thick gel (***inset, right***). In response to binding its specific molecular effector, adenosine, the aptamer dissociates and folds, disrupting the hydrogel. (***Bottom left***) This composite image shows the average signal from the aptamer (green channel) and the maximum signal of the beads (red channel) over 20 frames (33 s), in an intact hydrogel. The fluorophore-quencher pair appended to ~1% of the aptamers is separated, producing high fluorescent output and thus a bright green image. The intact network traps the embedded beads so that they remain in place over the time window of this composite image. (***Bottom right***) This composite image shows a gel 25 min after the addition of 14 mM adenosine over

the same time window as left. Upon the addition of adenosine, the aptamer dissociates, decreasing the emission of the fluorphore labeled aptamers, and thus the aptamer-channel signal substantially decreases. The dissociation of the aptamer dissolves the gel network, dramatically increasing bead mobility.

To measure dissolution kinetics at the molecular scale we employ a trace (~1%) amount of crosslinking aptamer that has been modified on its termini with a fluorophore-quencher pair (*Figure 1, bottom*). When in its "open," crosslinking conformation the fluorophore and quencher are segregated and emission is high (Figure 1, bottom left). In the adenosine-bound conformation of the aptamer, however, the fluorophore and quencher are in close proximity emission is low (*Figure 1, bottom right*) (4-22). To measure dissolution kinetics at longer length scales, in contrast, we use passive rheology, a method commonly employed for measuring the mechanics of soft materials (4-23, 4-24, 4-25, 4-26, 4- 27). Specifically, we measure the mean square displacement of micron-scale beads embedded in the hydrogel as a function of time. Initially, the intact hydrogel restricts the movement of the beads so that they remain largely in place, "jiggling" only slightly in response to thermal fluctuations. As the network dissolves, the mean square displacement of the beads increases, eventually reaching that expected for unhindered Brownian diffusion through a liquid.

4.3 Results

Time-lapse images capturing the fluorescence of the trace amount of fluorophore-labeled aptamers indicate that the hydrogel's molecular-scale dissolution kinetics are biphasic, with a slow initial decrease in fluorescence (the "lag phase") followed by a near-exponential decrease (the "exponential phase") (*Figure 4-2, top* and *middle*). The kinetics of

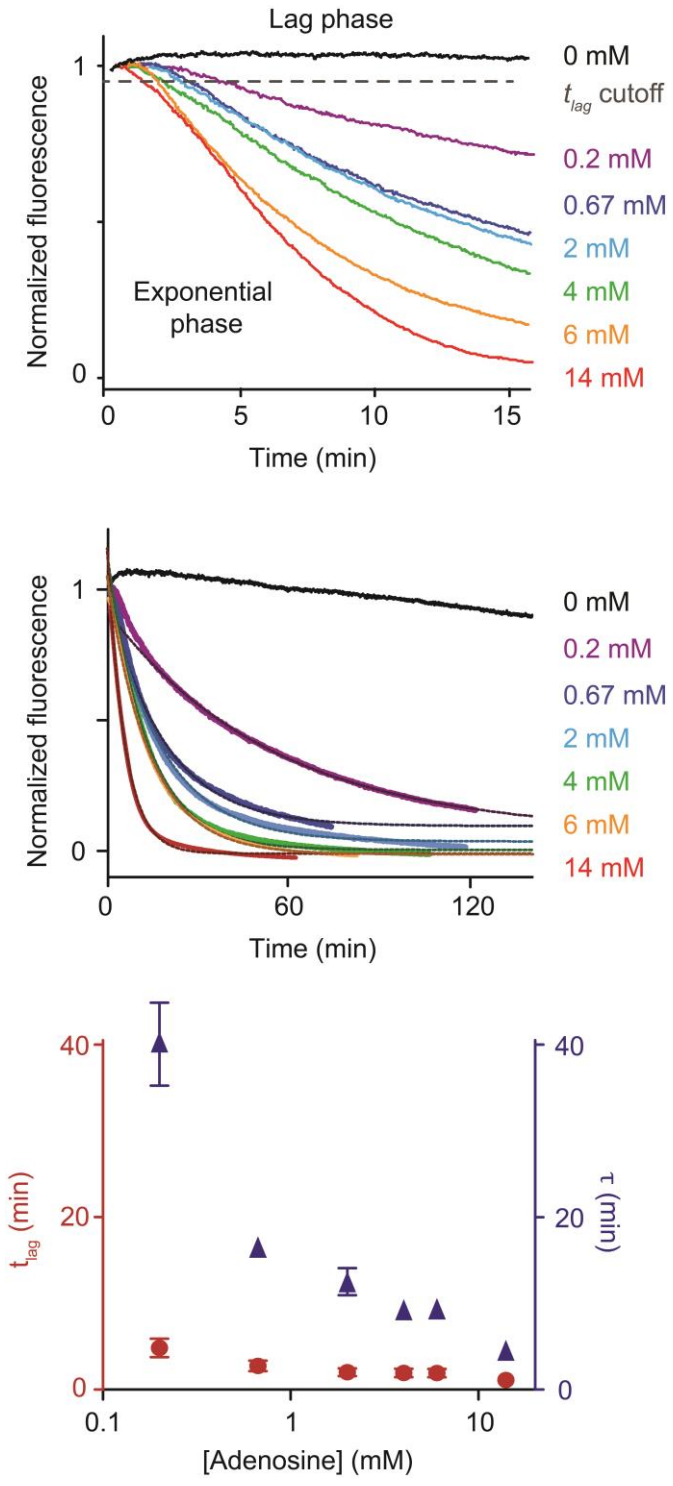

Figure 4-2. The adenosine-responsive hydrogel exhibits biphasic dissolution kinetics when the dissolution is monitored over molecular length scales. (***Top***) A close-up plot of the first 15 minutes after the addition of adenosine illustrates the concentration-dependent lag phase in the response of a trace of fluorophore-modified aptamer in the hydrogel. (***Middle***) This is followed by a concentration-dependent exponential dissolution phase. Note: near complete

dissolution is observed even at the lowest adenosince concentration we have employed. (***Bottom***) Both the lag time, t_{lag} (defined here as the time needed to decrease the initial fluorescence by 5%) and the lifetime, τ, of the exponential phase (determined after the fluorescence has decreased by 25%) increase monotonically with decreasing adenosine concentration.

each of these phases depends on the concentration of adenosine added. At a depth of 600 μm within the sample, for example, the length of the lag phase, which we define as the time required to reduce fluorescence by 5%, increases 3-fold (from 1.4±0.17 min to 4.2±0.13 min) as the adenosine concentration drops from 14 mM to 0.2 mM. The time constant of the exponential phase, which we obtain by fitting the decay observed after the initial fluorescence has decreased by 25%, depends still more strongly on adenosine concentration, increasing 10-fold (from 3.9±0.43 min to 38.3±0.13 min) over the same concentration range. Taken together, these two effects cause the overall time for dissolution to likewise rise monotonically with adenosine concentration: at a depth of 600 μm within the gel, for example, the time required to reduce the background-subtracted fluorescence to 50% of its initial value increases 7-fold (from 5.0±0.17 min to 37.2±6.1 min) over the same change in adenosine concentration (*Figure 4-2, middle*).

The dissolution kinetics of the gel also depend on the depth within the hydrogel at which the process is being monitored (*Figure 4-3*). Here, however, the dependence arises solely due to changes in the lag phase, as the time constant of the exponential phase is effectively independent of depth. In response to 6 mM adenosine, for example, the length of the lag phase increases 9-fold (from 0.2±0.2 min to 1.8±0.2 min) as the depth within the sample increases from 300 μm to 600 μm, an effect that presumably arises due to the finite

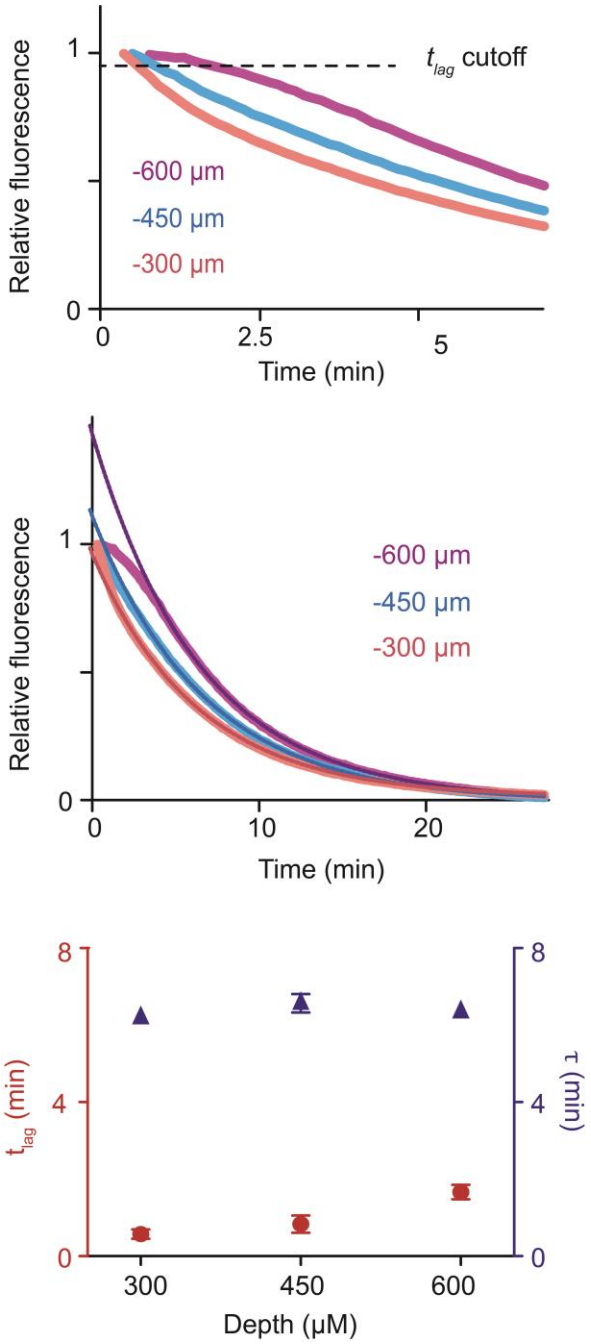

Figure 4-3. The lag time of the molecular scale dissolution depends on depth below the surface at which the observations are made. The exponential kinetics observed after the lag phase, however, are effectively independent of depth. (***Top***) The length of the lag phase, defined as the time required for the fluorescence to fall by 5%, increases monotonically with increasing depth. (***Middle***) After this initial depth-dependent lag phase, the fluorescence decreases with similar kinetics at all depths. (***Bottom***) The lag time t_{lag} increases from 0.6±0.2 mi at 300 µm to 1.8±0.1 min at 600 µm. The time constant constants of the exponential phase (fit when fluorescence has decreased by 25%), however, are near identical.

time required for the effector to diffuse into the material (4-20). The time constants of the exponential phases, in contrast, are near identical to within expected confidence intervals at all depths (*Figure 4-3*, *bottom*).

The final, net fluorescence we observe plateaus at near background levels after less than 150 min at all effector concentrations, suggesting that, at equilibrium, the hydrogel is completely dissolved at even the lowest (0.2 mM) adenosine concentration investigated. This observation was unexpected; effector binding must "outcompete" the hybridization of the aptamer to the monomers, which we believed would push the aptamer's dissociation constant far above 0.2 mM. Specifically, the secondary structure predicting software Mfold estimates the stability of the aptamer-Y-monomer base-pairing to be -60 kJ/mol (4-28, 4-29). Constraining the non-binding portion of the aptamer, however, is entropically unfavorably, and carries an energetic cost roughly equivalent to constraining the ends of a non-base pairing loop of a hairpin, which Mfold and polymer theory predict to be ~13 kJ/mol (4-28, 4-29, 4-30). Together, these effects would be expected to reduce the energy with which our aptamer crosslinkers bind to adenosine by 47 kJ/mol relative to the affinity of the free aptamer. This, in turn, should increase the 6 µM K_{half} of the free aptamer (4-22) by eight orders of magnitude. That our hydrogel completely dissociates even at 0.2 mM adenosine suggests, however, that the K_{half} is significantly less than 3 orders of magnitude above that of the free aptamer. This presumably occurs due to strain, which could substantially reduce the stability of the aptamer-monomer interactions and thus enhance the ease with which adenosine dissolves the hydrogel.

In addition to providing a measure of the hydrogel's dissolution kinetics, our approach also allows us to visualize the dissolution pattern of the hydrogel over time and

space, thus providing insight into the dissolution mechanism (*Figure 4-4*). Specifically, if dissolution were highly cooperative we might expect to see either patchy, punctate decreases in fluorescence, with dark spots forming and expanding at their edges in a nucleation-growth type pattern, or a wave-front pattern in which dissolution progresses from one side of the field of view to the other. Instead we observe an even decrease in fluorescence over the entire 120 μm x 120 μm field of view, suggesting that crosslinkers dissociate from the hydrogel randomly over time, rather than via a cooperative mechanism in which a dissociated crosslinker would increase the propensity of neighboring crosslinkers to dissociate.

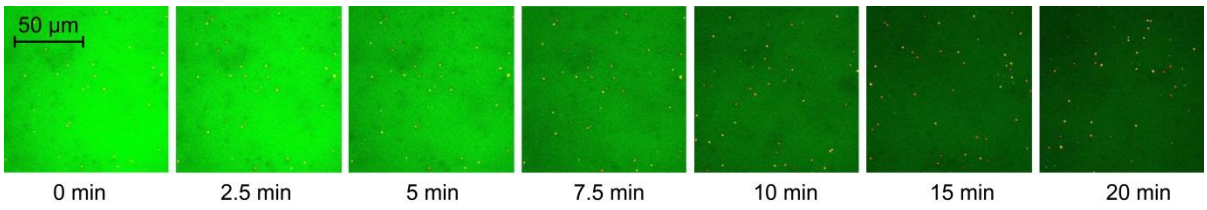

Figure 4-4. Sequential images of a dissolving hydrogel show a homogeneous decrease in aptamer fluorescence over time (green), indicating that, to the resolution of our image, the dissolution is spatially uniform. This stands in contrast to patchier, nucleation-like dissolution (in which small initial areas of dissolution form and expand) or wave front dissolution (in which dissolution occurs as a front advancing from one side). The latter observations might be expected were the dissolution process to be cooperative.

The dissolution of the hydrogel as probed over micron length scales (*Figure 4-5*, *top* and *middle*) is both slower and more strongly concentration-dependent than its dissolution at molecular length scales. For example, when we employ the mobility of 1.0 μm beads as our reporter, $t_{1/2}$ (the time required for the bead's mean squared displacement to reach half the value seen in buffer) ranges from 14.7±1.7 min at 14 mM adenosine to greater than 120 min

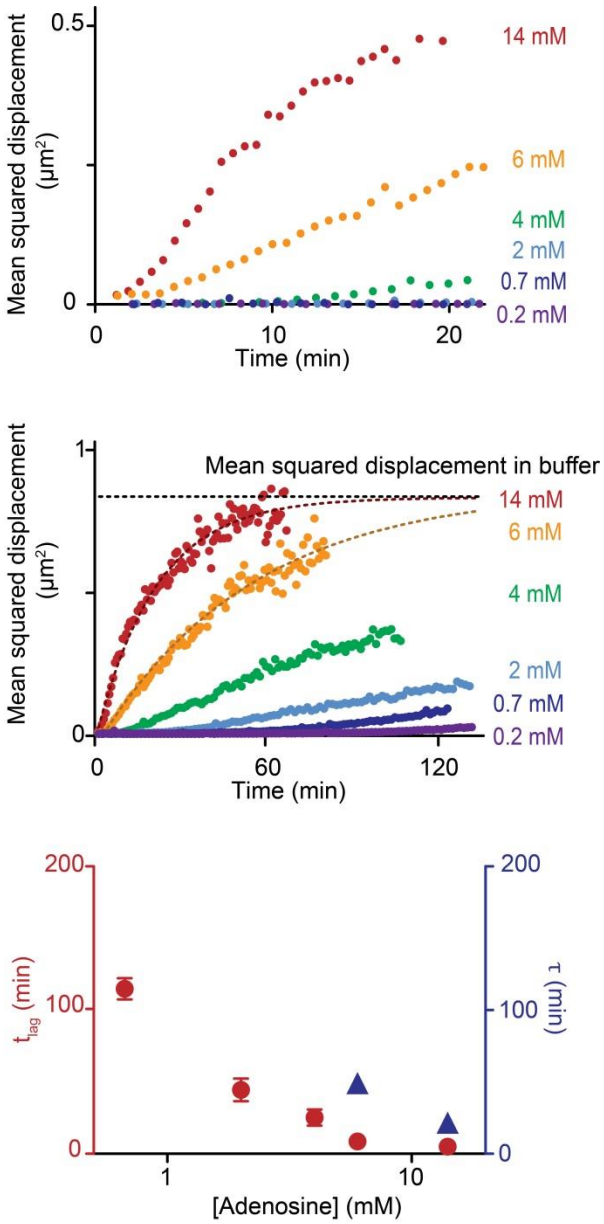

Figure 4-5. (***Top***) Like its molecular scale dissolution, the micron scale dissolution of the hydrogel exhibits an initial lag phase followed by (***Middle***) near-exponential behavior. Notably, very little increase in mobility occurs even after 120 minutes in response to lower than 2 mM adenosine. (***Bottom***) The lag time t_{lag} increases from 4.2±0.5 min at 14 mM adenosine to longer than 120 min at 0.2 mM adenosine. The time constants τ of the exponential fits are 19.6±2.3 min and 46.9±0.2 min at 14 mM and 6 mM respectively. At concentrations ≤ 4 mM, the bead motion does not reach the plateau value within the experimental time frame, preventing the extraction of characteristic exponential time constants.

at or above 2 mM. Here, too, the dissolution kinetics are biphasic, with a concentration-dependent lag phase followed by a concentration-dependent, near-exponential increase in mobility. The lag phase, which we define here as the time required for the mean square displacement to exceed 10% of what would be expected in buffer, ranges from 4.2±0.5 min at 14 mM adenosine to longer than the two hour experimental timeframe at 0.2 mM adenosine. The time constants of the exponential phase similarly range from 19.6±2.3 min at 14 mM to much greater than 2 hr at adenosine concentrations below 2 mM (*Figure 4-5, bottom*). At adenosine concentrations above 6 mM we observe bead mean square displacements that plateau at the mean squared displacement seen in water (e.g., 0.5 $\mu m^2/s$).

In contrast to the very different dissolution kinetics we observe at the molecular scale versus μm scale using the beads, the dissolution half-lives vary only modestly (*Figure 4-6*). Specifically, $t_{1/2}$ changes by only a factor of two (from 27.5±0.6 min to 47.1±4.2 min) despite a nearly 15-fold increase in bead diameter (*Figure 6, bottom*). What differences we do observe in the dissolution kinetics arise due to diameter-dependent changes in the lag time, which increases about 2.5-fold (from 6.0±0.7 min to 16.5±0.6 min as the bead diameter increases from 0.21 μm to 3.2 μm. The time constant of the exponential phase, in contrast, actually *de*creases with increasing bead size (from 46.3±6.3 min to 23.8±3.0 min). The increasing lag time with increasing bead size suggests that early in dissolution, the mesh size of the gel increases to enable increased movement of smaller beads, while staying sufficiently intact to trap the larger beads. Then, once the mesh size has decreased sufficiently to enable the movement of larger beads, the network has approached complete dissolution, resulting in a relatively short exponential phase for the larger beads.

Our ability to measure both the hydrogel's molecular scale dissolution and the extent to which it inhibits the motion of micron-sized beads simultaneously provides an opportunity to test Maxwell gelation and percolation theory (4-14, 4-15), relating a gel's crosslinking to its bulk mechanical properties. This theory predicts that above the percolation threshold, defined as the minimum fraction of intact crosslinkers for which there exists a continuous connected path through the gel, the mean square displacement should exhibit a power law relationship to the number of intact bonds. Below this threshold, in contrast, the gel network structure is no longer intact enough to trap the beads, and thus the mean squared displacement increases only slightly as the breakage of further bonds decreases the viscosity of the now liquid environment. Prior experimental (4-33, 4-34, 4-35) and simulation-based studies (4-13, 4-14, 4-15) support this theory, as do our observations For example, a plot of the normalized fluorescence, which captures the number of intact bonds, versus the mean squared displacement is biphasic, with an early power law-like phase transitioning into a plateau as the extent of dissolution increases and the hydrogel becomes liquid-like (*Figure 4-7*). The crossover between the two behaviors occurs when approximately 55% of the total fluorescence change has occurred (i.e., ~55% of the crosslinkers are broken), a value that is consistent with previous experimental observations and simulations of the gel point of amorphous gels (4-36).

4.4 Conclusions

We have developed and demonstrated simple, generalizable methods for quantitatively measuring the dissolution kinetics of a model stimulus-responsive hydrogel. The straightforward methods we have employed to do so may prove useful in the

optimization and development of artificial responsive hydrogels with optimized physical properties, and as a tool to improve the understanding of this increasingly important area of soft-matter physics.

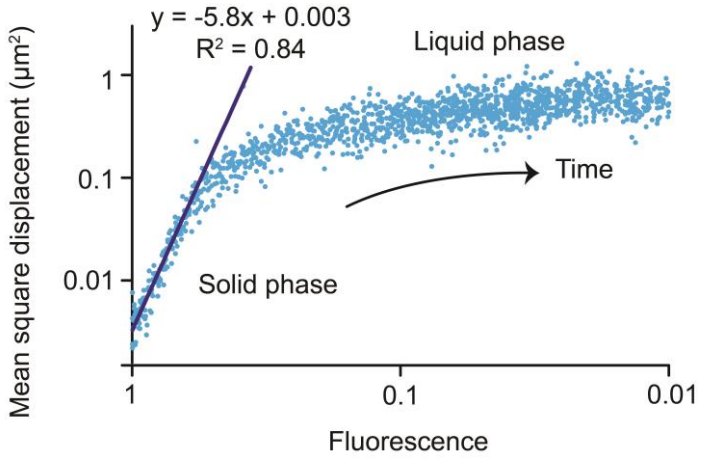

Figure 4-7. Plotting the fluorescent of the labeled aptamer versus the mean squared displacement of the beads during dissolution reveals a biphasic transition from solid-like to liquid-like behavior. Initially, when the material is in the solid phase, meaning that there are enough bonds intact to hold the beads in place, the mean squared displacement increases with decreasing fluorescence and thus fraction of intact bonds as a power law. When the number of bonds decreases enough to where the gel is no longer intact enough to hold the beads in place, the material undergoes a solid to liquid transition, where then beads are able to diffuse freely and mean squared displacement mean squared displacement only increases slightly with increasing bond breakage.

4.5 Materials and methods

Materials:

All reagent-grade chemicals, including adenosine, sodium phosphate monobasic, sodium phosphate dibasic, and sodium chloride were ordered from Sigma-Aldrich (St. Louis,

MI). Glass slides were purchase from Fisher Scientific (Hampton, NH). Unlabeled DNA and labeled DNA molecules were ordered from Sigma-Aldrich with desalt purification and Integrated DNA Technologies (Coralville, IA) with HPLC purification. Aqueous red Fluoro-Max beads of 0.21 µm, 1.0 µm, and 3.2 µm were ordered from Thermo Scientific (Waltham, MA). All reagents were used as purchased.

Each of the two Y-DNA monomers employed in this hydrogel consists of three subunit strands that hybridize to form a Y-shaped structure with a double-stranded core and pendant single-stranded functional ends. The core sequences are those first reported by Cheng *et al.* [7], and the single-stranded ends are complementary to eight and seven bases, respectively, on the 5' and 3' side, of the adenosine-binding aptamer of Huizenga and Szostak [22], hybridizing with Mfold-estimated free energies of -32.8 and -32.0 kJ/mol [22]. The sequences making up the monomers are as follows, with the double stranded core section denoted in italics and the elements complementary to the aptamer sequences underlined:

5' monomer subunit strands:

5a: 5' *CTTACGGCGAATGACCGAATCAGCCT* <u>ACCTTCCT</u>

5b: 5' *AGGCTGATTCGGTTCATGCGGATCCA* <u>ACCTTCCT</u>

5c: 5' *TGGATCCGCATGACATTCGCCGTAAG* <u>ACCTTCCT</u>

3' monomer subunit strands:

3a: 5' <u>CCCAGGT</u>*CTTACGGCGAATGACCGAATCAGCCT*

3b: 5' <u>CCCAGGT</u>*AGGCTGATTCGGTTCATGCGGATCCA*

3c: 5’ CCCAGGT*TGGATCCGCATGACATTCGCCGTAAG*

The aptamer strands are as follows, with the elements complementary to the Y-monomers underlined:

Unlabeled: 5’ ACCTGG*G*GGAGTATTGCGGAGGAAGGT

Labeled: 5’ Alexa488-ACCTGGGGGAGTATTGCGGAGGAAGGT-Black Hole Quencher1

Methods:

We synthesized each monomer by mixing a final concentration of 1.0 mM of each three component strands in 75 mM sodium chloride, 25 mM sodium phosphate, pH 7.0, then annealing by heating to 95°C for 5 min followed by cooling at a rate of 1°C/min to 4°C. We consistently achieved high yield of the desired products, which we confirmed using a 4-20% gradient acrylamide Tris/Borate/EDTA gel (100 V for approximately 45 minutes) stained with SYBR gold (*Figure 4-SI-1*). To form the hydrogels, we mixed final concentrations of 0.18 mM of each Y-monomer with 0.48 mM unlabeled aptamer, approximately 480 μM labeled aptamer, and 0.002% by volume red fluoromax beads in 60 mM sodium chloride, 20 mM sodium phosphate at pH 7.

We synthesized and imaged the hydrogels in a customized imaging flow cell. The cell consisted of a 1.8 mm diameter, 0.75 mm deep cylindrical well drilled into a 75 x 25 x 1.0 mm glass slide overlaid by a polydimethylsiloxane (PDMS) channel consisting of a square hole placed over the cylindrical well flanked by two 0.8 mm by 20 mm channels (*Figure 4-SI-2*). After synthesizing the gel in the well, we placed a glass coverslip over the PDMS

layer, covering the well but not the ends of the channel. After waiting at least 15 minutes to ensure complete gelation, we added 20 µl of adenosine solution to the top of the gel by pipetting it from one side of the channel. We imaged in an enclosed hutch maintained at 20°C with high humidity to minimize evaporation. For imaging we employed an upright Olympus Fluoroview FV1000 MPE laser scanning confocal microscope with a 25x magnification, 1.05 numerical aperture Olympus X Plan N lens. We simultaneously excited the aptamer fluorophore and fluorescent beads with 473 and 559 nm lasers, respectively, and detected via PMT detectors. Each frame was collected via raster scanning with a 512 x 512 pixel resolution and a 1.644 s^{-1} frame rate.

To obtain quantitative aptamer fluorescence decay curves we measured the average intensity of each image in the 473 nm fluorescence channel using ImageJ's batch measure function. We normalized each decay curve to the maximal and background fluorescence, which we obtained, respectively, by manually inputting the time of maximal fluorescence (generally at or shortly the addition of adenosine) and by fitting the last ~50% of the decay curve to an exponential equation using the Matlab cftool (see Matlab code section for code). To obtain fits of the exponential phase of the decay curves, we fit the portion where normalized fluorescence had decreased 25% from the maximal value to a simple exponential equation in Graph Pad plotting software. For each experimental condition (adenosine, bead size, and depth) we obtained at least triplicate measurements. We averaged the fluorescence of the replicates to obtain fluorescence versus time curves and the fit parameters of for each replicate to obtain average exponential time constants for each set of measurements.

We obtained bead tracks using the particle tracker function on Bitplane Imaris software. We analyzed this data to obtain the mean square displacements for all beads

present over each frame. To do this, we calculated the mean square change in distance over a frame between all sets of two beads present in both frames (excluding those separated by a distance less than 10x the bead diameter for the 0.21 μm and 1.0 μm beads and less than 3x the bead distance for the 3.2 μm beads to prevent correlated movement, see [25]), which is approximately equal to twice the mean squared displacement (SI Derivation 1), then multiplied the values we obtained by 0.5F. or visual clarity, we binned each mean square displacement versus time curve over 100 bins for Figures 4-4 and 4-5. We fit the time versus mean square displacement curves to simple exponential equations in GraphPad, reporting the averaged mean squared displacement for a given bin for several replicates for each condition. To obtain the fluorescence versus mean squared displacement plot (*Figure 4-6*), we plotted a representative non-binned bead data trace against the normalized fluorescence at the same time.

4.6 Matlab scripts

1. Function for plotting raw fluorescence.

```
%Raw fluorescence data plotting function
%Plaxco Group

%This function will pull the fluoresence data from the CSV file generated
%by ImageJ. It will then normalize to a percent max format, and feed the
%final data matrix back into the program that called this function as the
%variable "fluoro_data", in which the first column is the time stamp and
%the second column is the normalized fluoresence data.



function fluoro_data = FNC_Fluoro_Plot_041415_rawdata_forpaper(filename,
maxfluor)
    %"filename" is the name CSV file obtained by imagej batch measure of
the images
    %"maxfluor" is the frame number which contains what we hold to be the
    %maximum fluorescence, which is the fluorescence obtained immediately
```

```
    %after the addition of adenosine

    %Read the data file "filename"
    RawdataALL = csvread(filename,1);

    %Extract the first and third columns, which contain the frame number
and the fluorescence.
    Rawdata = [RawdataALL(:,1) RawdataALL(:,3)];

    %Make a matrix with just the fluorescence values
    Fluor_vals=Rawdata(:,2);

    %Obtain the maximum fluorescence, which occurs at the manually-input
    %time "maxfluor"
    peak_fluor = Fluor_vals(maxfluor);

    %Obtain all of the fluorescence values as fractions of the maximal
    %fluorescence by dividing by the peak fluorescence
    NormF = (Fluor_vals/peak_fluor);


    %Make a matrix with just the frame values
    frame = Rawdata(:,1);


    %Compile the normalized data into a matrix for (optional) plotting
    NormalData=[frame(maxfluor:length(frame))
NormF(maxfluor:length(frame))];

    % Remove discontinuities due to moving the focus, etc for easier
fitting
    % later:
    % Start by defining an empty matrix to do this
    no_disc_data = [];

    % for the whole data set:
    for position = 3:length(NormalData(:,1));
        %get the fluorescence for that data point
        num2=NormalData(position,2);
        %get the fluorescence for one point before that data point
        num1=NormalData(position-1,2);
        %get the fluorescence for two points before that data point
        num0=NormalData(position-2,2);
        %if the data point is not < 65% of the one before it
        if num2/num1 > 0.65;
            %if the data point that one is not < 65% of the one before it
            if num1/num0 > 0.65;
                %add to the data set without discontinuities
                no_disc_data = [no_disc_data; NormalData(position,1)
NormalData(position,2)];
            end
        end
    end
```

```
    % Get a data set only including the time after the addition of
    % adenosine for curve fitting
    % First, get a no-discontinuity data from the time that
    % fluorescence is added (assumed to be maxfluor) to ten points before
    % the end of the set
    FittingDataSet =
no_disc_data((round(maxfluor):round(length(no_disc_data)-10)),:);

    %Subtract the frame where fluorescence is added from all of the times
    %to get the frame number after the addition of fluorescence
    frame = FittingDataSet(:,1)-maxfluor;
    %Get the fluorescent values with the discontinuities removed
    fluoro =FittingDataSet(:,2);
    %The final output is the zero corrected time and the normalized
    %fluorescence values, with the discontinuities removed
    fluoro_data = [frame fluoro];

    % optional plot toggle on/off
    % plot(fluoro_data(:,1),fluoro_data(:,2), color);
```

2. Function for normalized raw fluorescence.

```
%Background subtracted plotting function
%Plaxco group

%This function will pull the fluoresence data from the CSV file generated
%by ImageJ. It will then normalize the fluorescence to the percent maximum
fluorescence (the
%fluoresence at the chosen max time) and the background levels previously
%obtained by fitting the previous data curves to find their background. It
%will also correct the time so that the frame in which the adenosine is
%added is equal to time zero, even if the maximal fluorescence occurs
%later.


function fluoro_data = FNC_Fluoro_Plot_060415_baselinesubtr(filename,
maxfluor,baseline, realstarttime);
    %"filename" is the name CSV file obtained by imagej batch measure of
the images
    %"maxfluor" is the frame number which contains what we hold to be the
    %maximum fluorescence, which is the fluorescence obtained immediately
    %after the addition of adenosine
    %"baseline" is the baseline calculated by fitting the
    %non-baseline-subtracted raw data to an exponential function to find
    %the baseline
    %realstarttime is the time at which we add the adenosine, which is
    %generally a few frames before the time of maximal fluorescence due to
    %the gel swelling and settling before then.

    %Read the data file "filename"
    RawdataALL = csvread(filename,1);
```

```
    %Extract the first and third columns, which contain the frame number
and the fluorescence.
    Rawdata = [RawdataALL(:,1) RawdataALL(:,3)];

    %Make a matrix with just the fluorescence values
    Fluor_vals=Rawdata(:,2);

    %Obtain the maximum fluorescence, which occurs at the manually-input
    %time "maxfluor"
    peak_fluor = Fluor_vals(maxfluor);

    %Obtain all of the fluorescence values as fractions of the maximal
    %fluorescence by dividing by the peak fluorescence
    NormF = (Fluor_vals/peak_fluor);

    %Correct to set the baseline at zero
    NormF_baselinesub = (NormF-baseline)/(1-baseline);


    %Make a matrix with just the frame values
    just_frame_numbers = Rawdata(:,1);


    %Compile the normalized data into a matrix for (optional) plotting
    NormalData=[just_frame_numbers(maxfluor:length(just_frame_numbers))
NormF_baselinesub(maxfluor:length(just_frame_numbers))];


    %Compile the normalized data into a matrix for (optional) plotting
    NormalData=[just_frame_numbers(maxfluor:length(just_frame_numbers))
NormF(maxfluor:length(just_frame_numbers))];

    % Remove discontinuities due to moving the focus, etc for easier
fitting
    % later:
    % Start by defining an empty matrix to do this
    no_disc_data = [];

    % for the whole data set:
    for position = 3:length(NormalData(:,1));
        %get the fluorescence for that data point
        num2=NormalData(position,2);
        %get the fluorescence for one point before that data point
        num1=NormalData(position-1,2);
        %get the fluorescence for two points before that data point
        num0=NormalData(position-2,2);
        %if the data point is not < 65% of the one before it
        if num2/num1 > 0.65;
            %if the data point that one is not < 65% of the one before it
            if num1/num0 > 0.65;
                %add to the data set without discontinuities
                no_disc_data = [no_disc_data; NormalData(position,1)
NormalData(position,2)];
            end
```

```
        end
    end


    % Get a data set only including the time after the addition of
    % adenosine for curve fitting
    % First, get a no-discontinuity data from the time that
    % fluorescence is added (assumed to be maxfluor) to ten points before
    % the end of the set
    FittingDataSet =
no_disc_data((round(maxfluor):round(length(no_disc_data)-10)),:);

    %Subtract the frame where fluorescence is added from all of the times
    %to get the frame number after the addition of fluorescence
    just_frame_numbers = FittingDataSet(:,1)-maxfluor;
    %Get the fluorescent values with the discontinuities removed
    fluoro =FittingDataSet(:,2);
    %The final output is the zero corrected time and the normalized
    %fluorescence values, with the discontinuities removed
    fluoro_data = [just_frame_numbers fluoro];

    % optional plot toggle on/off
    % plot(fluoro_data(:,1),fluoro_data(:,2), color);
```

3. Function for plotting bead mean square displacements.

```
%Bead plotting function
%Plaxco group

%This function will pull data from the particle tracking CSV file
generated
%by the Imaris software. The function can then calculate the average
squared change
%in particle seperation between all particles as a function of time.
%The output is presented in the variable "MSD_InterBead_Distance", which
%contains the timestamp in the first column and the average squared change
%in interbead distance in the second column.


function MSD_InterBead_Distance =
Luke_msd_interbead_addstart061015_forpaper(filename, limit, pointadded,
bin_on_off, color, distancecutoff, maxdisplacement)
    %"filename" is the name of the file obtained from Imaris containing
the
    %positions, times, and IDs for the beads. The format is [x position, y
    %position, z position (not tracked so arbitrary), time, bead id, and
    %point id
    %"limit"
    %"pointadded" is the frame at which we added the adenosine
    %"color" is the color for (optional) plotting
    %"distancecutoff" is the distance cutoff below which we do not
consider
    %the change in distance between bead pairs. Generally we input ~10x
    %bead diameter (see [ref two point microscopy paper,
```

```
    %Crocker/Valentine/Weitz])
    %"maxdisplacement" is the maximal one-frame displacement of the bead
    %that we would assume to be real, i.e., not a tracking error

    %import data file
    datafile = csvread(filename,1);

    %get the total number of points
    numberpts = length(datafile);

    %Imaris sets the bead index to a nine digit number, in the format
    %"10000001, 10000002, 1e9 + n" for the 1st,
    % 2nd, nth beads. Set this to just 1, 2, n format for easier viewing
    for n = 1:numberpts;
        datafile(n,5) = datafile(n,5)-1e9;
    end

    %Sort the data by the bead I.D.
    datasorted = sortrows(datafile, 5);


    %Caculate the displacement of each bead over one frame intervals and
store those displacements in a list
    %and store those displacements in a list.
    %Make an empty list for displacements
    xdisplacements = [];
    %For each row in the matrix (i.e., for each datapoint)
    for line = 2:numberpts;
        % if the bead ID of that point is the same as that of the previous
point
        if datasorted(line,5) == datasorted(line-1,5);
            %get the time of that point
            timeindex = datasorted(line, 4);
            %if the time is after the time when we added the adenosine
            if timeindex >= pointadded;
                %obtain the x and y positions of that bead at the given
                %point
                xposition = datasorted(line,1); yposition =
datasorted(line,2);
                %calculate the displacement, from the frame before the
                %current one to the current one
                xdisp = datasorted(line,1)-datasorted(line-1,1);
                %get the bead number
                bead_number = datasorted(line, 5);
                % if the displacement of the bead is less than the upper
                % limit maxdisplacement:
                if abs(xdisp) < maxdisplacement;
                    %append the bead's timeindex, x displacement, ID, x
                    %position, and y position to the list
                    xdisplacements = [xdisplacements; timeindex xdisp
bead_number xposition yposition];
                end
            end
        end
    end
```

```
    %Sort the xdisplacements by time
    sort_by_time = sortrows(xdisplacements, 1);

    %Find where the frame number changes in order to find the row numbers
    %in xdisplacements that correspond to each frame.
    %Make an empty list for these points
    cut_points = [];
    %for each row but the first in the list of displacements sorted by
time
    for row = 2:length(sort_by_time);
        %if the time index of a data point is NOT equal to the time index
        %of the next in the sort_by_time matrix, that means that the bead
        %ID is different, so that it is the start of a new series of
beads.
        %If this is the case, then add this index to the list of
        %cut_points.
        if sort_by_time(row, 1) ~= sort_by_time(row-1,1);
            point = row;
            cut_points = [cut_points; point];
        end
    end

    %Extract the single frame delta displacements from the xdisplacements
list,
    %using the cut_points values as row cut-offs.
    % Make an empty matrix to do this
    Single_Frame_Delta_Disps = [];
    %For each line between 3 and the number of cut points
    for line = 3:length(cut_points);
        %the end of displacements for those time intervals
        end_time = cut_points(line);
        %the start of the set of that time intervals
        start_time = cut_points(line-1);
        %the displacements at those time intervals
        data_thatcutpoint = sort_by_time(start_time:end_time-1,:);
        %if the frame has more than one bead in it, then continue (if not,
        %skip)
        if length(data_thatcutpoint(:,1)) ~= 1;
            %Find the difference in displacement for each combination of
            %beads, which corresponds to the change in the inter-bead
            %distance over one frame for that pair.
            %First, set a temporary matrix to do this
            temp_inter_dist_storage =[];
            %for "bead one" present at the time points
            for bead_one = 1:length(data_thatcutpoint(:,1));
                %for each "bead two" also present at that time point and
further down on the list
                for bead_two = bead_one+1:length(data_thatcutpoint(:,1));
                    %get the x position of both beads and the distance
                    %between them
                    xpos_one = data_thatcutpoint(bead_one,4); xpos_two =
data_thatcutpoint(bead_two,4); xdistance = xpos_one - xpos_two;
                    %get the y position of both beads and the distance
                    %between them
```

```
                    ypos_one = data_thatcutpoint(bead_one,5); ypos_two =
data_thatcutpoint(bead_two,5); ydistance = ypos_one - ypos_two;
                    %get the horizontal distance between the beads
                    %(pythagorean theorum)
                    distancebtbeads = sqrt(xdistance.^2 + ydistance.^2);
                    %if the distance is greater than required by the
cutoff
                    if distancebtbeads > distancecutoff;
                        inter_dist = data_thatcutpoint(bead_two, 2)-
data_thatcutpoint(bead_one,2);
                        %get the bead IDs
                        bead_one_id = data_thatcutpoint(bead_one,3);
                        bead_two_id = data_thatcutpoint(bead_two,3);
                        %Square the distance and place it in a storage
matrix with the bead IDs.
                        temp_inter_dist_storage =
[temp_inter_dist_storage; inter_dist^2 bead_one_id bead_two_id];
                    end
                end
            end
            %Average the change in displacement for all the combinations
of
            %beads in that frame.
            ave_inter_dist_change = mean(temp_inter_dist_storage(:,1));
            if ave_inter_dist_change < 10; %to prevent artifacts
                Single_Frame_Delta_Disps = [Single_Frame_Delta_Disps;
data_thatcutpoint(1,1) ave_inter_dist_change];
            end
        end
    end

    %If binning is toggled "on," bin the data over 100 bins to make it
    %easier to interpret
    if bin_on_off == 1;
        %set the number of bins to 100
        num_bins = 100;
        %find the bin step size by dividing the number of frames by 100
        bin_step_size = int64(length(Single_Frame_Delta_Disps)/num_bins)-
1;
    end

    %If binning is toggled "off," the bin step size is set as zero
    if bin_on_off == 0;
        bin_step_size = 1;
        limit = limit/1;
    end

    %set an empty matrix for the binned data
    binned_data_mat = [];
    %step through the data looking at each window, the size of which is
    %defined by bin_step_size
    for row =
bin_step_size:bin_step_size:length(Single_Frame_Delta_Disps);
        %put the data for each bin window in a temporary matrix for
        %averaging
        temp_bin_matrix = [];
```

```
        %for each
        for group = row-bin_step_size+1:row;
            temp_bin_matrix = [temp_bin_matrix;
Single_Frame_Delta_Disps(group,1) Single_Frame_Delta_Disps(group,2)];
        end
        %average the data in the bin window, then store the result in the
        %main data matrix
        binned_data_mat = [binned_data_mat; mean(temp_bin_matrix(:,1) -
pointadded) mean(temp_bin_matrix(:,2))];
        %setting this number (below) will change the max length of the
data
        %set.  If you get a "horzcat", lower this number to your smallest
        %matrix dimension
        if length(binned_data_mat) >= round(limit);
            break
        end
    end
    %plot the binned results (optional)
    plot(binned_data_mat(:,1), binned_data_mat(:,2), color);
    %return the binned interbead distances
    MSD_InterBead_Distance = binned_data_mat(2:length(binned_data_mat),:);
end
```

4.7 Supplementary figures

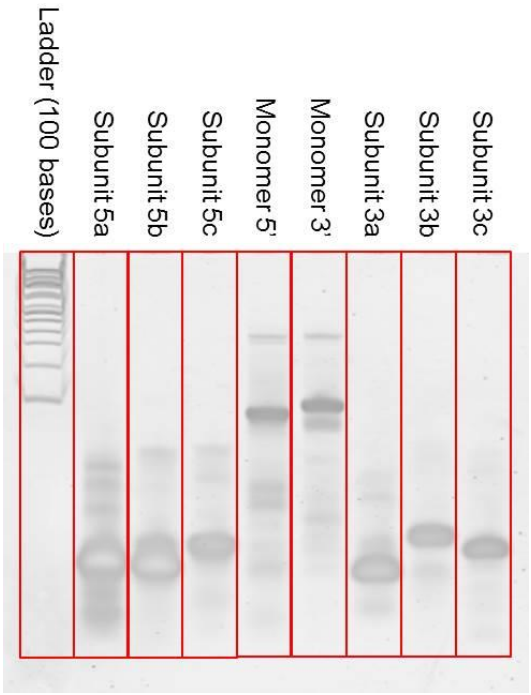

Figure 4-SI-1. We confirmed the successful synthesis of our monomers by running on a TBE gel and staining with sybr gold. The monomers' mobility was considerably lower than that of the individual subunits, indicating successful formation of the product.

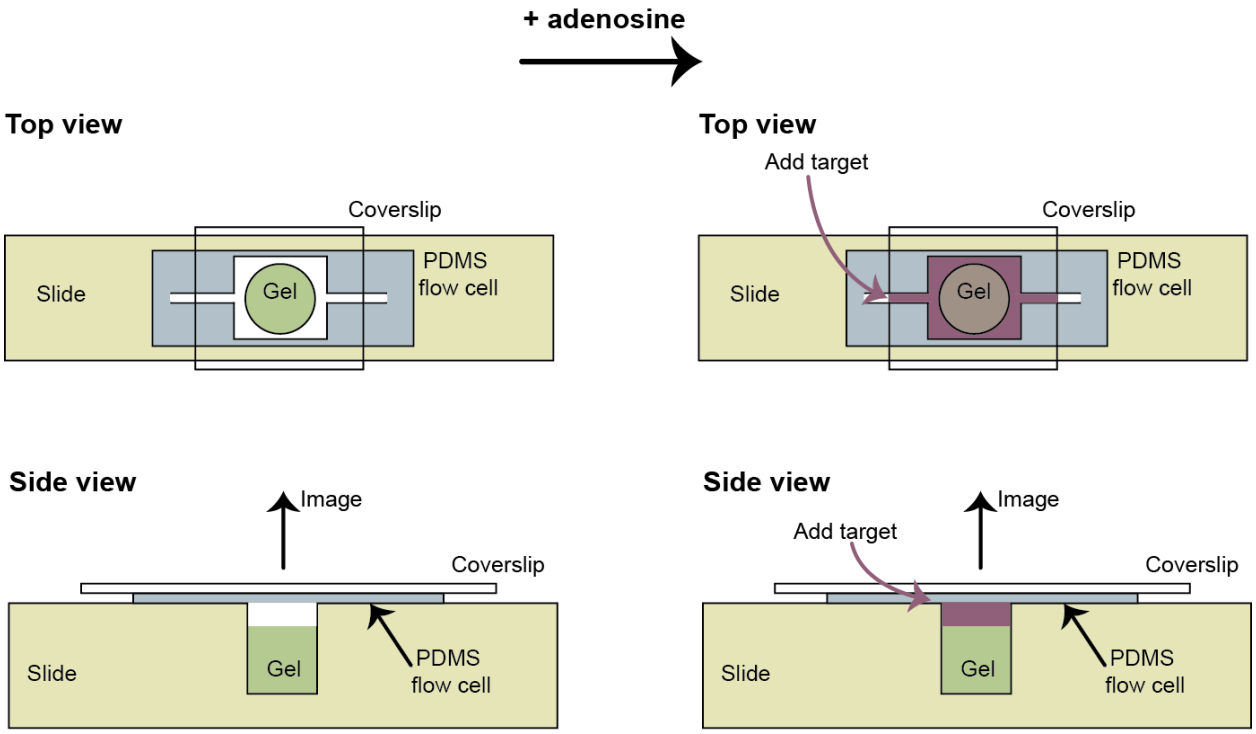

Figure 4-SI-2. We constructed a flow cell to enable precise addition of the adenosine solution and imaging of the gels.

4.8 Supplementary derivation

Mean square displacement is defined as the average squared displacement that a particle moves in a given time interval t. One dimensional mean square displacement is thus defined as:

$$Mean\ squared\ displcement = < x^2(t) >= < [x(t+T) - x(T)]^2 > = \sum_n [x_n(t+T) - x_n(T)]^{\,2} / n$$

Where t is the time interval, T is the first time where position is measured, and x_n is the position of particle n.

To eliminate effects from drift and flow, instead of measuring the mean square displacement, we measure the mean square change in position between two particles. The change in distance between two particles a and b over time t is thus equal to the difference in their displacements over t:

$$\Delta D_{ab}(t) = [x_a(T+t) - x_b(T+t)] - [x_a(T) - x_b(T)]$$

$$= x_a(T+t) - x_a(T) - [x_b(T+t) - x_b(T)]$$

$$= \Delta x_a(t) - \Delta x_b(t)$$

The mean square change in difference in positions is thus equal to :

$$< \Delta D_{ab}(t)^2 > = < [\Delta x_a(t) - \Delta x_b(t)]^2 > = < \Delta x_a(t)^2 + \Delta x_b(t)^2 + 2\Delta x_a(t)\Delta x_b(t) >$$

Because the particle motion is random, neglecting interactions between particles, the average value of the term $2\Delta x_a(t)\Delta x_b(t)$ is equal to zero. Thus:

$$< \Delta D_{ab}(t)^2 > = < \Delta x_a(t)^2 + \Delta x_b(t)^2 > = 2\Delta < x_n(t)^2 >$$

$$= 2 * Mean\ square\ displacement$$

4.9 References

4-1. Pollard TD (2014). The value of mechanistic biophysical information for systems-level understanding of complex biological processes such as cytokinesis. *Biophys Journal* **107**:2499-2507

4-2. Zlotnick A, Mukhopadhyay S (2011). Virus assembly, allostery, and antivirals. *Trends in Microbiology* **19**:14-23

4-3. Jahn R, Fasshauer D (2012). Molecular machines governing exocytosis of synaptic vesicles. *Nature* **490**:201-207

4-4. Meyers MA, McKittrick H, Chen P-Y (2013). Structural biological materials: critical mechanics-materials connections. *Science* **339**:773-779

4-5. Whitesides GM, Grzybowski B (2002). Self-assembly at all scales. *Science* **29**:2418-2421

4-6. Biffi S, Cerbino R, Nava G, Bomboi F, Sciortino F, Bellini T (2015). Equilibrium gels of low-valence DNA-nanostars: a colloidal model for strong glass formers. *Soft Matter* **11**:3132-3138

4-7. Cheng E, Xing Y, Chen P, Yang Y, Sun Y, Zhou D, Xu L, Fan Q, Liu D (2009). A pH-triggered, fast-responding DNA hydrogel. *Angew Chem* **121**:7776-7799

4-8. Helwa Y, Dave N, Froidevaux R, Samadi A, Liu J (2012). Aptamer-functionalized hydrogel microparticles for fast visual detection of mercury(II) and adenosine. *ACS App Mater Interfaces* **4**:2228-2233

4-9. Wei X, Tian T, Jia S, Zhu Z, Ma Y, Sun J, Lin Z, Y CJ (2015). Target-responsive DNA-hydrogel mediated "stop-flow" microfluidic paper-based analytic device for rapid, portable, and visual detection of multiple targets. *Anal Chem* **87**:4275-4282.

4-10 Zhang L, Lei J, Liu L, Li C, Ju H (2013). Self-assembled DNA hydrogel as switchable material for aptamer-based fluorescent detection of protein. *Anal Chem* **85**:11077-11082

4-11. Guo W, Qi X-J, Orbach R, Lu C-H, Freage L, Mironi-Harpaz I, Seliktar D, Yang H-H, Willner I (2014). Reversible Ag^{+}-crosslinked DNA hydrogels. *Chem Commun* **50**:4065-4068

4-12. Rovigatti L, Smallenburg F, Romano F, Sciortino F (2014). Gels of DNA nanostars never crystallize. *ACS Nano* **8**:3567-3574.

4-13. Broedersz CP, Mao X, Lubensky TC, MacKintosh FC (2011). Criticality and isostaticity in fibre networks. *Nature Physics* **7**:983-989

4-14. Mao X, Stenull O, Lubensky TC (2013). Effective-medium theory of a filamentous triangular lattice. *Phys Rev E* 042601

4-15. Sahimi M, Arbabi S (1993). Mechanics of disordered solids. II. Percolation on elastic networks with bond-bending forces. *Phys Rev B* **47**:703-713

4-16. Lin C-C, Metters AT (2006). Hydrogels in controlled release formulations: Network design and mathematical modeling. *Adv Drug Deliv Rev* **58**:1370-1408

4-17. Yu G, Yan X, Han C, Huang F (2013). Characterization of supramolecular gels. *Chem Soc Rev* **42**:6697-6722

4-18. Bae KH, Wang L-S, Kurisawa M (2013). Injectable biodegradable hydrogels: progress and challenges. *J Mater Chem B* **1**:5371-5388

4-19. Hirst AR, Coates IA, Bocheteau, Miravet JF, Escuder B, Castelletto V, Hamley IW, Smith DW (2008). Low-molecular-weight gelators: Elucidating the principles of gelation based on gelator solubility and a cooperative self-assembly model. *J Am Chem Soc* **130**:9113-9121

4-20. Narasimhan B (2001). Mathematical models describing polymer dissolution: consequences for drug delivery. *Adv Drug Deliv Rev* **48**:195-210

4-21. Wyart M, Liang H, Kabla A, Mahedevan L (2008). Elasticity of floppy and stiff random networks. *Phys Rev Lett* **101**:215501

4-22. Huizenga DE, Szostak JW (1995). A DNA aptamer that binds adenosine and ATP. *Biochemistry* **34**:656-665

4-23. Aufderhorst-Roberts A, Frith WJ, Donald AM (2014). A microrheological study of hydrogel kinetics and microheterogeneity. *Eur Phys J E* **37**:44

4-24. Larsen TL, Furst EM (2008) Microrheology of the liquid-solid transition during gelation. *Phys Rev Lett E* 146001

4-25. Crocker JD, Valentine MT, Weeks ER, Gisler T, Kaplan PD, Yodh AG, Weitz DA (2000). Two-point microrheology of inhomogenous soft materials. *Phys Rev Lett* **85**:888-891

4-26. Moschakis T, Murray BS, Dickinson E (2010). On the kinetics of acid sodium caseinate gelation using particle tracking to probe the microrheology. *J Colloid Interface Sci* **345**:278-285

4-27. Schultz KM, Baldwin AD, Kiick KL, Furst EM (2012). Measuring the modulus and reverse percolation transition of a degrading hydrogel. *ACS Macro Lett* **1**:706-708

4-28. Chan HS, Dill KA (1989) Intrachain loops in polymers. *J Chem Phys* **90**:492–509

4-29. SantaLucia JR (1998) A unified view of polymer, dumbbell, and oligonucleotide DNA nearest-neighbor thermodynamics. *Proc Natl Acad Sci USA* **95**(4):1460-1465.

4-30. Zuker M (2003) Mfold web server for nucleic acid folding and hybridization prediction. *Nucl Acids Res* **31**:3406-3415.

4-31. Lieleg O, Vladescu I, Ribbeck K (2010). Characterization of particle translocation through mucin hydrogels. *Biophys J* **98**:1782-1789

4-32. Lai SK, Wang Y-Y, Hida K, Cone R, Hanes J (2009). Nanoparticles reveal that human cervicovaginal mucus is riddled with pores larger than viruses. *Proc Natl Acad Sci USA* **107**:598-603

4-33. Schultz KM, Baldwin AD, Kiick KL, Furst EM (2012). Measuring the modulus and reverse percolation transition of a degrading hydrogel. *ACS Macro Lett* **1**:706-708

4-34. Mukyasasmita W, Lee JS, Heilshorn SC (2011). Molecular-level engineering of protin physical hydrogels for predictive sol-gel phase behavior. *Biomacromolecules* **12**:3406-3411.

4-35. Normand V, Lootens DL, Amici E, Plucknett KP, Aymard P (2000). New insight into agarose gel mechanical properties. *Biomacromolecules* **1**:730-738

4-36. Rudin A, Choi P. The Elements of Polymer Science and Engineering, 3rd Edition. 2012. Elsevier Science. p 410

4.10 Funding and acknowledgements

We thank Mary Raven for training and technical support with imaging and Omar Saleh and Megan Valentine for helpful discussions regarding the interpretation of bead tracking data. This work was supported by the Beckman Scholars program funded by the Arnold and Mabel Beckman Foundation, and from the Institute for Collaborative Biotechnologies through Grant W911NF-09-0001 from the U.S. Army Research Office. The content of the information does not necessarily reflect the position or the policy of the Government, and no official endorsement should be inferred. We also acknowledge the use of the NRI-MCDB Microscopy Facility and the Multiphoton/Laser Scanning Confocals supported by the NCRR and Office of The Director, National Institutes of Health of the NIH under Award # S10RR022585 and # S10OD010610 respectively.

V. QUANTITATIVE CONTROL OF THE RESPONSE KINETICS AND THERMODYNAMICS OF A "SMART" DNA HYDROGEL

Recent years have seen an increasing interest in biomimetic, stimulus-responsive hydrogels fabricated from DNA. The successful introduction of these materials into artificial technologies, however, requires the ability to quantitative control their response kinetics. Achieving this control may be, in principle, rather straightforward, as DNA's simple, modular structure enables the construction of precisely-organized three-dimensional networks and the quantitative control of the thermodynamics and kinetics of aptamer-target molecule binding. However, the relationship between the readily controllable structural properties of these DNA and aptamer hydrogels, for example the network geometry and thermodynamic stability, and their resulting physical properties, for example the kinetic response to target molecule and the relationship between molecular-scale and micron-scale dissolution, remains poorly understood. In response, here we have measured the time-resolved, multi-scale dissolution of a model adenosine-responsive Y-DNA hydrogel in order to investigate the relationship between the gel's response kinetics and the geometry and thermodynamics of the base-pairing that underlies its formation. We find that, as expected, the hydrogel dissolution kinetics decreases with increasing affinity between the hydrogel's monomers and aptamer crosslinker, albeit the base pairing geometry plays an important role as well. This chapter is in preparation for submission in fall 2015.

5.1 Motivation

Materials that assemble and dissolve in response to molecular cues are ubiquitous throughout biology (5-1, 5-2, 5-3, 5-4, 5-5). The ability to engineer such responsive materials would likely be of value in artificial biotechnologies, ranging from drug delivery vehicles to biosensors to switchable-surface materials. To create such responsive materials many researchers have turned to DNA as its modular, well-understood base-pairing rules support the construction of precisely organized three-dimensional structures and networks (5-6, 5-7, 5-8, 5-9, 5-10, 5-11, 5-12). Moreover, by employing structure-switching aptamers, DNA sequences that bind specific target molecules, as crosslinking elements key to the structural integrity of the hydrogel, these hydrogels can be made to assemble or dissolve in response to specific chemical cues. Many successful examples of such aptamer-crosslinked responsive hydrogels exist, including hydrogels that respond to pH (5-7), mercury (5-8), adenosine (5-9, 5-10, 5-12), cocaine (5-9), lead (5-9), thrombin (10), and silver (11).

The modular, well-understood base pairing rules of DNA suggests, in principle, that the engineering of responsive DNA hydrogels with precisely tuned thermodynamic and kinetic properties may be quite straightforward. That is, because DNA-DNA interactions occur primarily through simple, quantitatively-understood Watson-Crick base pairing, quantitative control of the thermodynamics and kinetics between DNA-DNA components may be readily achieved through simple changes in base pairing length, geometry, or extent of guanine-cytosine base pairs (5-13). Although the binding of aptamers to their target molecules is less well-understood then Watson-Crick base-pairing, control of the thermodynamics and kinetics of aptamers binding their target molecules may be achieved by tuning the thermodynamic and kinetic equilibrium between binding-competent and non-

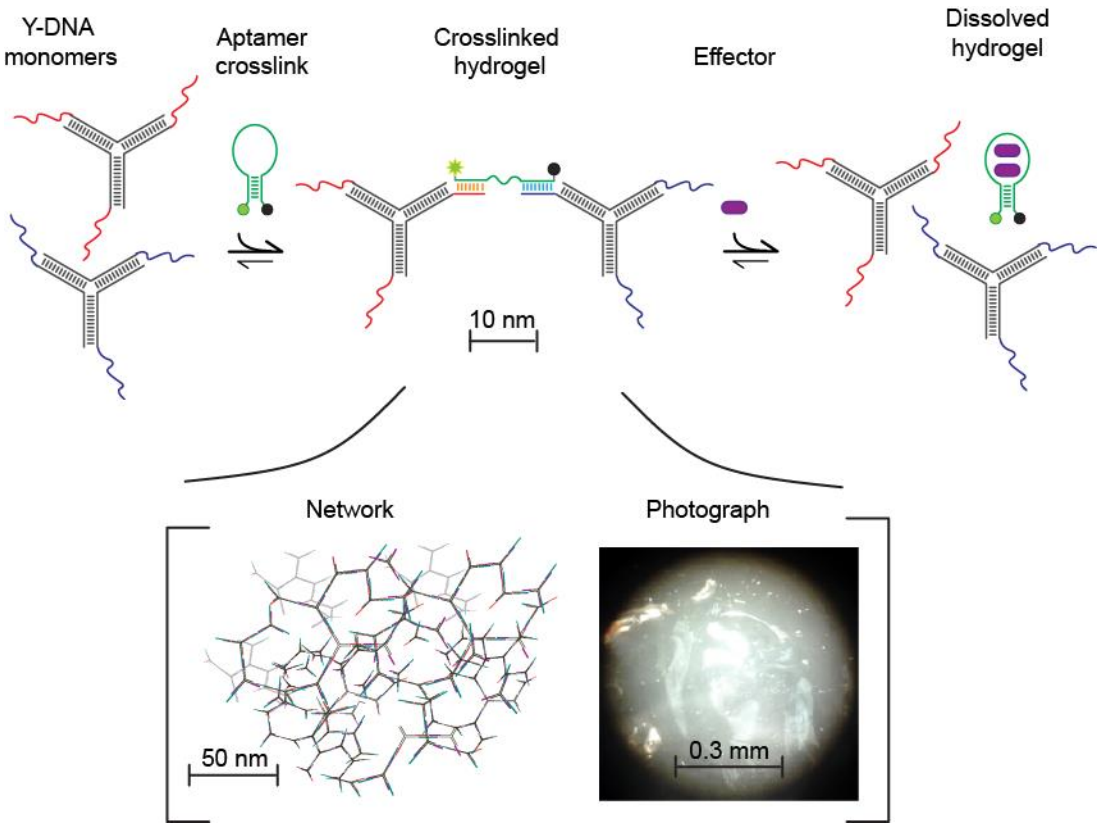

Figure 5-1. As our experimental system we employed an adenosine-responsive Y-DNA hydrogel. (***Top***) This hydrogel consists of Y-shaped "monomers" (each consisting of three annealed strands of DNA) with pendant, single-stranded arms. These arms are partially complementary to an adenosine-binding aptamer, which crosslinks the monomers to form a 3-dimensional network (***inset, left***) that forms a visibly thick gel (***inset, right***). In response to binding its specific molecular effector, adenosine, the aptamer dissociates and folds, disrupting the hydrogel.

binding-competent conformations. Similar control of the binding thermodynamics of aptamers has been achieved in many isolated aptamers free in solution (5-14, 5-15).

Despite these successful examples in which the responsiveness of solution-phase aptamers has been tuned, the exploration of responsive DNA hydrogels has remained rather qualitative. That is, only a few studies of DNA hydrogels have centered on the systematic,

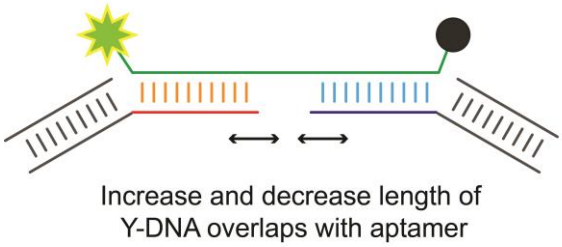

Free energy of binding the aptamer

5' overlap \ 3' overlap	9	8	7	6
9	-42.5	-37.0	-32.4	-26.6
8	-34.5	-29.0	-24.5	-18.8
7	-26.6	-21.2	-16.7	-10.9
6	-21.2	-15.8	-11.3	-5.6

Figure 5-2. We achieve control of the gel dissolution kinetics by changing the number of base pairs, and thus the affinity, with which the Y-DNA monomers bind to the adenosine aptamer crosslinker. (***Left***) Specifically, we systematically tuned the length with which the monomers' arms bind to the 5' and 3' portion of the adenosine aptamer. (***Right***) We predict the free energy of interaction by adding the base-pairing contributions of the 5' and 3' overlap sides with the aptamer calculated from Mfold (5-18, 5-19), to the estimated free energy penalty from gel formation estimated from the difference in adenosine-binding affinity from our previous work (5-12), Chapter 4.

quantitative control of their properties (5-16), and none to date have explored the relationship between base-pairing length or geometry and response to molecular effectors. In response, here we use a simple, recently developed strategy to explore the effect of tuning the thermodynamic stability and network geometry of a model DNA hydrogel on the kinetics of its response to its molecular effector.

5.2 Results

We employ an adenosine-responsive of the modular, frequently employed Y-DNA hydrogel architecture as our model system. This architecture, first developed by Cheng *et al.* in 2009, consists of a network of Y-shaped DNA "monomers" (each consisting of three annealed strands that form a structural, double-stranded core with three pendant, single-

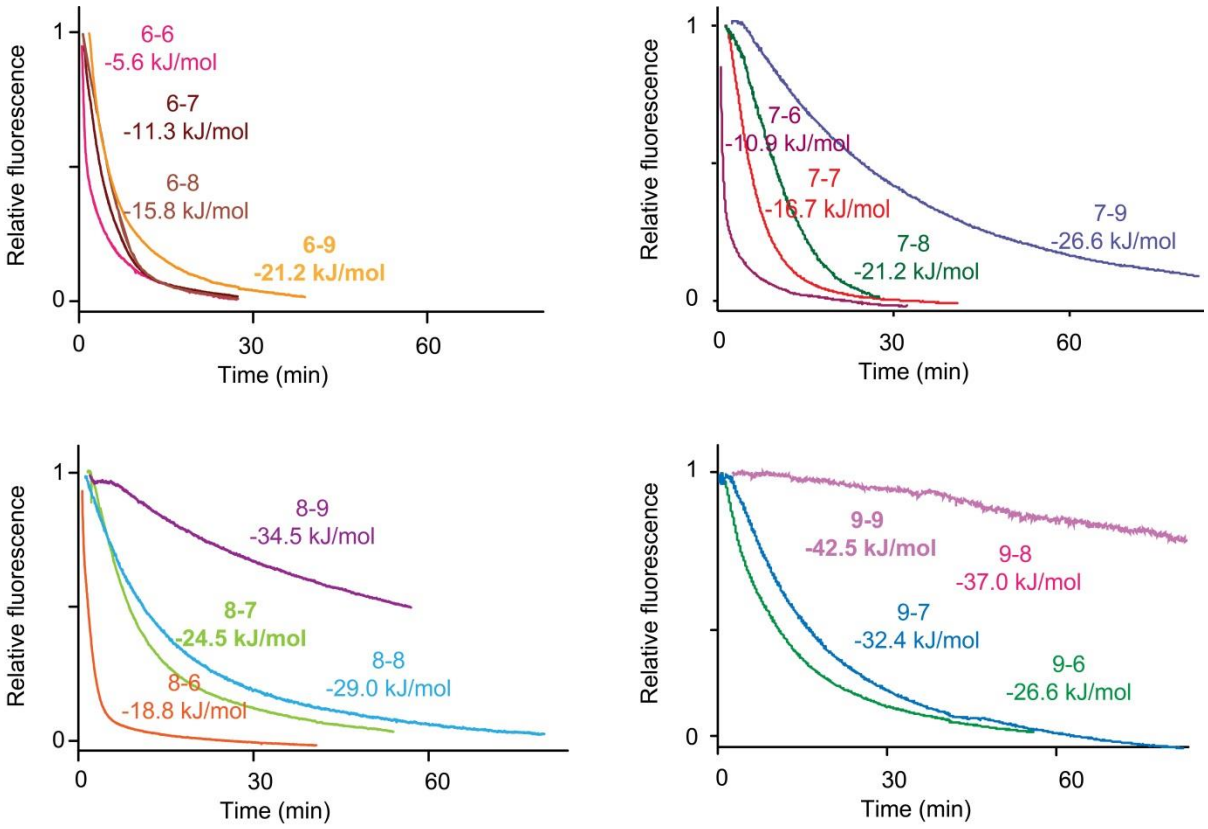

Figure 5-3. The addition or subtraction of a single base pair produces a substantial difference in dissolution kinetics. Here we show the normalized fluorescence decay curves in response to 10 mM adenosine for hydrogels in which the 5' end of the aptamer overlaps with 6, 7, 8, and 9 bases in which the 3' end of the aptamer overlaps with six bases (***top left***), seven bases (***top right***), eight bases (***bottom left***), and nine bases (***bottom right***). In the labels, "X-Y', X and Y refer to the number of bases that bind the 5' and 3' end of the aptamer crosslinker, respectively.

stranded arms) crosslinked via hybridization with a complementary sequence to form a dense 3-dimensional network (*Figure 5-1*) (5-7). In our model system, we employ the classic adenosine-binding aptamer of Huizenga and Szostak (5-18) as the crosslink, rendering the resulting hydrogel responsive adenosine. Mixing the aptamer with the Y-monomers produces a thick, relatively rigid hydrogel (*Figure 5-1, right inset*). To probe the relationship between affinity between the aptamer crosslinker and the monomers, we varied the length of the pendant single-stranded arms of each monomer to base pair with 6, 7, 8, and 9 bases on the

end of the adenosine aptamer. We investigated the kinetics of all 16 possible combinations (*Figure 5-2, right*).

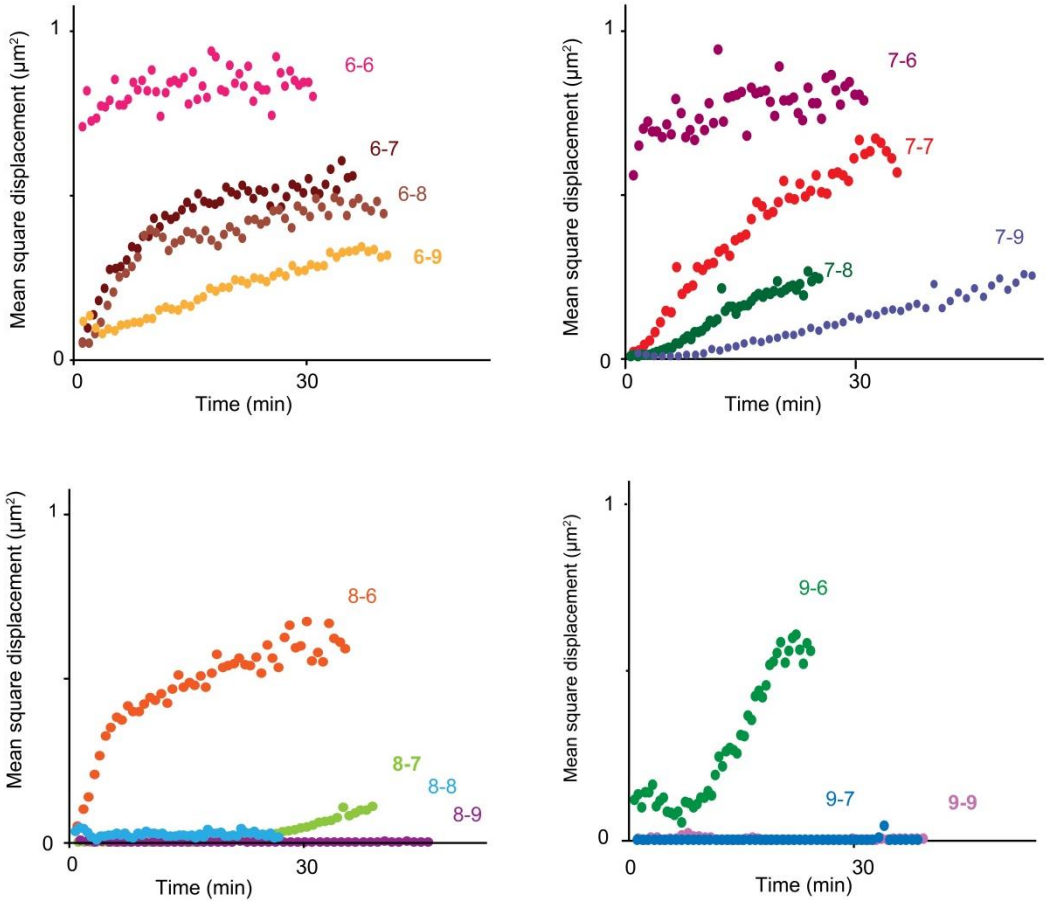

Figure 5-4. Like the molecular-scale kinetics, the micron-scale gel dissolution kinetics (measured with 1.0 μm diameter beads) become slower with increasing base pairing length between the Y-monomers and the aptamer. Notably, the least-stable gels, 6-6 and 6-7, do not appear strong enough to substantially entrap beads even very early in dissolution. On the other end of the spectrum, in the most stable gels (i.e., 8-8, 8-9, 9-7, and 9-9), substantial bead movement does not occur even after long times after addition of adenosine. In the labels, "X-Y', X and Y refer to the number of bases that bind the 5' and 3' end of the aptamer crosslinker, respectively.

Increasing the length of base pairing between the monomers and the aptamer increases the time required for dissolution at both the molecular (*Figure 5-3*) and micron

(*Figure 5-4*) length scales, with the addition or subtraction of even a single base pair being sufficient to alter significantly the dissolution rate. Quantitatively, the half time for dissolution t_{half}, which we define here as the time required for aptamer fluorescence to fall to 50% of its initial value, increases near monotonically with increasing base-pairing length between the aptamer and the monomers (*Figure 5-5, top left*). Varying only the extent to which the Y-monomers bind to the aptamer, we observed a wide range of dissolution kinetics in response to 10 mM adenosine. t_{half} increases from 3.7±1.1 min using Y-monomers that bind six bases at the ends of the adenosine aptamer to longer than two hours using Y-monomers that bind at least eight at the 5' end of the aptamer and nine bases at the 3' end of the aptamer.

Comparing the hydrogel dissolution kinetics to the thermodynamic stability of the gel (i.e., the thermodynamics of interaction between the Y-monomers and crosslinker) results in quantitative validation and supports the approach as generally applicable. We estimated the free energy of interaction by adding the favorable free energy of the aptamer base-pairing with the monomers to the unfavorable free energies associated with breaking the base-paired stem in the free aptamer, which we also calculated with Mfold, and with restricting the position of the aptamer and Monomers to form the hydrogel (5-19, 5-20) (*Figure 5-2, left*). In our estimation, the cost of restricting the positions of the aptamer comes from two main sources. The first is the entropic cost of restricting the position of the non-base paired portion of the aptamer when forming the hydrogel, which scales logarithmically with the length of this non-base-paired region (5-21). The other cost arises from the translational entropy loss associated with restricting the position of the monomers and aptamer in forming the gel, which we estimate from our previous work as approximately 33 kJ/mol (5-12; Chapter 4).

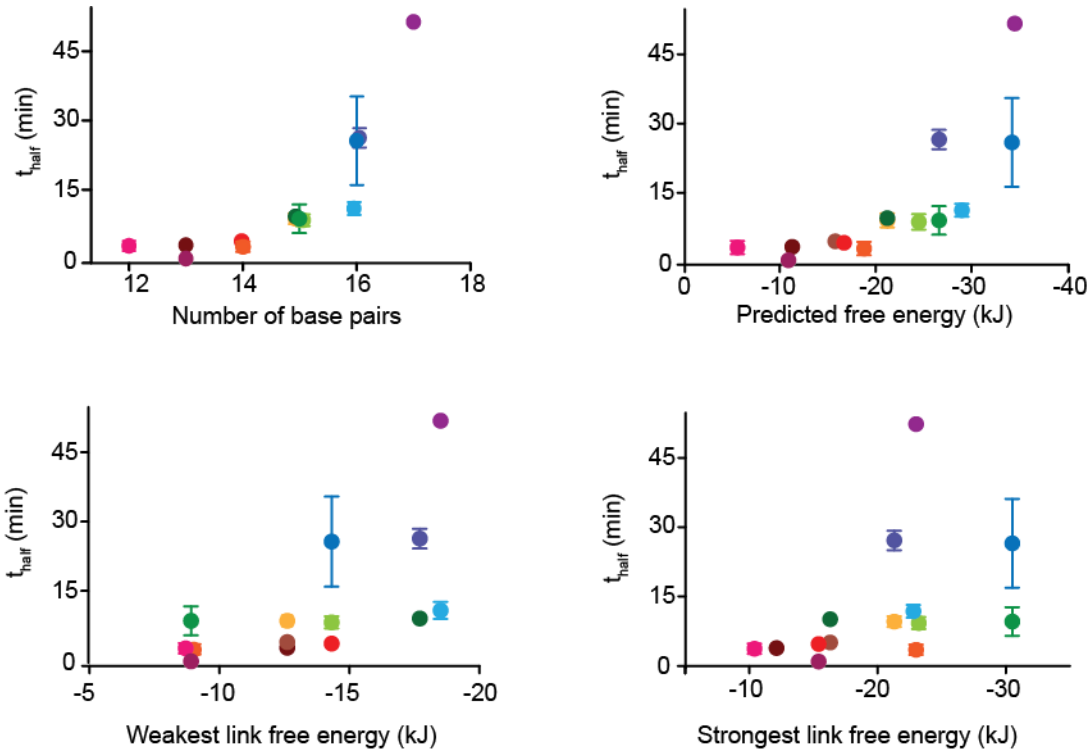

Figure 5-5. The dissolution kinetics of the hydrogel depend a combination of geometric and energetic factors. The dissolution kinetics are perhaps most closely related to the number of overlapping base pairs between the Monomers and the crosslinking aptamer (***top left***), with a near-monotonic relationship between the number of overlapping base pairs and the t_{half}, the time required for the normalized fluorescence to decrease by 50%. The dissolution kinetics are also closely related to the predicted binding free energy between the aptamer and the Y-DNA monomers (***top right***), although this relationship appears somewhat less monotonic, particularly at higher numbers of base pairs and predicted free energies. The dissolution kinetics are also related, though less monotonically, to the weaker (***bottom left***) and stronger (***bottom right***) of the two Y-monomers that the aptamer binds to, suggesting that neither the first or second side of the aptamer to dissociate from the Y-onomers plays a simple role in limiting the kinetic rate of dissolution.

Comparing the estimated free energies of interaction between the monomers and the aptamer to the dissolution kinetics, we find that in general, the half time of dissolution increases with increasing free energy of interaction between the monomers and the aptamer. However, neither the base-pairing length nor the free energy of interaction is entirely

predictive of dissolution kinetics, suggesting that the geometry of the monomers' interaction with the aptamer may play an important role. To investigate this relationship between base pairing geometry and hydrogel dissolution kinetics, we plotted the half times for dissolution versus both the free energy of hybridization for the "weakest link," the weaker side of each specific monomer combination (*Figure 5-5,bottom left*), and the free energy of hybridization for the "strongest link," the stronger side of each monomer combination (*Figure 5-5, bottom right*). We find that while dissolution half time generally increases with both increasing free energy of hybridization for both the weakest and the strongest link, neither is completely predictive of dissolution kinetics.

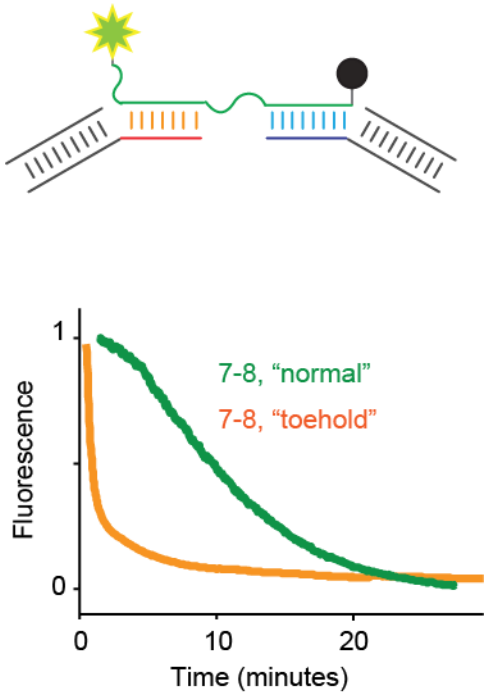

Figure 5-6. We achieve further control of our model DNA responsive hydrogels by employing monomers that bind the aptamer crosslinker internally, giving the aptamer a "toehold" to enable faster dissociation. (***Top***) In this construct, the Y-monomer that binds the 5' end of the adenosine aptamer binds the 4^{th}-10^{th} bases from the 3' end, leaving a toehold at the 5' end of the aptamer. (***Bottom***) Hydrogels containing monomers with this "toehold" binding dissolve much faster than those that bind at the end of the aptamer.

To further explore the relationship between monomer/aptamer geometry and the hydrogel dissolution kinetics, we measured the dissolution kinetics of hydrogels containing monomers that bound internally, rather than at the ends of the aptamer, thus giving the aptamer a "toehold" (*Figure 5-6, top*). As expected, these hydrogels dissolved substantially faster than the hydrogels containing monomers that base pair with the same number of bases of the aptamer crosslinker (*Figure 5-6, bottom*).

5.3 Conclusions

In summary, we demonstrate the use of both base-pairing length and geometry to control the response kinetics of target molecule responsive DNA hydrogels. Given the many successful examples of achieving quantitative control of the thermodynamics and kinetics of one-dimensional DNA switches (5-13, 5-14, 5-15), and in engineering responsive DNA hydrogels with a diverse variety of architectures and effector molecules (5-7, 5-8, 5-9, 5-10, 5-11, 5-12), we believe that the approach presented here may be of value in many artificial responsive materials and biotechnologies.

5.4 Materials and methods

Materials:

All reagent-grade chemicals, including adenosine, sodium phosphate monobasic, sodium phosphate dibasic, and sodium chloride were ordered from Sigma-Aldrich (St. Louis, MI). Glass slides were purchase from Fisher Scientific (Hampton, NH). Unlabeled DNA and

labeled DNA molecules were ordered from Sigma-Aldrich with desalt purification and Integrated DNA Technologies (Coralville, IA) with HPLC purification. Aqueous red Fluoro-Max beads of 1.0 μm diameter were ordered from Thermo Scientific (Waltham, MA). All reagents were used as purchased.

Each of the Y-DNA monomers employed in this hydrogel consists of three subunit strands that hybridize to form a Y-shaped structure with a double-stranded core and pendant single-stranded functional ends. The core sequences are those first reported by Cheng *et al.* (5-7), and the single-stranded ends are complementary to 6, 7, 8, and 9 bases on the 5' and 3' side of the adenosine-binding aptamer of Huizenga and Szostak (5-18). The sequences that compose the monomers are as follows, with the double stranded core section denoted in italics and the elements complementary to the aptamer sequences underlined:

5' monomer subunit strands:

5-6a: 5' *CTTACGGCGAATGACCGAATCAGCCT* <u>ACCTTCC</u>

5-6b: 5' *AGGCTGATTCGGTTCATGCGGATCCA* <u>ACCTTCC</u>

5-6c: 5' *TGGATCCGCATGACATTCGCCGTAAG* <u>ACCTTCC</u>

5-7a: 5' *CTTACGGCGAATGACCGAATCAGCCT* <u>ACCTTCCT</u>

5-7b: 5' *AGGCTGATTCGGTTCATGCGGATCCA* <u>ACCTTCCT</u>

5-7c: 5' *TGGATCCGCATGACATTCGCCGTAAG* <u>ACCTTCCT</u>

5-8a: 5’ *CTTACGGCGAATGACCGAATCAGCCT* ACCTTCCTC

5-8b: 5’ *AGGCTGATTCGGTTCATGCGGATCCA* ACCTTCCTC

5-8c: 5’ *TGGATCCGCATGACATTCGCCGTAAG* ACCTTCCTC

5-9a: 5’ *CTTACGGCGAATGACCGAATCAGCCT* ACCTTCCTCC

5-9b: 5’ *AGGCTGATTCGGTTCATGCGGATCCA* ACCTTCCTCC

5-9c: 5’ *TGGATCCGCATGACATTCGCCGTAAG* ACCTTCCTCC

3’ monomer subunit strands:

3-6a: 5’ CAGGT*CTTACGGCGAATGACCGAATCAGCCT*

3-6b: 5’ CAGGT*AGGCTGATTCGGTTCATGCGGATCCA*

3-6c: 5’ CAGGT*TGGATCCGCATGACATTCGCCGTAAG*

3-7a: 5’ CCAGGT*CTTACGGCGAATGACCGAATCAGCCT*

3-7b: 5’ CCAGGT*AGGCTGATTCGGTTCATGCGGATCCA*

3-7c: 5’ CCAGGT*TGGATCCGCATGACATTCGCCGTAAG*

3-8a: 5’ CCCAGGT*CTTACGGCGAATGACCGAATCAGCCT*

3-8b: 5’ CCCAGGT*AGGCTGATTCGGTTCATGCGGATCCA*

3-8c: 5’ CCCAGGT*TGGATCCGCATGACATTCGCCGTAAG*

3-9a: 5’ CCCCAGGT*CTTACGGCGAATGACCGAATCAGCCT*

3-9b: 5’ CCCCAGGT*AGGCTGATTCGGTTCATGCGGATCCA*

3-9c: 5’ CCCCAGGT*TGGATCCGCATGACATTCGCCGTAAG*

In contrast to the “normal” monomers, which base-pair with the aptamer sequence at its ends, the “toehold” monomers base-pair with the aptamer internally. The sequences are as follows:

5-7-toehold-a: 5’ *CTTACGGCGAATGACCGAATCAGCCT* TTCCTCCG

5-7-toehold-b: 5’ *AGGCTGATTCGGTTCATGCGGATCCA* TTCCTCCG

5-7-toehold-c: 5’ *TGGATCCGCATGACATTCGCCGTAAG* TTCCTCCG

3-8-toehold-a: 5’ TCCCCCA*CTTACGGCGAATGACCGAATCAGCCT*

3-8-toehold-b: 5’ TCCCCCA*AGGCTGATTCGGTTCATGCGGATCCA*

3-8-toehold-c: 5’ TCCCCCA*TGGATCCGCATGACATTCGCCGTAAG*

The aptamer strands are as follows, with the elements complementary to the (5’7 and 3’8) Y-monomers underlined:

Unlabeled: 5’ ACCTGGGGGAGTATTGCGGAGGAAGGT

Labeled: 5’ Alexa488-ACCTGGGGGAGTATTGCGGAGGAAGGT-Black Hole Quencher-1

Methods:

We synthesized each monomer by mixing a final concentration of 1.0 mM of each three component strands in 75 mM sodium chloride, 25 mM sodium phosphate, pH 7.0, then annealing by heating to 95°C for 5 min followed by cooling at a rate of 1°C/min to 4°C. We consistently achieved high yield of the desired products, which we confirmed using a 4-20% gradient acrylamide Tris/Borate/EDTA gel (100 V for approximately 45 minutes) stained with SYBR gold (*Figure SI 1*). To form the hydrogels, we mixed final concentrations of 0.18 mM of each Y-monomer with 0.48 mM unlabeled aptamer, approximately 480 μM labeled aptamer, and 0.002% by volume red fluoromax beads in 60 mM sodium chloride, 20 mM sodium phosphate at pH 7.

We synthesized and imaged the hydrogels in a specially designed imaging flow cell. The cell consisted of a 1.8 mm diameter, 0.75 mm deep cylindrical well drilled into a 75 x 25 x 1.0 mm glass slide overlaid by a polydimethylsiloxane (PDMS) channel consisting of a square hole placed over the cylindrical well flanked by two 0.8 mm by 20 mm channels (*Figure SI 2*). After synthesizing the gel in the well, we placed a glass coverslip over the PDMS layer, covering the well but not the ends of the channel. After waiting at least 15 minutes to ensure complete gelation, we added 20 μl of adenosine solution to the top of the gel by pipetting it from one side of the channel. We imaged in an enclosed hutch maintained at 20°C with high humidity to minimize evaporation. For imaging we employed an upright Olympus Fluoroview FV1000 MPE laser scanning confocal microscope with a 25x magnification, 1.05 numerical aperture Olympus X Plan N lens. We simultaneously excited

the aptamer fluorophore and fluorescent beads with 473 and 559 nm lasers, respectively, and detected via PMT detectors. Each frame was collected via raster scanning with a 512 x 512 pixel resolution and a 1.644 s^{-1} frame rate.

To obtain quantitative aptamer fluorescence decay curves we measured the average intensity of each image in the 473 nm fluorescence channel using ImageJ's batch measure function. We normalized each decay curve to the maximal and background fluorescence, which we obtained, respectively, by manually inputting the time of maximal fluorescence (generally at or shortly the addition of adenosine) and by fitting the last ~50% of the decay curve to an exponential equation using the Matlab cftool (see Matlab code section for code). To obtain fits of the exponential phase of the decay curves, we fit the portion where normalized fluorescence had decreased 25% from the maximal value to a simple exponential equation in Graph Pad plotting software. For each experimental condition (adenosine, bead size, and depth) we obtained at least triplicate measurements. We averaged the fluorescence of the replicates to obtain fluorescence versus time curves and the fit parameters of for each replicate to obtain average exponential time constants for each set of measurements.

We obtained bead tracks using the particle tracker function on Bitplane Imaris software. We analyzed this data to obtain the mean square displacements for all beads present over each frame. More specifically, we calculated the mean square change in distance over a frame between all sets of two beads present in both frames (excluding those separated by a distance less than 10x the bead diameter, see reference (5-4, 5-25)), which is approximately equal to twice the mean squared displacement (see Chapter 4.8.), then multiplied the values we obtained by 0.5. For visual clarity, we binned each mean square displacement versus time curve over 100 bins for Figures 5-3. We fit the time versus mean

square displacement curves to simple exponential equations in GraphPad, reporting the averaged mean squared displacement for a given bin for several replicates for each condition. We computationally analyzed the fluorescence and bead data with the scripts shown in Chapter 4.6.

5.5 References

5-1. Pollard TD (2014). The value of mechanistic biophysical information for systems-level understanding of complex biological processes such as cytokinesis. *Biophys Journal* **107**:2499-2507

5-2. Zlotnick A, Mukhopadhyay S (2011). Virus assembly, allostery, and antivirals. *Trends in Microbiology* **19**:14-23

5-3. Jahn R, Fasshauer D (2012). Molecular machines governing exocytosis of synaptic vesicles. *Nature* **490**:201-207

5-4. Meyers MA, McKittrick H, Chen P-Y (2013). Structural biological materials: critical mechanics-materials connections. *Science* **339**:773-779

5-5. Whitesides GM, Grzybowski B (2002). Self-assembly at all scales. *Science* **29**:2418-2421

5-6. Biffi S, Cerbino R, Nava G, Bomboi F, Sciortino F, Bellini T (2015). Equilibrium gels of low-valence DNA-nanostars: a colloidal model for strong glass formers. *Soft Matter* **11**:3132-3138

5-7. Cheng E, Xing Y, Chen P, Yang Y, Sun Y, Zhou D, Xu L, Fan Q, Liu D (2009). A pH-triggered, fast-responding DNA hydrogel. *Angew Chem* **121**:7776-7799

5-8. Helwa Y, Dave N, Froidevaux R, Samadi A, Liu J (2012). Aptamer-functionalized hydrogel microparticles for fast visual detection of mercury(II) and adenosine. *ACS Appl Mater Interfaces* **4**:2228-2233

5-9. Wei X, Tian T, Jia S, Zhu Z, Ma Y, Sun J, Lin Z, Y CJ (2015). Target-responsive DNA-hydrogel mediated “stop-flow” microfluidic paper-based analytic device for rapid, portable, and visual detection of multiple targets. *Anal Chem* **87**:4275-4282.

5-10. Zhang L, Lei J, Liu L, Li C, Ju H (2013). Self-assembled DNA hydrogel as switchable material for aptamer-based fluorescent detection of protein. *Anal Chem* **85**:11077-11082

5-11. Guo W, Qi X-J, Orbach R, Lu C-H, Freage L, Mironi-Harpaz I, Seliktar D, Yang H-H, Willner I (2014). Reversible Ag^{+}-crosslinked DNA hydrogels. *Chem Commun* **50**:4065-4068

5-12. Simon AJ, Walls-Smith LT, Freddi M, Fong FY, Gubala V, Plaxco KW (2015). Quantitative measurement of the molecular and micron scale dissolution kinetics of responsive DNA hydrogels. *In preparation.*

5-13. Vallée-Bélisle A, Ricci F, Plaxco KW (2009). Thermodynamic basis for the optimization of binding-induced biomolecular switches and structure-switching biosensors. *Proc Natl Acad Sci USA* **106**:13802-13807

5-14. Porchetta A, Vallée-Bélisle A, Plaxco KW, Ricci F (2012). Using distal-site mutations and allosteric inhibition to tune, extend, and narrow the useful dynamic range of aptamer-based sensors. *J Am Chem Soc* **124**:20601-20604

5-15. Armstrong RE, Strouse GF (2014). Rationally manipulating aptamer binding affinities in a stem-loop molecular beacon. *Bioconjugate Chem* **25**:1769-1776

5-15. Xing Y, Cheng E, Yang Y, Chen P, Zhang T, Sun Y, Yang Z, Liu D (2010). Self-assembled DNA hydrogels with designable thermal and enzymatic responsiveness. *Adv Mater* **23**:1117-1121

5-16. Nishikawa M, Ogawa K, Umeki Y, Mohri K, Kawasaki Y, Watanabe H, Takahashi N, Kusuki E, Takahashi R, Takahashi Y, Takakura Y (2014). Injectable, self-gelling, biodegradable, and immunomodulator DNA hydrogel for antigen delivery. *J Contr Rel* **180**:25-32

5-17. Huizenga DE, Szostak JW (1995). A DNA aptamer that binds adenosine and ATP. *Biochemistry* **34**:656-665

5-18. SantaLucia JR (1998) A unified view of polymer, dumbbell, and oligonucleotide DNA nearest-neighbor thermodynamics. *Proc Natl Acad Sci USA* **95**(4):1460-1465.

5-19. Zuker M (2003) Mfold web server for nucleic acid folding and hybridization prediction. *Nucl Acids Res* **31**:3406-3415.

5-20. Chan HS, Dill KA (1989) Intrachain loops in polymers. *J Chem Phys* **90**:492–509

5.6 Funding and Acknowledgements

We thank Mary Raven for training and technical support with imaging and Omar Saleh and Megan Valentine for helpful discussions regarding the interpretation of bead tracking data. This work was supported by the Beckman Scholars program funded by the Arnold and Mabel

Beckman Foundation, and from the Institute for Collaborative Biotechnologies through Grant W911NF-09-0001 from the U.S. Army Research Office. The content of the information does not necessarily reflect the position or the policy of the Government, and no official endorsement should be inferred. We also acknowledge the use of the NRI-MCDB Microscopy Facility and the Multiphoton/Laser Scanning Confocals supported by the NCRR and Office of The Director, National Institutes of Health of the NIH under Award # S10RR022585 and # S10OD010610 respectively.